OXYGEN DIFFUSION
IN MONOCLINIC ZIRCONIA SPHERES

OXYGEN DIFFUSION
IN
MONOCLINIC ZIRCONIA SPHERES

by

ANDREW MADEYSKI, Dipl. Eng.

A Thesis
Submitted to the Faculty of Graduate Studies
in Partial Fulfilment of the Requirements
for the Degree
Doctor of Philosophy

McMaster University
August 1967

DOCTOR OF PHILOSOPHY (1967)
(Metallurgy and Materials Science)

McMASTER UNIVERSITY
Hamilton, Ontario
Canada

TITLE: Oxygen Diffusion in Monoclinic Zirconia Spheres

AUTHOR: Andrew Madeyski, Dipl. Eng., (Polish University College, London, England)

SUPERVISOR: Professor W. W. Smeltzer

NUMBER OF PAGES: 164; (xiii)

SCOPE AND CONTENTS:

An investigation is reported of oxygen diffusion in monoclinic zirconia at elevated temperatures.

A method was developed for production of solid zirconia spheres of a quality suitable for diffusion measurements. The spheres, 60μ and 90μ diameter were subsequently used for the determination of the coefficient of self-diffusion of oxygen in stoichiometric zirconia at 800°C, 850°C, 900°C, 950°C and 1000°C. Oxygen 0^{18} isotope exchange using mass spectrometry for the gas analysis was employed for this investigation.

The oxygen self-diffusion coefficent was found to conform to the Arrhenius equation

$$D\ (\frac{cm^2}{sec}) = 8.58 \times 10^{-3} \exp\ (- 56224/RT)$$

Theoretical considerations indicate that this diffusivity represents virtually the lattice diffusion of oxygen in zirconia.

Diffusivities of oxygen in zirconia scale calculated from zirconium oxidation studies are 10^4 times higher and are believed to be due to short-circuit diffusion through line defects. To substantiate

this hypothesis, "slabs" of stoichiometric zirconia scale and irregular, but equiaxed particles of the same material were used for oxygen diffusion experiments employing the same method. The diffusivities for the slabs were 10^3 times higher than those for spheres, supporting the validity of the short-circuit diffusion theory for zirconia scale.

Oxygen concentration drop across zirconia scale on metal, during its formation by parabolic kinetics was calculated for 600°C and 850°C, and was found to be 0.04 g/cm^3 approximately, while the concentration drop across the interface between the oxide and the oxygen-saturated metal was about 1.07 g/cm^3.

ACKNOWLEDGEMENTS

The author wishes to express his gratitude to his supervisor, Dr. W. W. Smeltzer, whose scientific guidance, encouragement and understanding of the experimental problems throughout this investigation were most valuable and deeply appreciated.

Thanks are also due to Dr. J. S. Kirkaldy, as well as to Dr. C. C. McMullen and Dr. M. B. Ives (members of the Supervising Committee) for their valuable suggestions and constructive criticism; to Dr. H. G. Thode for the assignment of the mass spectrometer and of the isotopic water supply to this project; to Dr. W. H. Fleming and Dr. C. Calvo for their assistance and advice in connection with the mass spectrometry and X-ray diffraction respectively; to Dr. W. C. Hagel from the General Electric Research Laboratories, Schenectady, N.Y., for valuable information regarding the use of O^{18} for oxygen exchange in oxide spheres; to Dr. H. Schmalzried from the Institut für Theoretische Hüttenkunde, Clausthal-Zellerfeld, Germany, for a stimulating and informative discussion on the mechanism of oxygen diffusion in zirconia; to Mr. D. Zakaib, Mr. B. St. George, and Mr. D. Rasmussen from the British-American Oil Research Laboratories for their contribution in connection with the mass spectrometry; and to Mr. M. Van Oosten for the skillful and patient assistance with the preparation of zirconia spheres. The author wishes also to acknowledge gratefully two awards of the consolidated Mining and Smelting Co. Ltd. Research Fellowship.

This research project was supported by the United States Air Force Office of Scientific Research, Office of Aerospace Research and the National Research Council of Canada.

TABLE OF CONTENTS

LIST OF TABLES

LIST OF ILLUSTRATIONS

CHAPTER 1

INTRODUCTION

Zirconium, with its low neutron cross-section and high resistance to corrosion has become an important metal for canning fissile materials in atomic reactors and for special applications in industry and in aerospace projects. Unfortunately, the usefulness of this metal is considerably limited by its low resistance to high temperature oxidation. Despite the large amount of research done on this subject during the last decade, the oxidation mechanism is not completely understood. It is known that oxygen is the species which diffuses through the oxide to combine with zirconium at the oxide-metal interface. Consequently, the diffusion rate of oxygen in the oxide scale is an important factor in determining the oxidation properties of zirconium.

In view of this, the knowledge of the diffusion coefficient of oxygen in zirconia is of great practical and theoretical interest. Furthermore, the determination of this coefficient is vital to an understanding of the lattice defect structure and of the oxygen transport mechanism in zirconia. At present, oxygen diffusion results are not available to test the hypothesis that both interstitial oxygen and oxygen vacancies may exist in zirconia, their relative concentrations being dependent upon oxide stoichiometry.

A convenient method for determining the self-diffusion coefficient of oxygen in zirconia could be proposed where small oxide spheres heated to the desired temperature are exposed to an atmosphere of oxygen 0^{16} containing a non-radioactive isotope 0^{18}. This oxygen isotope would diffuse into the sample due to its much lower initial concentration in the solid. Thus, the progress of self-diffusion may be recorded by periodically taking samples of the atmosphere in the diffusion chamber for analyses of $0^{16}0^{18}$ to $0^{16}0^{16}$ gas ratios.

This method, however, is beset with difficulties because zirconia spheres must be prepared from an oxide which undergoes a destructive phase transition upon cooling after solidification. A method for preparation of zirconia spheres, a study on the structure of these spheres and application of a mass spectrometry technique for determining the oxygen diffusion coefficient in zirconia are described in this thesis. Moreover, these diffusion results are employed to elucidate more fully the oxidation mechanism of zirconium.

CHAPTER 2

DEVELOPMENT OF THE PRINCIPLE FOR PREPARATION OF ZIRCONIA SPHERES AND THEORY OF OXYGEN DIFFUSION IN ZIRCONIA

2.1 Zirconium-Oxygen Phase Diagram and Structure of Zirconium Oxide

The constitution of the system zirconium-oxygen, or more accurately, zirconium-zirconium dioxide was thoroughly investigated in 1954 by Domagala and McPherson(1). Iodide zirconium used in this study was combined with calculated amounts of ZrO_2 and arc melted. The resulting zirconium-oxygen alloys were carefully annealed at 21 temperature levels between 600 and 2000°C. Determination of the phase boundaries was accomplished by metallographic evaluation of specimens quenched from the various temperatures. Incipient melting techniques were employed to determine solidus curves, and x-ray diffraction work was used for establishing the lattice parameters of the α solid solution of oxygen in zirconium and of the zirconium dioxide crystals.

Further research work done in the United States, Russia and Europe, basically confirmed the original constitution diagram, but some modifications were introduced. Figure 1 shows the diagram brought up to date by Elliott(55) on the basis of the presently available data.

Zirconium metal transforms at 862°C from a low temperature close-packed hexagonal α phase structure to the high temperature body centered cubic β phase. This transformation temperature is raised by the addition of oxygen which at 25 a/o stabilizes the α phase up to its melting point of 1975°C. Furthermore, the solution of oxygen in zirconium

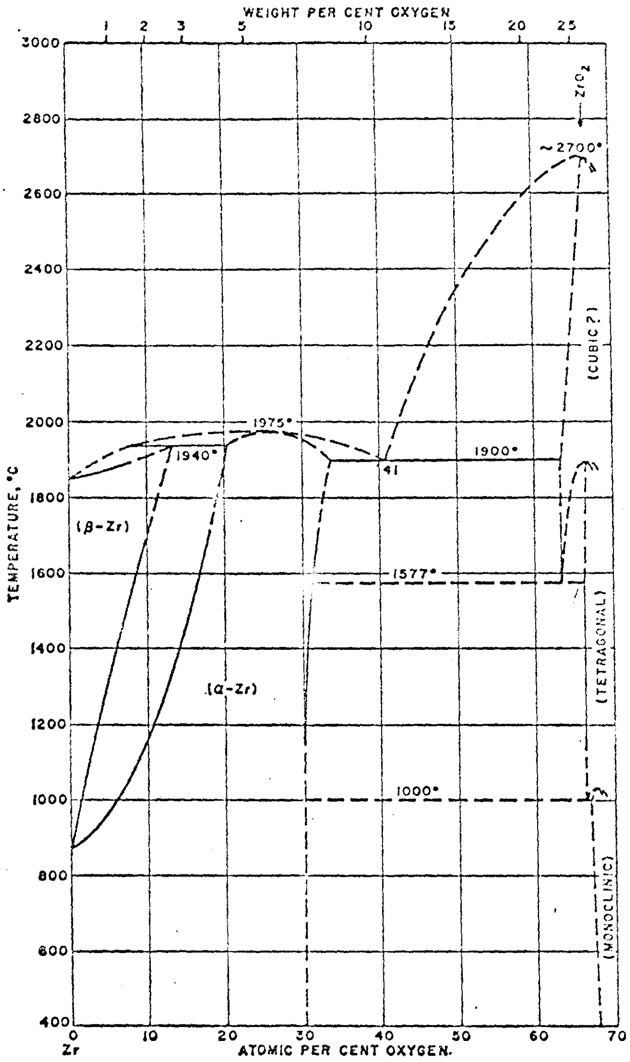

Figure 1

Zirconium - Oxygen constitution diagram (after Elliott(55)).

creates a two-phase region where both α and β zirconium are stable. The maximum solubility of oxygen in α-Zr was reported originally by Fast(3), de Boer(4) and Guldner(5) to be about 40 a/o. This was later reduced by Domagala and McPherson(1) to 29.2 a/o, but further investigation by Gebhardt indicated that the solubility at 1900°C reaches a maximum of 34 a/o approximately. However, these investigators agree that it is not possible to retain to room temperature solid solutions of α-Zr containing more than 30 a/o O.

On solidification of zirconium-oxygen alloys with less than 25 a/o O there is a peritectic reaction between α-solid solution containing 18.2 a/o O and the liquid with approximately 8 a/o O. Alloys whose oxygen content is between 25 a/o and 63 a/o form a eutectic of interspersed α-solid solution with 29.2 a/o O and zirconia with 63.0 a/o O. If the oxygen content of the liquid is between 65 a/o and 66.7 a/o, only substoichiometric zirconia is first formed on solidification. This zirconia, which is apparently cubic, undergoes a possible eutectoid reaction discovered by Gebhardt et al(39). They found by metallographic investigation that the solubility limit of ZrO_2 decreases sharply from 66.5 a/o to 63.4 a/o O when the temperature drops from 1835°C to 1570°C due to the presence of a eutectoid transformation.

Fully stoichiometric zirconia solidifies apparently in a cubic phase, and then transforms to tetragonal around 2285°C, as established by Smith and Cline(57). In the vicinity of 1000°C, it transforms again to a monoclinic structure, which is stable at room temperature. These transformations are described in more detail in a latter part of this Chapter.

The melting point of zirconia is very high and consequently not easy to determine accurately because of experimental difficulties. It has been variously reported as 2677 ± 20°C.,(19), 2687 ± 20°C.,(20), 2715 ± 20(21) and 2710 ± 15°C(22). The most common figure accepted in the literature is 2700°C, but more recent measurements of the melting point of hafnia-free zirconia by Curtis et al(49) produced the value 2850 ± 25°C.

It has been conclusively proved that zirconia corresponds to the general chemical formula ZrO_2 and that it has a cubic, tetragonal or monoclinic crystal structure depending on temperature. The existence and stability of other zirconium oxides or different crystal structures have been the subject of much speculation and controversy. The cubic structure of ZrO_2 was reported by Hoch and Johnston(30), who even observed an order-disorder transition from simple cubic to b.c.c. cubic at 1970°C. There is a possiblity that this may be the tetragonal-cubic transition suggested later by other investigators and shown tentatively in Figure 1. However, the composition of the alloy, quoted by Hoch and Johnston(30) as 50 a/o O, does not correspond to the 66.5 a/o O found by Gebhardt et al(39). The tetragonal structure has the lattice parameter ratio $c/a \simeq 1.01$, which is fairly close to 1, so that, making allowance for the experimental difficulties at high temperatures, this phase could conceivably have been mistaken for cubic by Hoch. Korobkov et al(45)(46) and Sarkisov et al(47) have detected the presence of cubic zirconia in the oxidation of zirconium metal. This zirconia phase is converted on heating below 1000°C to a tetragonal and finally the monoclinic form. Evans and Wildsmith(40) also reported a high temperature form of ZrO_2 which is cubic. It may be mentioned also that the cubic structure of zirconia can be produced and stabilized down to room temperature by addition of other oxides such as CaO, Y_2O_3, Dy_2O_3, La_2O_3, Sc_2O_3, Nd_2O_3, etc. However, since these are solid solution rather than pure zirconia, they are outside the scope of this work.

Suboxides of zirconium ZrO and Zr_2O_3 were reported by various investigators, e.g. Wedekind(23), Weiss and Neumann(24), van Arkel and deBoer(25), Jacob(26), Zintl et al(27) and Jakobs(28). However, these authors have given no conclusive evidence of the existence of these oxides, and some of the observations may be explained on the basis of the solid solutions. Samsonov(42) found some ZrO and ZrO_2 during the reduction of ZrO_2 with C. ZrO was found to be face-centered cubic, with the lattice parameter a = 4.62A. However, this form is undoubtedly not stable. Pearson(52) lists ZrO as "metastable" with a = 4.584A to 4.620A. Domagala and McPherson(1) in their investigation of the zirconium-oxygen system found no indication of any oxides other than ZrO_2.

The lattice parameters of the tetragonal zirconia were measured by Komissarova et al(48) and reported as a = 4.09A, c = 5.17A. The crystal lattice spacings of monoclinic zirconia were investigated by various research workers, both on this continent and in Russia. The lattice parameters are shown in Table 1 .

Monoclinic zirconia is of particular interest to us because this was the phase for which oxygen diffusivities were established in this work. The crystal structure of monoclinic zirconium dioxide is shown in Figure 2 based on work of McCullough and Trueblood(51). Zirconium ions are shown as small circles, while oxygen ions are indicated as large circles. This structure has the space group symmetry $P2_1/c$ with four

TABLE 1

Lattice constants of monoclinic zirconia

Investigators	Year	a	b	c	Angle β
Yardley(53)	1926	5.21 kX 5.16 kX 5.17 kX	5.26 kX 5.21 kX 5.22 kX	5.375 kX 5.32 kX 5.33 kX	99° 28'
Ruff and Ebert(54)	1929	5.174 kX	5.266 kX	5.308 kX	99° 12'
Curtis et al(49)	1954	5.21 A	5.26 A	5.375 A	99° 58'
McCullough and Trueblood (51)	1959	5.169 A	5.232 A	5.341 A	99° 15'
Adam and Rogers(50)	1959	5.1454 A	5.2075 A	5.3107 A	99° 14'
Komissarova et al (48)	1960	5.12 A	5.202 A	5.308 A	99° 18'

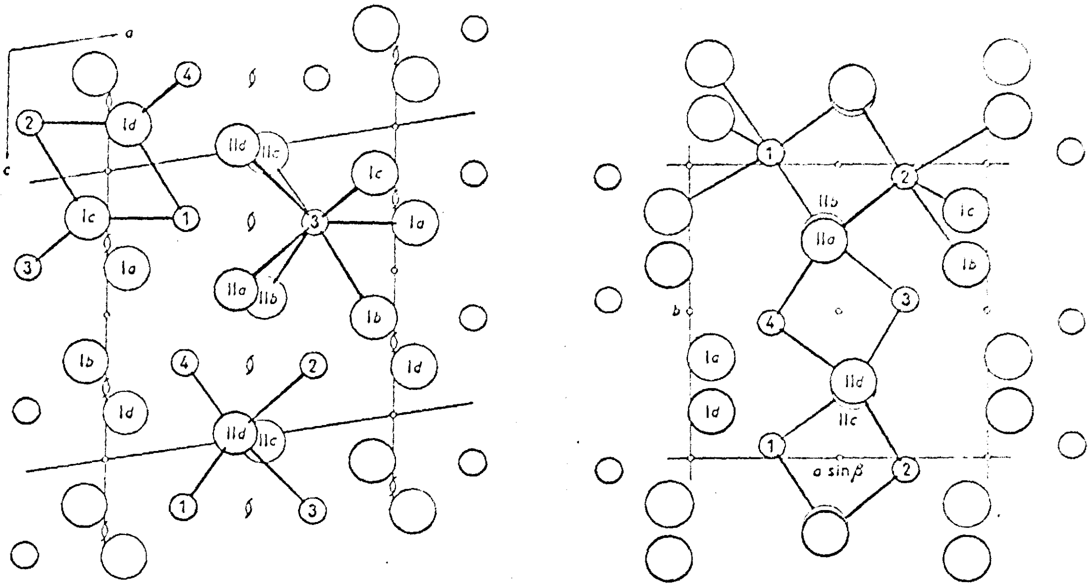

(a) Projection on (010)

(b) Projection on (001)

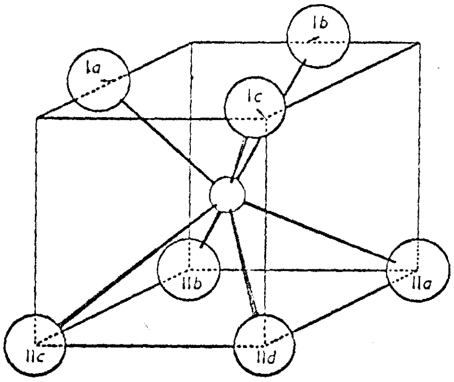

(c) The Zr coordination polyhedron (idealized)

Figure 2

Crystal structure of monoclinic zirconia (ZrO_2). Small circles: Zr. Large circles: O. (From McCullough and Trueblood(51)).

ZrO_2 in the unit cell.

There are two very interesting features of the structure . One is the seven-fold coordination of zirconium. The zirconium-oxygen distances in the coordination polyhedron vary from 2.04A to 2.26 A. That the coordination number is clearly seven is shown by the fact that the nearest zirconium-oxygen ion separation is 3.77A. The coordination polyhedra are shown in Figure 2 (a) and (b), and in a somewhat idealized form in Figure 2 (c). This last drawing indicates that the coordination polyhedron about Zr may be visualized as being derived from a cube. If the three upper oxygen ions are moved in the directions of the arrows, their distances from the zirconium ion at the center of the cube will be more nearly equalized, but still will average somewhat less than the Zr-O distances for the four oxygen ions at the corners of the cube base. This presentation of the Zr coordination polyhedron is somewhat idealized as may be shown by a precise calculation of the inter-ionic distances, but it does give a fairly close approximation to the structure of monoclinic zirconia.

Another interesting feature of the structure is the alternation of fluorite-like layers containing oxygen ions in tetrahedral coordination, marked O_{II} in Figure 2 , with layers which contain O_I ions in triangular coordination. These layers are parallel to (100) and are approximately a/2 in thickness. The Zr-O_{II} distances in the O_{II} coordination tetrahedron range from 2.16A to 2.26A, with an average of 2.22A. The central angles at O_{II} in this tetrahedron range from 100° to 132° with an average of 109°. In the O_I coordination triangle, the Zr-O spacings are 2.04A, 2.10A and 2.15A, producing an average of 2.10A, and central angles at O_I are equal to 106°, 109° and 145°.

This type of structure for monoclinic zirconia explains the strong tendency of these crystals to twin on the (100) plane. This twinning is so common that untwinned crystals of the naturally occurring zirconia, the mineral baddeleyite, are rare. McCullough and Trueblood$^{(51)}$ interpreted this tendency to twinning to be due to the relatively low energy difference between the ZrO_7 configuration found in the structure and another arrangement in which the group of three O_I is rotated 180° about an axis approximately perpendicular to the plane of the four O_{II} ions. However, Smith and Newkirk$^{(56)}$ pointed out the importance of the anti-parallelism of the O_I and O_{II} planes with respect to the twin plane. A simple reflection of the structure across a plane parallel to (100) or a rotation about a two-fold axis parallel to the c axis will not result in an acceptable twin boundary configuration. However, a very acceptable boundary may be obtained by rotating the structure about a twofold axis through $x = \frac{1}{2}$; $y = \frac{1}{2}$ and translating one half of the twin $\frac{1}{2}$ a with respect to the other half. This is shown in Figure 3 . In this arrangement, the composition plane is the plane of the O_{II} ions. In analogy to the model proposed by McCullough and Trueblood, this type of displacement may be described also as a rotation of the O_{II} group about an axis nearly perpendicular to the plane of the O_I group. The distortion of the ZrO_7 groups at the composition plane results from an adjustment of the O_{II} ions to positions which are midway between the positions satisfying the stable configurations of each half of the twin. This shift is only about 0.025A, which produces very little distortion.

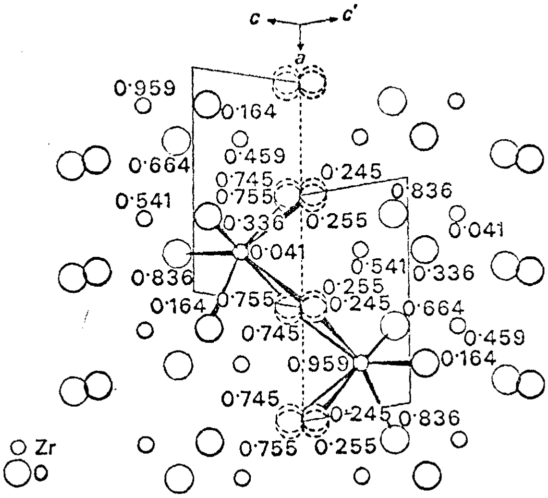

Figure 3

Twinning mechanism model for monoclinic zirconia proposed by Smith and Newkirk(55).

Projection of (100) composition plane of the (100) twin. The unit cell is partially outlined to indicate the $\frac{a}{2}$ glide conditon at the boundary. The dotted circles representing oxygen atoms show positions for both halves of the twin. The final oxygen position will be an average of the two possibilities. The numbers represent the y coordinate for each atom in terms of b.

2.2 Polymorphic Transformations in Zirconia

Phase transformations in zirconia have attracted a large amount of interest during the last decade because of their theoretical and practical importance.

The tetragonal-cubic inversion temperature has been established as 2285° ± 50°C by Smith and Cline(57). The temperature hysteresis of 30°C associated with this inversion suggests a "displacive" transformation, using the terminology introduced by Buerger(63). A displacive transformation, which is synonymous with Ubbelohde's(64) "continuous" type of transformation, is one in which there is only a slight displacement of atoms, of the order of thermal motion. The high temperature and the low temperature forms of a crystal under a displacive (or continuous) transformation possess related symmetries. Comparing Figures 4 and 5 it is easy to notice that this applies to the tetragonal-cubic inversion in zirconia. The oxygen ions of the tetragonal phase shift along the c axis to the planes $z = \frac{1}{4}$ and $\frac{3}{4}$ with a corresponding decrease in length of the c axis and an increase in length of the a axis until they become equal. No change in the bonding configuration is required.

Crystals which undergo displacive transformations have a strong tendency to retain their original orientation. A typical example is potassium hydrogen phosphate , $KH_2\ PO_4$,studied in detail by Ubbelohde and Woodward(65). If a tetragonal single crystal of this compound is cooled to about -100°C, domains of a new orthorombic phase appear, but these domains are oriented so as to preserve the direction of the c axis and either the a or the b axis. During the transformation, domains of

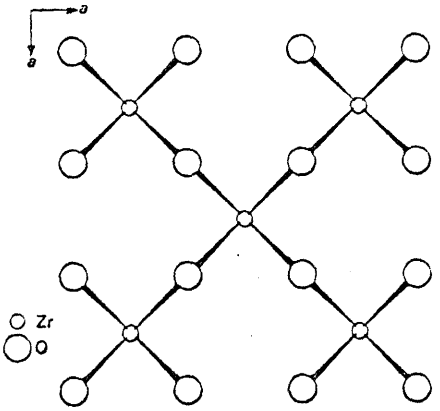

Figure 4

One layer of ZrO_8 groups in the cubic ZrO_2 structure. The plane of projection is (100).

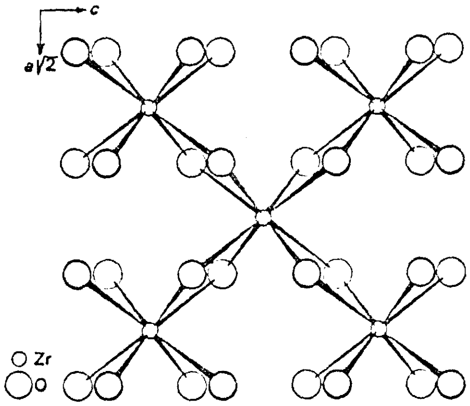

Figure 5

One layer of ZrO_8 groups in the tetragonal ZrO_2 structure. The plane of projection is (110). (From Smith and Newkirk$^{(55)}$).

both the high and the low temperature structures co-exist. When the temperature of the crystal is raised above the transformation interval, the original single crystal is restored. This cycle can be repeated indefinitely. Continuous transformations invariably occur over a temperature interval and show a hysteresis.

On the other hand, a crystal subjected to the other type of polymorphic transformation, called "reconstructive" by Buerger(63) and "discontinuous" by Ubbelohde(64), does not retain the original orientation. A representative example is that of the monoclinic - rhombic transformation of sulfur. If a single crystal of monoclinic sulfur is heated to the transformation temperature, many nuclei of the rhombic high temperature phase are formed. These nuclei then grow to produce the rhombic phase composed of a large number of randomly oriented grains. When the specimen is cooled back to room temperature, it is no longer a single crystal but consists of randomly oriented grains of the monoclinic form.

The monoclinic to tetragonal inversion of zirconia is crystallographically not as straightforward as the tetragonal to cubic, because of the larger symmetry differences between the former structures. This transformation was studied experimentally and theoretically by a number of investigators, including Murray and Allison(66), Bailey(67), Wolton(68)(69), Grain and Garvie(70), and Sukharevskii et al(71). Grain and Garvie(70) made an extensive investigation of this transformation using single crystal x-ray methods, high-temperature diffractometry and differential thermal analysis. Their first experiment consisted in taking room temperature Laue transmission photographs of a single crystal of zirconium dioxide before and after the transformation. The following results were obtained: (a) The basic Laue pattern has been preserved even though the crystal has gone through the transformations monoclinic → tetragonal → monoclinic. (b) The diffraction pattern after the transformations consisted of streaks, rather than spots, and some of these streaks were doubled.

Result (a) indicated that the structure of the cycled monoclinic zirconium dioxide was close to that of the original single crystal, and that the inversion must proceed by a mechanism different from nucleation and grain growth. This conclusion is in disagreement with some of the earlier opinions, e.g. those of Kauer et al.(72) and Murray and Allison(66), who contended that the transformation proceeds through a diffusion mechanism. Wolton(68), however, likened the monoclinic → tetragonal transformation in zirconia to the martensite transformation in metals. Both transformations have many characteristics in common, although the latter is accompanied by plastic deformation which does not occur to the same extent in ceramic materials. For this reason, Wolton classified the zirconia inversion as "brittle martensitic transformation", in analogy with that in manganese arsenide. This brittleness in zirconia during the transformation, which is of great practical importance, will be discussed later.

The result (b) from the Grain, Garvie's(79) first experiment may be explained in the following way. When a monoclinic single crystal of zirconia is heated above 1100°C, domains of the tetragonal phase form in the monoclinic matrix. The tetragonal domains are highly oriented so that when the process is reversed, something approaching a single crystal is obtained. The streaks observed in the Laue photographs apparently result both from strain and from the fact that the specimen is not exactly a single crystal, but is made of a number of grains with a strong preferred orientation. The doubling of the streaks was undoubtedly caused by transformation twinning. During the reverse transformation, from tetragonal to monoclinic, monoclinic domains can form in different orientations with respect to one another. As they come into contact, they will either be in parallel or in symmetrical orientation. Those which meet with symmetrical orientations form twins. The model of these twins was discussed above.

High temperature x-ray diffraction methods were used by Grain and Garvie(70) to determine the kinetics of the transformation and the temperature hysteresis on zirconia powder samples. Their results are shown in Figure 6. Results of other investigators(71) are superimposed on the diagram, and shown in Figure 7. It will be seen that there is a hysteresis loop of approximately 250°C between the forward and the reverse transformations. There is also a two-phase region of approximately 100°C for the forward, and 500°C for the reverse transformation. Another interesting feature of the transformation is the fact that the amount of materials converted to a new phase at any temperature remains constant after an initial rapid rise. To increase the amount of material transformed the temperature must be changed.

This type of behaviour is termed "athermal" kinetics, and may be explained in the following way. During the transition, coexistence of the monoclinic and the tetragonal structures occurs in a hybrid single crystal. Because of the volume difference between the two forms, there is strain at the boundary between the two structures. It is this strain energy which brings the reaction to a halt at any given temperature. One may consider that the monoclinic and the tetragonal structures are really end members of an infinite number of thermodynamic states, characterised by pressure,

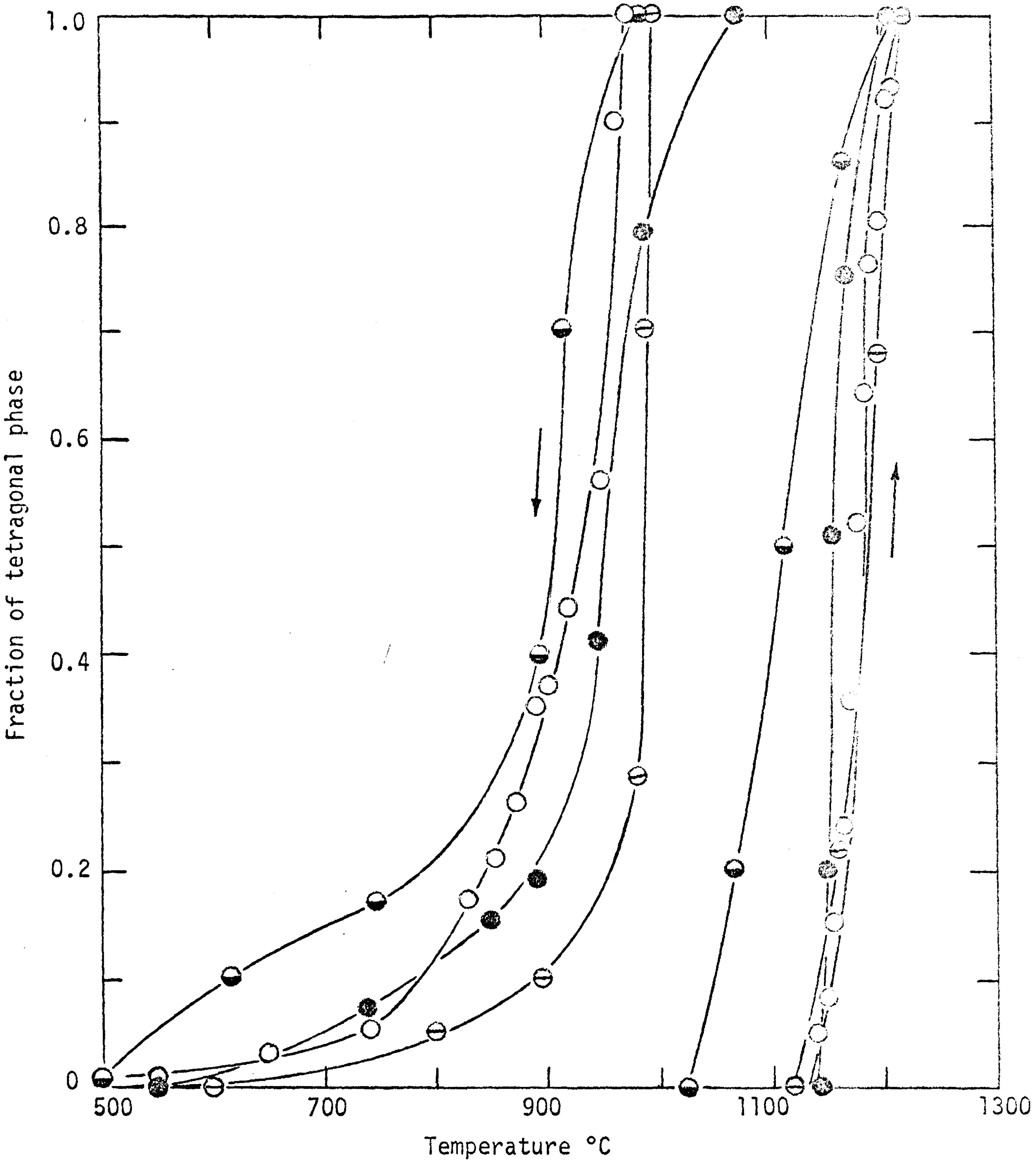

Figure 6

Fraction of tetragonal phase as a function of temperature during monoclinic ⇄ tetragonal transformation in zirconia.

O Specimen preheated at 1500°C (from Grain and Garvie[(70)])
θ Specimen not preheated
◒ Specimen preheated at 1000°C } (from Sukharevskii et al[(71)])
● Specimen preheated at 1750°C

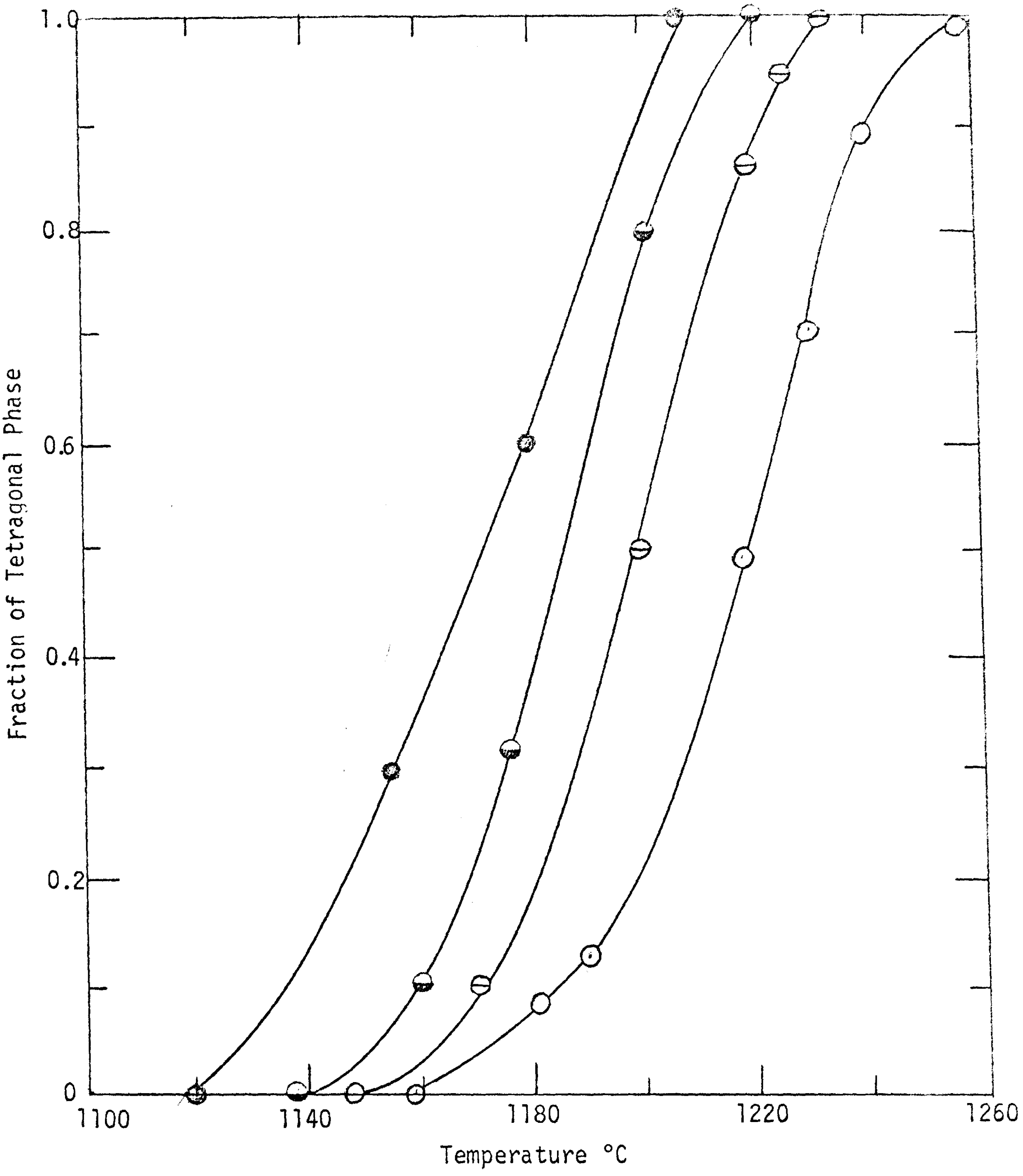

Figure 7

Fraction of tetragonal phase as a function of temperature for various numbers of cycles during the monoclinic-to-tetragonal transformation in zirconia

0 - 1 cycle	● - 3 cycles
θ - 2 cycles	● - 10 cycles

volume, temperature and strain. As the temperature is increased an incremental amount, the hybrid single crystal passes from one thermodynamic equilibrium state to another. This is apparently what Ubbelohde(64) had in mind when he called this phenomenon a "continuous transformation". This model explains also the existence of the temperature hysteresis between the forward and the reverse continuous transformations. The state of a hybrid crystal containing tetragonal domains in a matrix of the monoclinic structure is not the same as that of a crystal containing monoclinic domains in a matrix of the tetragonal structure, even though the phase ratio may be the same in both instances.

Grain and Garvie(70), Garvie(73) and Mazdiyasni et al(74) observed that very fine powders of zirconia obtained by precipitation from a solution or by thermal decomposition of zirconium alkoxide do not show the continuous type of transformation and if their crystal size is extremely small, the tetragonal phase may exist even at room temperature. This has been explained(70) by assuming that the average size of the new phase domain is about 1000A. When the particle size of a powder is less than a domain, coexistence of the two phases is impossible, and hence classical thermodynamics and kinetics apply to the inversion. When a single grain attains the transition temperature, it transforms discontinuously from the monoclinic to the tetragonal structure. The kinetics exhibit a logarithmic rate law. The stabilization of the high temperature tetragonal phase in very fine zirconia powders will be understood when it is realized that the surface energy of these tiny particles is relatively very high. For instance, in crystalites 270A in diameter, this energy amounts to 1000 cal/mole, which is equivalent to a temperature increase of 300°K(70).

Investigators who used for their experiments white zirconia which is essentially stoichiometric, did not take into account another important factor affecting the transformations, - the defect structure of this oxide. Zirconia can exist with a very extensive deficiency of oxygen, and the presence of a large number of anion vacancies has a profound effect on its properties. It has been proposed by Livingstone(76) on the basis of thermodynamic considerations, and proved experimentally by Livage and Mazières(77) that sub-stoichiometry tends to stabilize the tetragonal phase.

Since tetragonal zirconia occupies a smaller volume than the monoclinic phase, it may be expected that high pressure will tend to delay the tetragonal to monoclinic transformation. This effect existing on the microscopic scale has already been discussed in connection with the growth kinetics of the monoclinic domains. Similar results, however, should be observed by applying a high pressure to the complete crystal. This, in fact, has been observed by Vahldiek et al.(78) who produced a mixed tetragonal-monoclinic crystals by applying a pressure of 15-20 Kb to zirconia at 1200-1700°C and quenching the specimen to room temperature.

The crystallographic aspects of the tetragonal to monoclinic transformation were studied by Smith and Newkirk(56), who proposed the model shown in Figure 8. The crystal structure relationship of these phases is not as straightforward as that of the tetragonal and cubic. The most significant difference between the monoclinic and tetragonal structures is the change in the coordination of the Zr atoms and one of the O atoms which requires that some bonds be severed during the inversion. The most likely correlation is one in which the c axis of the tetragonal form

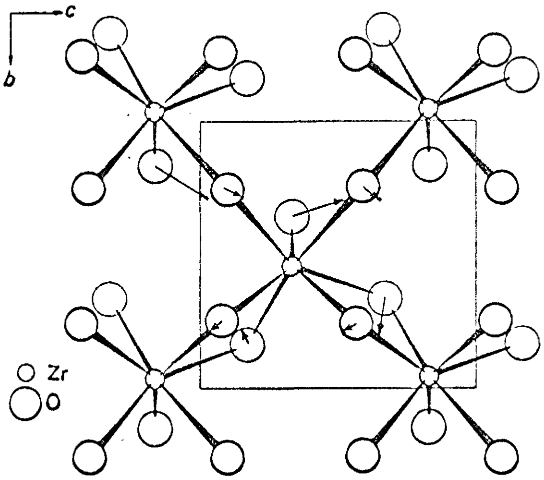

Figure 8

Monoclinic to tetragonal inversion model proposed by Smith and Newkirk(55). The layer of ZrO_7 groups in monoclinic zirconia at $x = \frac{1}{4}$ projected on the (100) plane. The unit cell outline represents its position at x = 0. The small arrows indicate the probable movement of oxygen ions to the tetragonal positions at the phase change.

corresponds to the c axis of the monoclinic phase. Small arrows in Figure 8 show the most likely shift which would take place during the transformation. The longest displacement is the movement of the O_I atom attached to the ZrO_7 group in the lower right of Figure 8 to join the center group. This atom which is initially 3.75A from the center Zr atom, moves about 1.2A. The whole transformation takes place by the rotation of the triangular groups of O_I atoms accompanied by minor movements of other atoms into the more symmetrical configuration.

The tetragonal to monoclinic inversion in zirconia is associated with a considerable volume change. Widely differing figures, however, have been quoted by various investigators who determined the percentage of this change either experiementally or by calculation. For instance, Debuigne and Lehr$^{(79)}$ estimated from the lattice parameters that this change should be of the order of 5%. Grain and Garvie$^{(70)}$ report the value of 6%, while Yavorsky$^{(80)}$ quotes a figures of 3.2% for the length contraction, which would correspond to 9.3% volume change. Douglass$^{(81)}$ made dilatometric measurements on specimens originally produced from zirconia powder under 3000 lb/in^2 pressure at 2300°C. The diagram in Figure 1 of his paper indicates that the length change of the specimen during the monoclinic to tetragonal transformation was more than 1.05%. Unfortunately, it appears from his curve that the transformation was not completed before commencement of the cooling cycle. Furthermore, the final sample length after the monoclinic - tetragonal - monoclinic cycle was greater than the original length, indicating that a certain amount of the tetragonal phase existed in the monoclinic specimen at the beginning of the cycle. This could be possibly explained by the fact that the specimen was originally produced under high pressure which tended to stabilize the tetragonal structure. In any case, the results of this dilatometric study indicate that the volume change during the monoclinic to tetragonal transformation must be at least 3.1%. In fact, in the Discussion section of the Debuigne and Lehr's paper(79), Douglass stated that this phase transformation is associated with a 10 - 12% volume contraction.

The discrepancies in the reported volume changes result apparently from different specimen textures, grain sizes, impurity levels, densities, orientations, etc.

Whatever the value of the contraction on heating or expansion on cooling actually is, it is usually sufficiently high to cause extensive cracking in zirconia undergoing the transformation. This is primarily caused by the fact that the transformation temperature range is about 1600°C below the melting point of zirconia, where the material possesses a much lower ductility. The cracking has far-reaching technological and experimental implications, as will be seen below.

2.3 Mechanical Properties of Zirconia and Their Relation to Oxygen Vacancy Concentration

The mechanical properties of zirconia as a function of temperature are of considerable importance both for the zirconium metal oxidation studies and for the preparation of diffusion specimens, such as were used in this study. Unfortunately, there is relatively little information on this subject in the literature. Saur et al(82) investigated the deformation of zirconium sheet specimens during oxidation at 900°C in air. They found considerable buckling of the rectangular specimens when the oxide thicknesses on both sides were not equal, which was particularly noticeable in the linear oxidation range after the "breakaway" point.

This was a visible manifestation of the high stresses produced in the metal and in the oxide layers as a result of a high Pilling-Bedworth ratio (molar volume ZrO_2/molar volume Zr), which is 1.56 approximately. Greenbank and Harper(83) investigated this phenomenon more thoroughly and attempted to determine the magnitude of the stresses in the oxide by using circular zirconium sheet specimens clamped around periphery, heated to 400° or 500°C and exposed to an oxidizing atmosphere at one side only. The stresses were calculated from the curvature of the specimen, assuming the Young's modulus for the monoclinic zirconia to be $E = 3.02 \times 10^7$ psi(84). The maximum stresses in the oxide determined in this way were of the order of 4×10^5 psi.

Another experiment conducted by the same investigators consisted in oxidizing at 370° - 560°C, both sides of long zirconium strips, 10 mils thick, 1/4 inch wide and 8 inches long. After oxidation, while still at temperature, the strips were wrapped around a metal former of continuously decreasing radius of curvature, so that the outer surface of the oxide was subjected to a tensile strain which increased continuously along the length of the specimen. The position, and hence the value of the applied strain at which cracking first occurred was determined by plotting the number of cracks per unit distance against the distance along the strip and extrapolating to zero crack density. The thickness of the oxide at the point of zero crack density was then determined by metallographic sectioning of the oxide. The results obtained indicated that the elongation to fracture depends strongly on the oxide thickness. For instance, at 560°C, the applied elongation to cause fracture decreased continuously with increasing oxide thickness and reached zero at a thickness of about 8μ. Extrapolation to zero thickness of oxide indicated an elongation to failure of about 1.3%. A possible interpretation is that as the thickness of oxide increases, so does the degree of its imperfections, producing high localized stresses under external loading which add to the residual stresses resulting from the volume changes in the oxidation process.

In view of the high Pilling-Bedworth ratio for zirconia, it is obvious that either the metal substrate or the oxide, or both of them must deform plastically. Since the experimental evidence is relatively scarce, there is a difference of opinions as to where the major portion of the plastic deformation takes place. In the Discussion of the paper by Debuigne and Lehr on dry corrosion of non alloyed zirconium(79) Lehr stated that the interfacial stresses seem to be relieved mainly by creep in the metal which is far more plastic than the oxide film, and that the plasticity of the oxide film is very low, even at high temperatures. Douglass, however, was of the opinion that at the oxidation temperatures, the strength of the oxide film may be equal to or less than that of the oxygen - contaminated zirconium, and the oxide may plastically deform to relieve the coherency stresses. This view finds some support in the observations performed by Wanklyn(85) who examined zirconia films by electron transmission microscopy. He found that the appearance of the oxide was that of a heavily cold worked material, indicating a large amount of previous plastic deformation.

Zirconia can exist with a large oxygen deficiency, in which case its color is black. The maximum degree of substoichiometry has not been determined with certainty. Cox, in an unpublished report, summarized the experimental results of sixteen independent investigators who attempted to determine the minimum amount of oxygen which may exist in single-phase zirconia. None of the results was entirely reliable, but the lowest composition quoted was $ZrO_{1.70}$. In any case, it may be expected that a large concentration of oxygen vacancies will facilitate the diffusional processes and increase the ductility of the oxide. This fact has been found by Douglass(81). He partially oxidized a piece of black zirconia to produce white, stoichiometric rings around the anion deficient grains. Micro-hardness measurements were then made within a single grain on both the anion-deficient and the stoichiometric portions. The size of the hardness impressions was identical, i.e. the hardness values were the same.. However, a notable difference existed in the characteristics of the indentations. The black zirconia consistently showed more sharply defined indentations and there was no evidence of any cracks in the vicinity of the identiations. The indentations in the stoichiometric layer exhibited numerous cracks radiating outward from the corners and in a semi-circular fashion from one corner to another. In the previously-mentioned Discussion of the paper by Debuigne and Lehr(79) Douglass also reported a considerable drop in the hardness of black zirconia with an increase in temperature. When the temperature of $ZrO_{1.995}$ was raised from 23°C to 700°C, its hardness decreased from 600 to 300 DPH.

2.4 New Principle for Producing Solid Zirconia Spheres

Measurements of oxygen diffusion in various ceramic materials by isotope exchange using O^{18} was done by a number of investigators. Haul and Just(89)(90), who were among the earliest employing this method, used for their experiment cadmium oxide crystals which were approximately equiaxed, but not exactly spherical. However, in the mathematical treatment of the results, they assumed the spherical shape for the particles. Similar experiments were later carried out by Haul and Duembgen(91) on titanium oxide, quartz and quartz glass.

Hagel and Mackenzie(92) used the O^{18} exchange method for investigation of the oxygen diffusion in aluminborate and aluminosilicate glasses. The specimens were prepared in form of long fibres with diameters of 17, 18 and 30μ, and the equations used for the analysis were those derived for infinitely long cylinders. Consistent and reproducible results were obtained by this method.

In the case of crystalline materials, the use of actual spheres instead of irregularly shaped particles offers many advantages. First of all, the mathematical treatment of the experimental results is more rigorous instead of approximate. Furthermore, the size is more uniform, because thin but long particles which would pass through a sieve of a given size are nonexistent. Finally, all the crystallographic directions are equally represented so that the value obtained for the diffusion coefficient is closer to the average.

Spheres, obtained by dropping irregular particles through an electric arc, were used for diffusion experiments by Kingery and Berg(94). Following the same method, Oishi and Kingery(96) investigated self-diffusion of oxygen in single crystal and polycrystalline aluminum oxide. Later, Kingery et al(97) used $NiCr_2O_4$ and α-Fe_2O_3 spheres for the determination of the oxygen mobility in these oxides. Hagel(93) conducted an extensive investigation of anion diffusion in α-Cr_2O_3 using 90μ and 127μ diameter chromium oxide spheres, and oxygen O^{18} as a tracer. He found that the isotope equilibrium on crystal surfaces was quickly established, and the rate-determining factor was self-diffusion within the spheres.

In view of these successful experiments, it appeared very promising to use this method for the investigation of oxygen diffusion in zirconium dioxide. In fact, Kingery et al$^{(95)}$ followed this procedure for the determination of the oxygen ion mobility in a cubic zirconia-calcia alloy ("stabilized zirconia") which does not exhibit polymorphic transformations at high temperatures. Unfortunately, pure monoclinic zirconia, undergoes the transformation discussed in Section 2.2 of this thesis, and this is associated with the large volume changes described in Section 2.3. Consequently, the spherical specimens tended to crack or even disintegrate while cooling from the arc temperature. However, in view of the lower brittleness of the substoichiometric zirconia, discussed in Section 2.3, it appeared reasonable to expect that black zirconia spheres may withstand the transformation without failure. This would require a reducing atmosphere in the arc furnace, which would partially deoxidize ZrO_2. Black spheres could be then re-oxidized to full stoichiometry at a temperature below the transformation range.

This new principle proved to be entirely successful and we have described the method in a recent publication$^{(98)}$ submitted from this laboratory. The details of the method will be described in Chapter 3.

2.5 Crystal Defect Structure of Zirconia and its Dependence on Oxygen Partial Pressure

The defect structure of oxygen-deficient zirconia and its relation to the partial pressure of oxygen in the environment was investigated theoretically by Douglass and Wagner(99). These authors made the following assumptions in their analysis of the problem:

1) The finite thickness of space charge regions may be neglected since the concentration of charged defects in black zirconia under consideration is quite high, so that the effective thickness of a space charge layer is only about three times the diameter of the oxygen ion.

2) The ideal law of mass action applies, i.e. interactions among charged defects are negligible.

3) Since the lattice of zirconia is a distorted CaF_2 lattice, the existence of the same type of ionic defects may be assumed in both structures. Ure(100) found that these defects in CaF_2 consist of interstitial oxygen ions, oxygen ion vacancies, excess electrons and electron holes.

The concentrations of these defects must obey the electric neutrality condition which requires that the number of positive excess charges must be equal to the number of negative excess charges:

$$2x_v + x_p = 2x_o + x_n \tag{1}$$

where x_v, x_p, x_o and x_n are the concentrations of oxygen vacancies, electron holes, interstitial oxygen ions and excess electrons respectively. These concentrations are expressed as ratios of the number of defects to the number of Zr ions.

An "oxygen vacancy - interstitial oxygen ion" pair (anti-Frenkel defect) is created by an internal reaction:

oxygen ion on a regular lattice site = interstitial oxygen ion
+ anion vacancy.

The equilibrium constant for this reaction is

$$K_1 = x_o\, x_v \tag{2}$$

Similarly, for the internal reaction:

valence electron = excess electron + electron hole

the equilibrium constant equals

$$K_2 = x_n x_p \tag{3}$$

The surface reaction for the oxygen uptake from the gas phase may be written as

$\frac{1}{2} O_2$(gas) + 2 excess electrons = interstitial oxygen ion.

The equilibrium conditions for this reaction are:

$$\frac{x_o}{p^{1/2} x_n^2} = K_3 \tag{4}$$

The following limiting cases may now be considered.

1. For nearly ideal stoichiometric composition (white zirconia)

$$x_o \cong x_v \tag{5}$$

i.e. for every interstitial oxygen ion there is a corresponding vacancy in the lattice. In view of Eq. (2) there is then

$$x_o \cong x_v \cong K^{1/2} \tag{6}$$

2. For zirconia with a substantial excess of oxygen, the concentrations of oxygen vacancies and excess electrons are small compared to those of interstitial oxygen ions and electron holes, so that, in view of Equations (1), (3) and (4),

$$x_o \cong \frac{1}{2} x_p \cong \left(\frac{1}{4} K_2^2 K_3\right)^{1/3} p^{1/6} \tag{7}$$

and

$$x_v = \frac{K_1}{x_o} = \frac{K_1}{\left(\frac{1}{4} K_2^2 K_3\right)^{1/3}} p^{-1/6} \tag{8}$$

3. For zirconia with a considerable deficiency of oxygen (black zirconia), there is a large number of oxygen vacancies present, so that

$$x_v \cong \frac{1}{2} x_n \cong \left(\frac{K_1}{4 K_3}\right)^{1/3} p^{-\frac{1}{6}} \qquad (9)$$

and

$$x_o = \frac{K_1}{x_v} \cong (4 K_1^2 K_3)^{1/3} \quad p^{1/6} \qquad (10)$$

The partial electrical conductivity κ ion due to the motion of oxygen ions either as interstitials or via vacancies, may be expressed as

$$\kappa_{ion} = 2 F (u_o x_o + u_v x_v)/V_m \qquad (11)$$

where

u_o = electrochemical mobility of interstitial oxygen.

u_v = electrochemical mobility of anion vacancies.

F = Faraday constant

V_m = molar volume

Similarly, the partial electronic condubtivity κ_e is equal to

$$\kappa_e = F (u_n x_n + u_p x_p)/V_m \qquad (12)$$

where

u_n = mobility of excess electrons

u_p = mobility of electron holes.

The relations between the partial conductivities and the oxygen partial pressure may now be expressed for the three limiting cases.

1. For white zirconia of nearly ideal stoichiometric composition, Equations (5), (6) and (11) yield

$$\kappa_{ion} \cong 2 F (u_o + u_v) K_1^{1/2}/V_m \qquad (13)$$

The partial electronic conductivity depends on the relative magnitudes of the mobilities and concentrations of the electronic defects. If $u_p x_p >> u_n x_n$, there is

$$\kappa_e = \frac{Fu_p}{V_m} \frac{K_2 K_3^{1/2}}{K_1^{1/4}} p^{1/4} \tag{14}$$

Conversely, if $u_p x_p << u_n x_n$,

$$\kappa_e = \frac{Fu_n}{V_m} \frac{K_1^{1/4}}{K_3^{1/2}} p^{-\frac{1}{4}} \tag{15}$$

2. For zirconia with a substantial excess of oxygen there is

$$\kappa_{ion} \cong \frac{2F}{V_m} \Big[u_o(\tfrac{1}{4} K_2^2 K_3)^{1/3} p^{1/6} + u_v \frac{K_1}{(\frac{1}{4} K_2^2 K_3)^{1/3}} p^{-\frac{1}{6}}\Big] \tag{16}$$

and, if $u_p x_p >> u_n x_n$,

$$\kappa_e \cong \frac{2Fu_p}{V_m} (\tfrac{1}{4} K_2^2 K_3)^{1/3} p^{1/6} \tag{17}$$

3. Finally, for black zirconia with a considerable deficiency of oxygen,

$$\kappa_{ion} = \frac{2Fu_v}{V_m} (\frac{K_1}{4K_3})^{1/3} p^{-1/6} \tag{18}$$

and

$$\kappa_e \cong \frac{2Fu_n}{V_m} (\frac{K_1}{4K_3})^{1/3} p_{O_2}^{-1/6} \tag{19}$$

if $u_n x_n >> u_p x_p$.

Figure 9 shows schematically the variation of electric conductivity as a function of oxygen partial pressure, using logarithmic scales. For oxygen pressures higher than p_2 the conductivity is predominantly

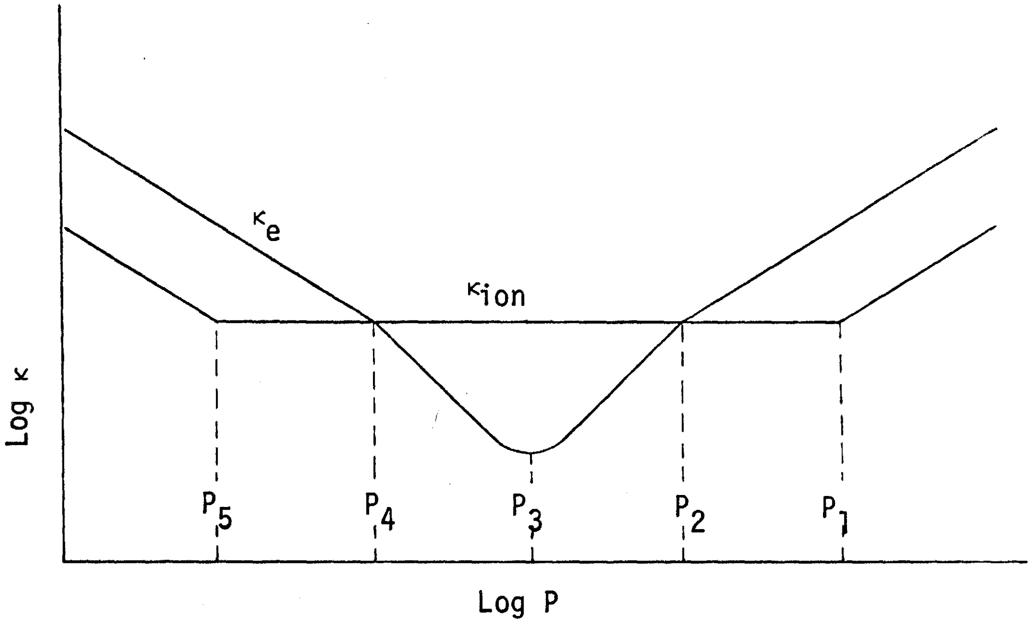

Figure 9

Dependence of partial ionic and electronic conductivities on oxygen partial pressure p. (From Douglass and Wagner(99).)

electronic, of the "p" type, i.e. electron holes are the majority carriers. At p_2 the ionic conductivity becomes equal to the electronic, and between p_2 and p_4 oxygen ions and vacancies are mainly responsible for the electric current flow. At p_3 the excess electrons carry the same portion of the electronic current as the holes, and as the oxygen pressure drops, zirconia changes from the "p" to the predominantly "n" type conductivity. When the oxygen pressure decreases to p_4, the electronic conductivity once again becomes higher than the ionic, except that now the excess electrons are the majority carriers. For oxygen pressures lower than p_5, the ionic conductivity, which was approximately constant between p_1 and p_5, starts increasing again.

The values of p_2 through p_5 depend on temperature, but are generally speaking low. Only few of them have been determined experimentally or can be estimated with any degree of confidence. Vest et al(101) experimentally determined the dependence of the electric conductivity of ZrO_2 on partial pressure of oxygen at 1000°C. They found that zirconia is an amphoteric semiconductor with the transition from "n" type to "p" type conductivity occurring at about 10^{-16} atm. In other words, at 1000°C the value of p_3 is 10^{-16} atm approximately. Other critical values for oxygen pressure quoted by Douglass and Wagner(99) are $p_2 \cong 10^{-7}$ atm, at which the ionic conductivity equals the "p" type electronic conductivity, and $p_5 \cong 10^{-21}$ atm, where the ionic and the "n" type electronic conductivities are equal. Both these values were determined at 990°C. These results support the model proposed by Douglass and Wagner, but more experimental evidence will be necessary to positively prove it.

The oxygen diffusion measurements described in this thesis were carried out at oxygen partial pressures close to atmospheric. Work of Aronson(102) indicates that at these pressures zirconia should be close to stoichiometry. On the basis of the foregoing considerations and evidence it appears reasonable to assume that the predominant defects under these conditions are of the anti-Frenkel type, i.e. that we are dealing mainly with oxygen vacancies and interstitial oxygen ions. The relation of diffusion coefficients to the corresponding electric conductivities discussed above will be shown in Chapter 5 of this thesis. At this place it should be mentioned that the development of the method for producing solid zirconia spheres provides a suitable material for the investigation of oxygen diffusivities. Accordingly additional experimental evidence may be obtained to substantiate or negate the model proposed by Douglass and Wagner(99).

2.6 Existing Information on Oxygen Diffusion in Zirconia

Oxygen diffusion in zirconia was investigated by Debuigne and Lehr(79), Douglass(86), Aronson(102), Cox(87) and McClaine(103).

Debuigne and Lehr(79) investigated the kinetics of the oxidation of zirconium between 600°C and 850°C in oxygen and in carbon dioxide. In interpreting their results they considered the competition between the formation of the oxide layer and the solution of oxygen in the metal. On the basis of experimental determination of the increases in mass of the test specimens and measurements of the thickness of the oxide layers they have determined the coefficients of oxygen diffusion in the oxide and in the metal at several temperatures. The equation which they obtained for the diffusion coefficient of oxygen in a zirconia layer on a metal substrate is

$$D = 1.05 \times 10^{-3} \exp(-29300/RT).\ \text{cm}^2/\text{sec}$$

Douglass(86) used a different method for his measurement of the oxygen diffusivity. Substoichiometric, black zirconia specimens were obtained by hot pressing zirconia powder in a graphite die under vacuum at 3000 psi and 2000°C to form cylinders 2" dia. x 3" long. The die was coated with boron nitride to prevent the reaction between oxide and carbon. The zirconia cylinders were then sectioned into rectangular slabs and placed in a stream of flowing oxygen at the desired temperature for various times. The slabs were then sectioned transversely, mounted in Bakelite, ground and polished. The diffusion zones were photographed under polarized light. However, the analysis of the diffusion of oxygen in zirconia presented a problem due to the extremely rapid grain boundary diffusion. The equation given for the oxygen diffusivity in zirconia $Zr\,O_{1.955}$ was:

$$D = 5.55 \times 10^{-2} \exp(-33400/RT).\ \text{cm}^2/\text{sec}$$

Aronson(102) measured the oxygen diffusivity using a fine sub-stoichiometric zirconia powder with an approximate average particle size of 0.25μ. Oxidation measurements were performed gravimetrically. The resulting Arrhenius plot is shown in Figure 52, page 136 of this thesis. The activation energy for the process was found to be 58000 cal/mole.

The technique used by Cox(87) consisted in oxidizing zirconium specimens completely or partially in 50% oxygen O^{17}. The specimens were then irradiated with He^3 ions which produced α-particles emitted from the O^{17} $(He^3, \alpha)O^{16}$ reaction. By measuring the intensity of the α-radiation as a function of energy, it was possible to determine the concentration of O^{17} as a function of depth in the zirconia scale. Since the results fitted either an error function curve (volume diffusion) or an exponential curve (line diffusion), it was not possible to use the shape of the curve as an indication of the type of the diffusion process. The effective average coefficients of oxygen diffusion in zirconia calculated from Cox's data are 2.52×10^{-14} cm^2/sec at 400°C and 1.13×10^{-12} cm^2/sec at 500°C. A straight line representing the diffusivity as a function of temperature, passing through these 2 points is shown in Figure 52 .

McClaine(103) estimated a magnitude for the intrinsic diffusivity of oxygen in zirconia by assuming that the energy of formation for an oxygen vacancy was 2 ev (≈46000 cal/mole). Thus,

$$V_o = N_o \exp(-2/kT),$$

where V_o = oxygen vacancy concentration per cm^3,

N_o = number of oxygen atoms per cm^3

$\exp(-2/kT)$ = fraction of oxygen atoms with sufficient energy to move into the surface sites leaving vacancies behind.

Using this equation, McClaine calculated that at 1250°K (=977°C) $V_o \approx 10^{15}$ per cm^3. Since the coefficient D of oxygen diffusion via vacancies is proportional to the vacancy concentration, D for 1250°K was estimated to be 10^{-13} cm^2/sec using the previously discussed Douglass' data for $ZrO_{1.995}$, where $V_o = 1.4 \times 10^{20}$ per cm^3. Actually, McClaine's(103) diagram, reproduced also by Cox(87), shows $D = 10^{-12}$ cm^2/sec which resulted from an error. He assumed that Douglass' equation for D was $D = 0.55 \exp(-33500/RT)$, while, according to the original paper it was $D = 0.055 \exp(-33500/RT)$. Having one point of the Arrhenius plot of D, McClaine determined then the direction of the straight line by calculating its slope as

Energy for formation of oxygen vacancies + Energy for motion of vacancies

$= 2 \text{ ev} + 1.25 \text{ ev} = 3.25 \text{ ev} \cong 75000 \text{ cal/mole}$

The result (corrected for the above mentioned error) is shown in Figure 52. The comparison between the values of oxygen diffusivities in zirconia obtained by the above investigators, and the values determined in this study will be discussed in Chapter 5.

CHAPTER 3

EXPERIMENTAL ARRANGEMENTS AND METHODS

3.1 Specimen Preparation

3.1.1 Method

Zirconia specimens used in this work consisted of small spheres, 45μ to 105μ in diameter. The spheres were made by crushing zirconia to very small pieces, sorting them to size using sieves, and dropping the particles in the 45μ to 75μ size range through an electric arc operating in an inert helium atmosphere. The particles melted, spheroidized due to surface tension and solidified in the free fall before reaching the bottom of the arc furnace.

Zirconia particles used for spheroidizing can be obtained either from ZrO_2 powder or from the metal by complete oxidation. The first method consists in pressing the powder to form tablets, sintering the tablets, crushing them and sorting to size. An attempt to utilize this method in this work was soon abandoned because of the lack of a suitable very high temperature furnace.

The second procedure for obtaining solid zirconia, namely the oxidation of high purity zirconium metal, is simple, effective in producing uncontaminated material and does not require expensive equipment. It was successfully used in this study.

To prepare the raw material for spheres, columnar white zirconia obtained by complete oxidation of the metal was crushed to the desired small size and graded using standard Tyler sieves. Crushing was done using hard tool steel dies in the first stages and an agate mortar and pestle for further diminution. Electrically operated Fisher Mortar Grinder was found very helpful in reducing the amount of labor required.

3.1.2 Furnace for Oxidation of Zirconium

The furnace and the auxiliary equipment built by the author for the oxidation of zirconium metal is shown in Figure 10. Figure 11 shows the schematic arrangement of this apparatus.

The furnace was of the electric resistance type, with Kanthal elements, capable of producing temperatures up to 1400°C. The temperature was indicated and controlled by a Honeywell Pyr-O-Vane instrument using a Type S (platinum vs. platinum + 10% rhodium) thermocouple. The oxidation chamber of the furnace consisted of a mullite tube whose one end was connected to a vacuum pump, an oxygen supply cylinder and a manometer. Oxygen exhausted to the atmosphere through the other end of the tube and through a bubbler containing low vapour pressure vacuum pump oil. Both ends of the mullite tube were cooled to protect greased glass joints and stopcocks, by air blast produced with compressed air flowing through perforated copper tubing coils. The rate of oxygen flow could be accurately controlled using a needle valve located between the pressure regulator on the gas cylinder and the stopcock at the inlet to the furnace tube.

To obtain white zirconia, high purity zirconium metal sheet, one or two millimeters thick, was first cut into strips, about 3/8 in. wide and 4 in. long. These specimens were carefully cleaned with solvents to remove any surface contamination. The analysis of the metal, 99 w/o

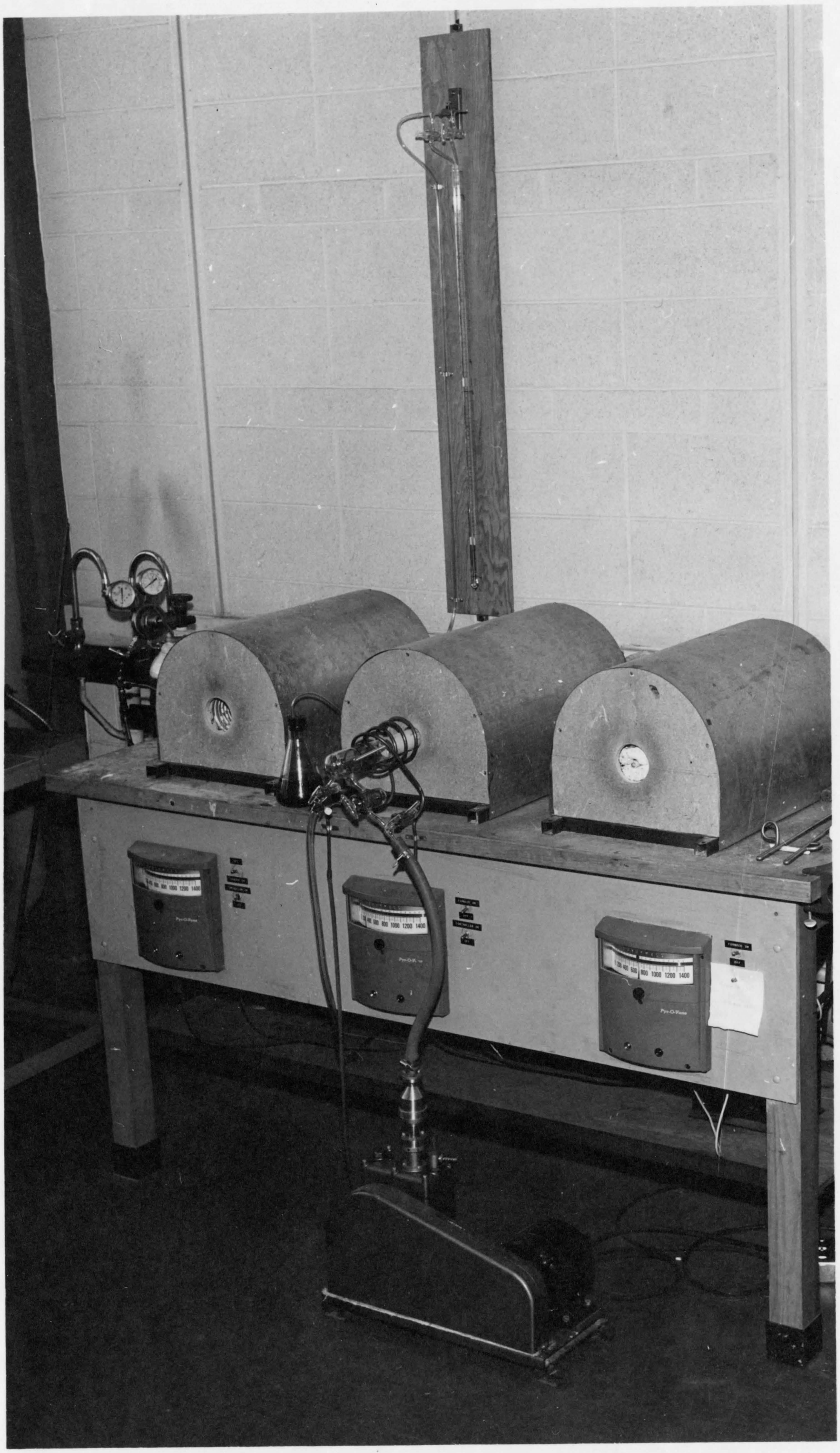

Figure 10

Furnace for oxidation of zirconium and the associated equipment (in the centre of the photograph)

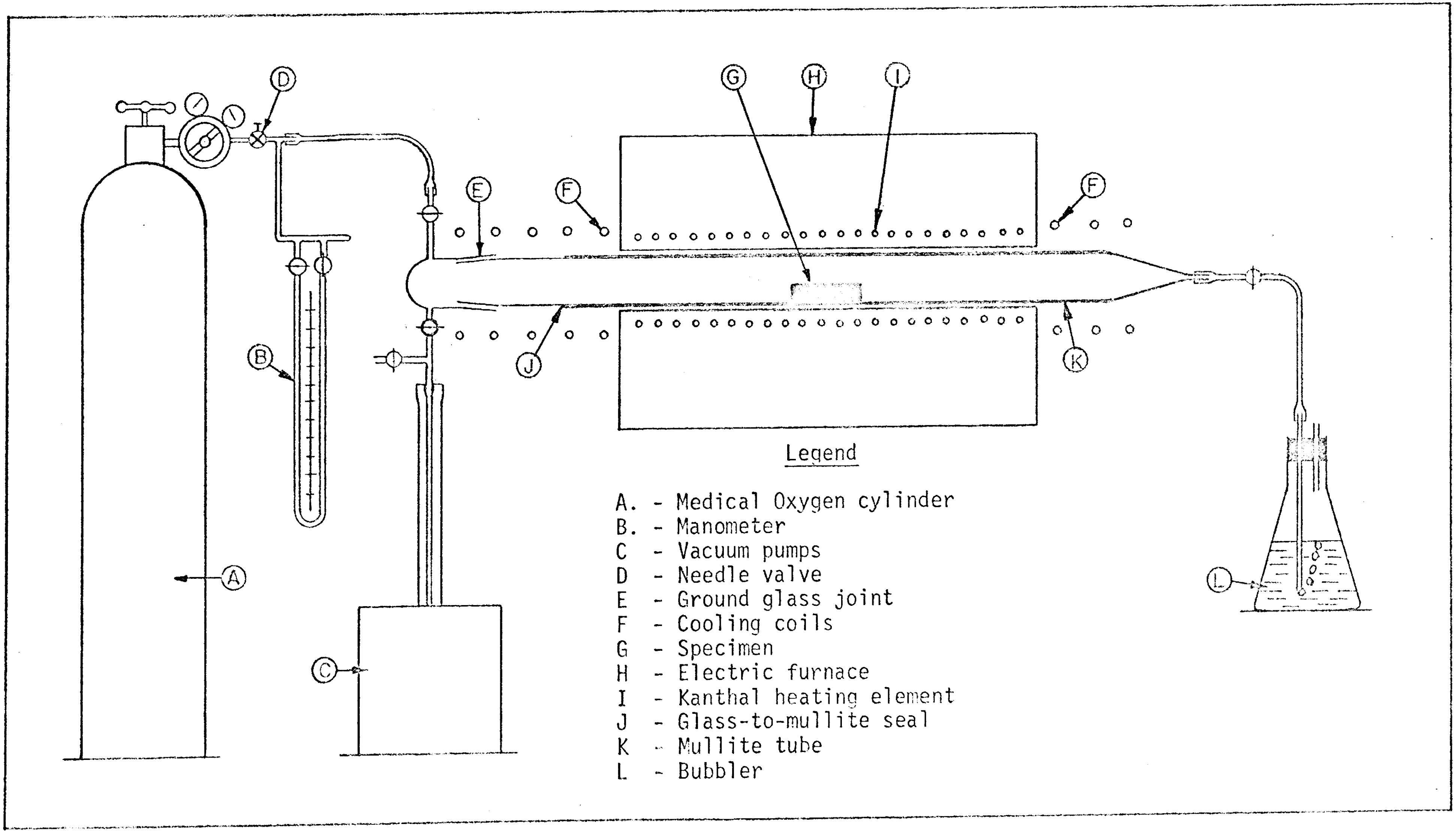

Figure 11

Schematic diagram of the furnace for oxidation of zirconium and re-oxidation of black spheres.

zirconium, is given in Table 2. Several of these strip specimens were oxidized completely to white zirconia in each oxidation operation by placing them in the middle of the mullite furnace tube and exposing them to a flowing atmosphere of medical grade oxygen at 1200°C.

3.1.3 Arc Furnace for Spheroidization of Zirconia

The electric arc furnace used for the spheroidizing treatment is shown in Figures 12 and 13. It was equipped with graphite electrodes and a graphite body in the hot zone, connected to a Vycor glass tube in the lower, cooler part of the furnace. Ceramic "Pyro-phyllite" bushings provided electric insulation for the electrodes. One of the electrodes was stationary, while the other could be moved manually by means of a fiberglass handle to adjust the length of the arc. At the lower end, the Vycor tube terminated at a hollow aluminum ring which had one helium inlet tube and 12 outlet orifices providing a uniform distribution of the gas around the internal periphery of the furnace. A flat aluminum disc formed the bottom of the furnace where the spheres and the irregular particles which missed the arc collected after passage through the furnace. The plate could be easily removed to retrieve this solid product by unscrewing three wing nuts securing it to the furnace. Two silicone rubber O-rings made the lower part of the furnace gas tight: one between the aluminum ring and the Vycor tube, and the other between the ring and the bottom plate. This was found necessary to prevent air from being displaced into the furnace by the upward helium flow. The upper part of the furnace was not gas tight, allowing helium to escape during the furnace operation when a small flow of gas was

TABLE 2

Chemical Analysis of Zr Metal Used for Producing Zirconia

Element	Content,* ppm
Al, Cu, Ti	25
Mg, Mn, Sn	10
Co, Pb, V	5
C	30
H	2.2
Fe	210
Hf	60
O	140
N, Ni	1.0
Cd	0.3
Si	85
W	25
Zn	50

* After AECL, Chalk River

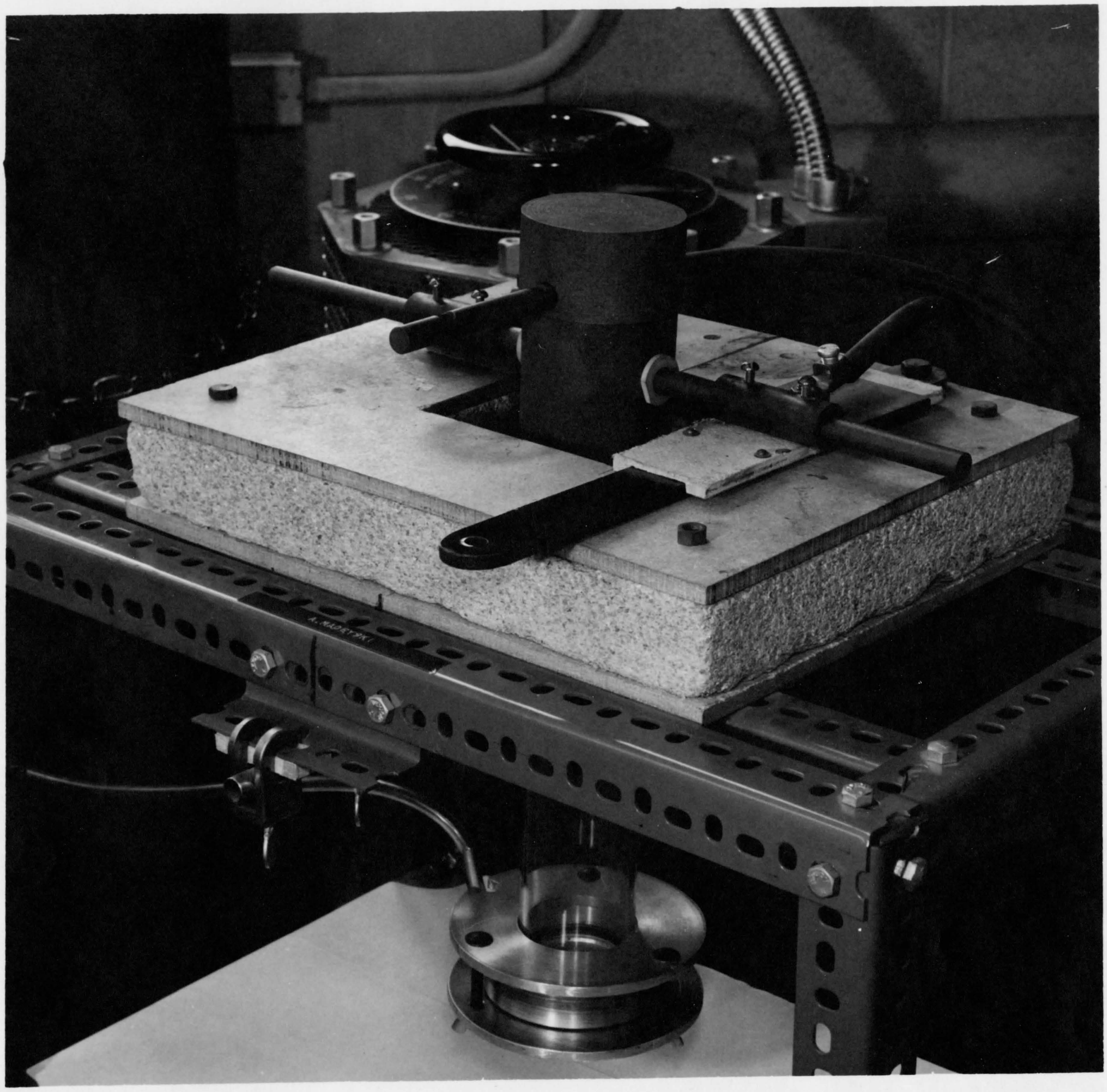

Figure 12

Electric arc furnace for spheroidization of zirconia.

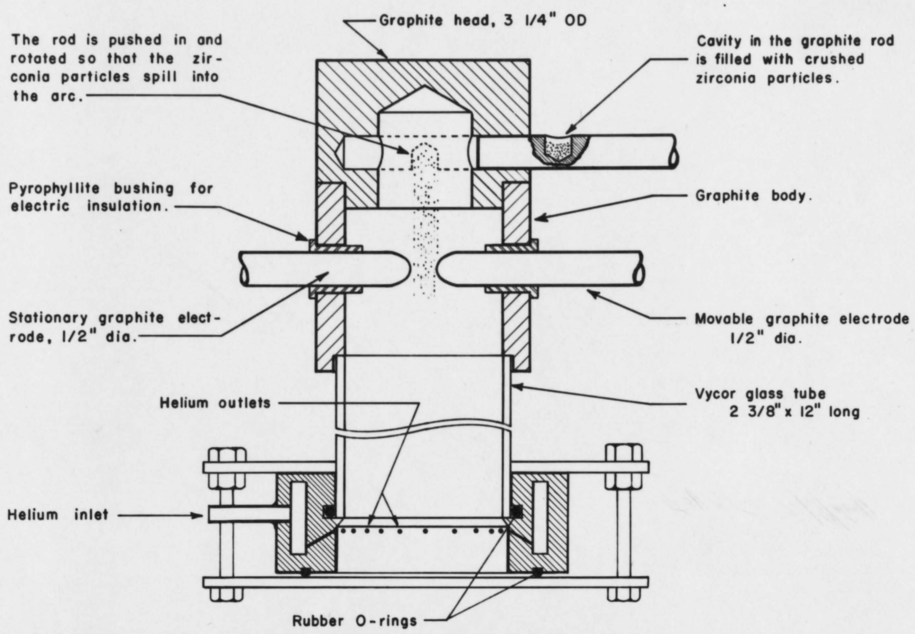

Figure 13

Schematic cross-section of the arc furnace.

maintained for reasons explained in Section 4.2.

The arc length used for spheroidizing was approximately 3/8 in. at 90 volts and 55 amps. Direct current was used to provide an uninterrupted arc. One of the difficulties in the original design of the furnace was connected with the feeding of the zirconia particles into the arc. The powder was dropped through a funnel-like silica glass tube, shown in Figure 14 but thermal current from the arc blew a large portion of the feed right out of the furnace. The design was changed then to that shown in Figure 13.

The graphite rod was pulled out part way until its cavity was outside the furnace head. The cavity was then filled with zirconia and the rod was pushed in and turned by 180° spilling the powder into the arc.

The operation of the arc furnace was always started by blowing helium through the bottom of the furnace at a high rate to thoroughly purge the arc region of air. Approximately ten cubic feet of helium were sufficient for this purpose. This stage was very important because nitrogen, even in small quantities, led to the formation of defective spheres. To control the helium flow, the Tygon hose from the pressure regulator on the gas cylinder had two branches. One was completely unobstructed, while the other included a micrometer needle valve. During the initial purging of the furnace, both branches were open to provide a high rate of helium flow necessary for good turbulence. When this stage was completed, the unobstructed branch was closed with a simple pinch clamp. This reduced the flow to a very small rate critically adjusted using the micrometer needle valve

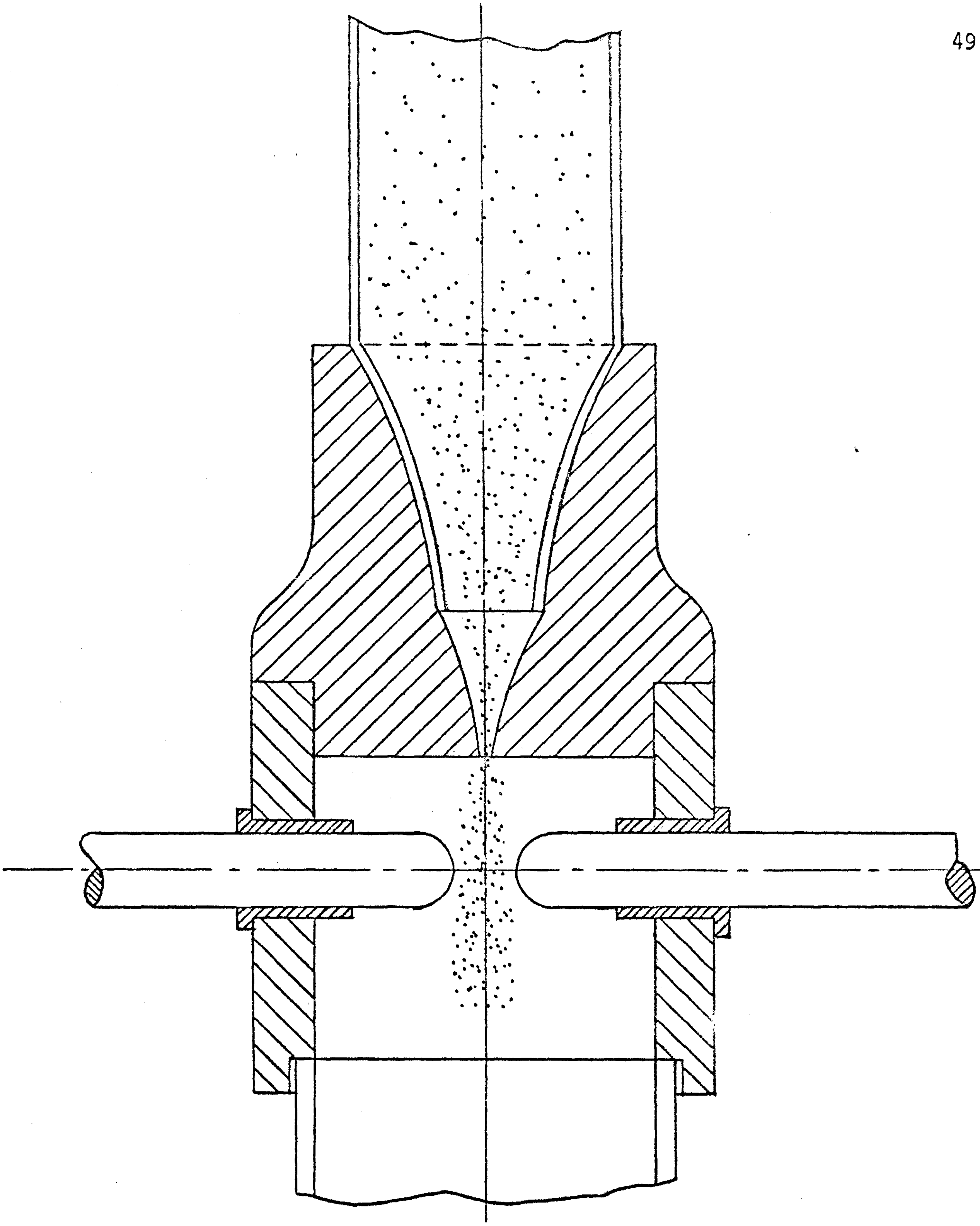

Figure 14

Original design of the arc furnace feeder. Full size.

because an excessive rate of flow interfered with the passage of the zirconia powder through the arc or could even blow out the arc. On the other hand, a sufficient flow rate was required to maintain a positive pressure inside the furnace for effective removal of air introduced with the powder charge, and of the carbon oxides produced in the reduction process. Fortunately, it was not necessary to readjust the valve for each furnace operation.

When the furnace was being purged, the graphite rod, used for feeding zirconia, was removed to allow air and helium to escape. As soon as the helium flow rate was reduced, the rod was replaced and the arc was started. This was done without opening the furnace by simply bringing the electrodes to about 1/32 in. from each other and touching the graphite rod with the tip of a Tesla coil. Short-circuiting of the electrodes was avoided to protect the power supply unit. The arc was drawn to its full operating length of 3/8 inch by shifting the moveable electrode.

The cavity in the graphite rod was then charged with zirconia and the rod was pushed in and held over the arc for about 2 minutes to desorb the entrained air which was carried away by the flowing helium. The rod was subsequently rotated slowly by 180°, gradually spilling the zirconia powder into the arc. After the furnace had been in operation for some time, it was necessary to clean the electrodes. Some of the zirconia adhered to the white hot graphite, melted, and decreased the amount of carbon vapour available for the reduction process. In practice, it was found most convenient to have a few spare electrodes which could be used to replace the contaminated ones. The exchange took less than a minute, and the removed electrodes could be later easily dressed using a sander.

3.1.4 Separation of Spheres

The separation of the spheres from the irregular zirconia particles which entirely or partially missed the arc, was done by rolling them down an incline. A Bristol board trough was used originally, but its surface was somewhat rough for the size of the powder. Furthermore, with all the particles moving in the same direction, the spheres tended to be blocked by the other particles. Much better results were obtained when the powder was dropped on an inverted watch glass, as shown schematically in Figure 15. When the glass was vibrated slightly, the particles spread in all directions and the spheres were free to roll off the edges into another, larger watch glass placed with the concave side up. The watch glasses had to be carefully washed before use because zirconia spheres tended to stick to greasy spots. For the same reason, the operator had to wear fabric gloves to prevent leaving fingerprints. Cotton gloves were found superior to nylon because the latter produced static electricity on the glass which caused the spheres to stick together or move irregularly. On particularly dry days, when a static charge gradually built up on the glassware, breathing gently on the surface was found very effective. Presumably, thin film of moisture conducted and neutralized the charges from the glass surface and from the spheres, and then evaporated within a few seconds leaving spheres dry and rolling freely.

3.1.5 Furnace for Re-oxidation of Sub-stoichiometric Spheres

Zirconia spheres produced in the arc were oxygen deficient for

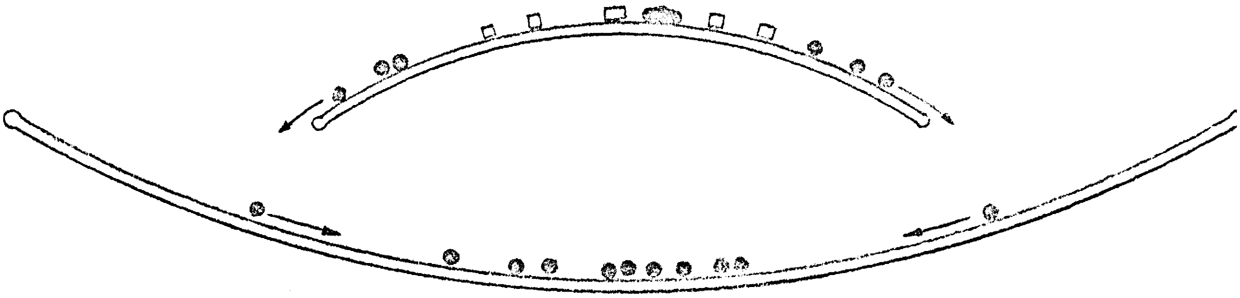

Figure 15

Schematic diagram of the method of sphere separation from irregular zirconia particles.

reasons discussed in Section 2.4. To re-oxidize them from black, sub-stoichiometric to white, fully stoichiometric oxide, they were heated in oxygen in the furnace shown in Figures 10and 11. The black spheres were placed in platinum crucibles, shaped to fit the inside of the mullite tube of the furnace. The tube was thoroughly evacuated of air, and pure, medical grade oxygen was admitted. The re-oxidation was done at 850°C, followed by an overnight annealing at the same temperature to diffuse out and oxidize any traces of carbon and to homogenize the structure. The spheres were then cooled with the furnace to minimize the stresses.

3.2 Atmosphere Preparation

3.2.1 Method

The atmosphere for the self-diffusion measurements consisted of oxygen O^{16} containing 1.3 a/o of the non-radioactive isotope O^{18}. Natural abundance of this isotope in the oxygen of the air is 0.2 a/o.

This atmosphere was prepared by electrolysis of O^{18}-enriched water. To increase the electric conductivity of the water, potassium fluoride was added. More commonly used salts such as sulfates, were not employed because they contain oxygen which could exchange with O^{18} reducing the concentration of this isotope in the atmosphere produced. Chlorides were discarded, to avoid possible contamination of the oxygen with chlorine. Sodium fluoride was considered, but its maximum solubility in cold water was found to be only 4.2% by weight, compared to 92.3% for potassium fluoride. However, before using potassium fluoride it was necessary to determine the relation between the concentration of this salt in water and the electric conductivity of the solution, since no information on the subject was available in literature. On the basis of the measurements described in Appendix 1, it was decided to use 15 w/o as the initial concentration of KF in the water.

3.2.2 Apparatus for Electrolysis of O^{18} Enriched Water

The apparatus for the electrolysis of the O^{18} enriched water is shown in Figures 16 and 17. It consisted of a vertical electrolysis vessel with platinum sheet electrodes suspended on platinum wires. The vessel had provisions for cooling of the isotopic water and of the vessel walls using iced water. The purpose of the cooling was to reduce the amount of evaporation during the initial evacuation of the space above the water, as well as during the electrolysis when large amounts of heat were produced by the electric current.

The first step in the electrolysis procedure was to chill the isotopic water and to evacuate the space above the water using a mechanical vacuum pump. Medical grade oxygen was then admitted to the vessel and pumped out again to purge nitrogen and other impurities from the air. This procedure was repeated ten times, after which the "hydrogen" chamber of the vessel was isolated from the rest of the system, while the "oxygen" chamber was connected only to the portion of the apparatus containing a manometer and the first cold trap. The electrolysis was then started using a small initial current to prevent excessive bubbling and foaming which led to large isotopic water losses in the form of vapor and fine spray. As the oxygen pressure was built up, the electrolysis current was gradually increased to 2 amp. Oxygen was then periodically bled to the rest of the purifying system and to

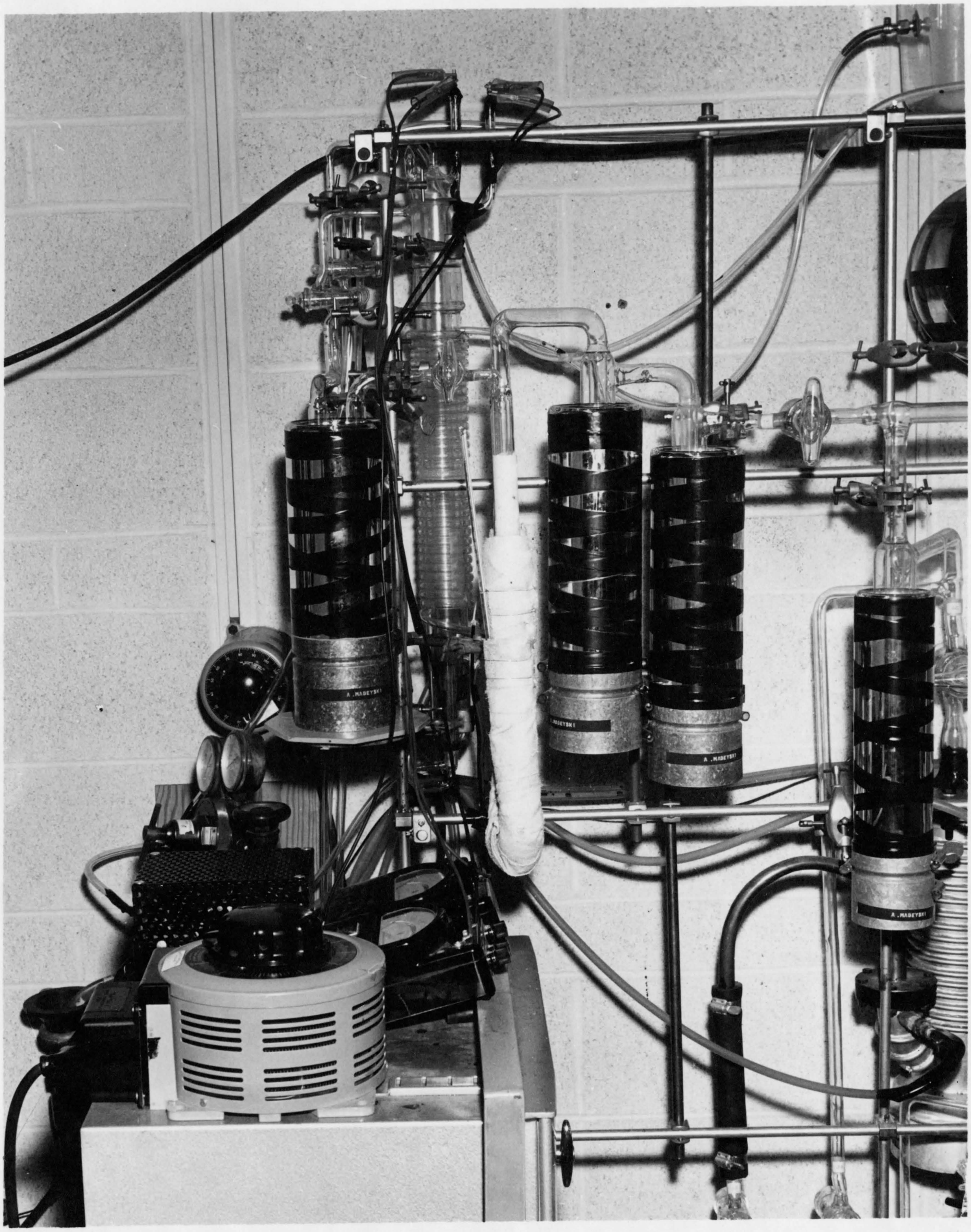

Figure 16

Isotopic water electrolysis portion of the apparatus.

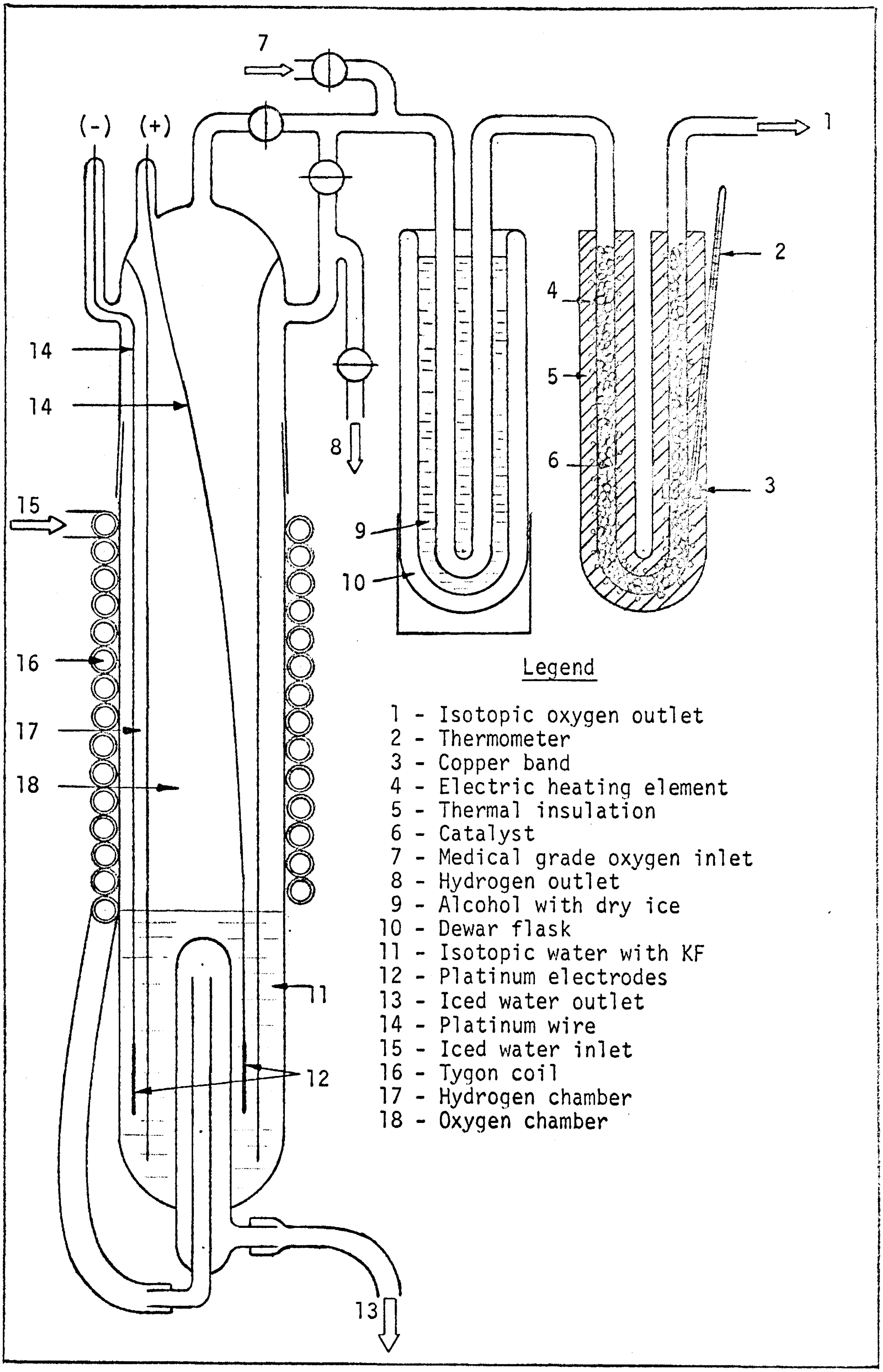

Legend

1 - Isotopic oxygen outlet
2 - Thermometer
3 - Copper band
4 - Electric heating element
5 - Thermal insulation
6 - Catalyst
7 - Medical grade oxygen inlet
8 - Hydrogen outlet
9 - Alcohol with dry ice
10 - Dewar flask
11 - Isotopic water with KF
12 - Platinum electrodes
13 - Iced water outlet
14 - Platinum wire
15 - Iced water inlet
16 - Tygon coil
17 - Hydrogen chamber
18 - Oxygen chamber

Figure 17

Schematic diagram of the portion of the apparatus for isotopic water electrolysis.

the collector bulbs. Hydrogen was removed from time to time by a vacuum pump which exhausted to the atmosphere outside the building.

The purification of the isotopic oxygen consisted of passing it through an alcohol - dry ice cold trap, a catalyst and two liquid nitrogen cold traps. The purpose of the first cold trap was to remove, liquify and solidify the isotopic water vapor, which was later returned to the chilled electrolysis vessel by removing the dewars from the cold trap and boiling the water away using an electric tape heater. The copper oxide catalyst removed traces of hydrogen from the oxygen stream by converting it to water vapor which was frozen out in the next cold trap. Since liquid nitrogen was used to cool it, carbon dioxide was also solidified here. Oxygen, which liquified in this cold trap, was later gradually boiled away by temporarily removing the dewars. It passed into the second cold trap, and was later similarly transferred to the collector bulbs.

The catalyst used was "BTS" made by the Badische Anilin and Soda Fabrik A.G., Ludwigshafen am Rhein, Germany. It consisted of copper oxide in a very finely dispersed form stabilized on a carrier. It was electrically heated to 200°C during the operation of the system. It was found that the catalyst had a large amount of nitrogen adsorbed on it which was gradually released contaminating the oxygen. This was eliminated by heating the catalyst to 250°C under vacuum for a number of days and purging it periodically with medical grade oxygen.

3.3 Oxygen Diffusion

3.3.1 Method

The measurement of the oxygen self-diffusion in zirconia consisted in holding zirconia spheres at a desired temperature in an atmosphere containing 1.3 a/o of O^{18} in O^{16} which corresponded to 2.6 v/o of the molecules $O^{18}O^{16}$. Since the spheres were previously annealed in an atmosphere of O^{16} containing only the natural abundance of O^{18} which is 0.2 a/o, more O^{18} diffused into the spheres than diffused out during the experiment, until the concentrations of O^{18} in the solid and in the gas became equal. By periodically taking samples of the atmosphere in the diffusion chamber, and determining the ratio of the number of $O^{16}O^{18}$ molecules to $O^{16}O^{16}$, it was possible to follow the progress of self-diffusion of oxygen in zirconia and to calculate the coefficient of self-diffusion.

3.3.2 Apparatus for Oxygen Diffusion

The oxygen diffusion portion of the apparatus is shown in Figures 18 and 19. An overall picture embracing the gas preparatory and purification train is shown in Figure 20.

The diffusion chamber consisted of a platinum-rhodium alloy tube, 20 mm in diameter, and 380 mm long, closed at the lower end and attached to a glass tube by means of a graded seal at the upper end. The glass tube could be connected to the vacuum manifold, oxygen O^{18} reservoir or the sample collector, as required, by opening corresponding stopcocks. The top of the glass tube carried a ground glass joint whose upper part contained a glass winch for lowering or raising a platinum crucible with zirconia spheres. The crucible, which was suspended on a thin platinum wire, was 12 mm in diameter and 15 mm high.

The platinum tube was located inside a ceramic tube made of

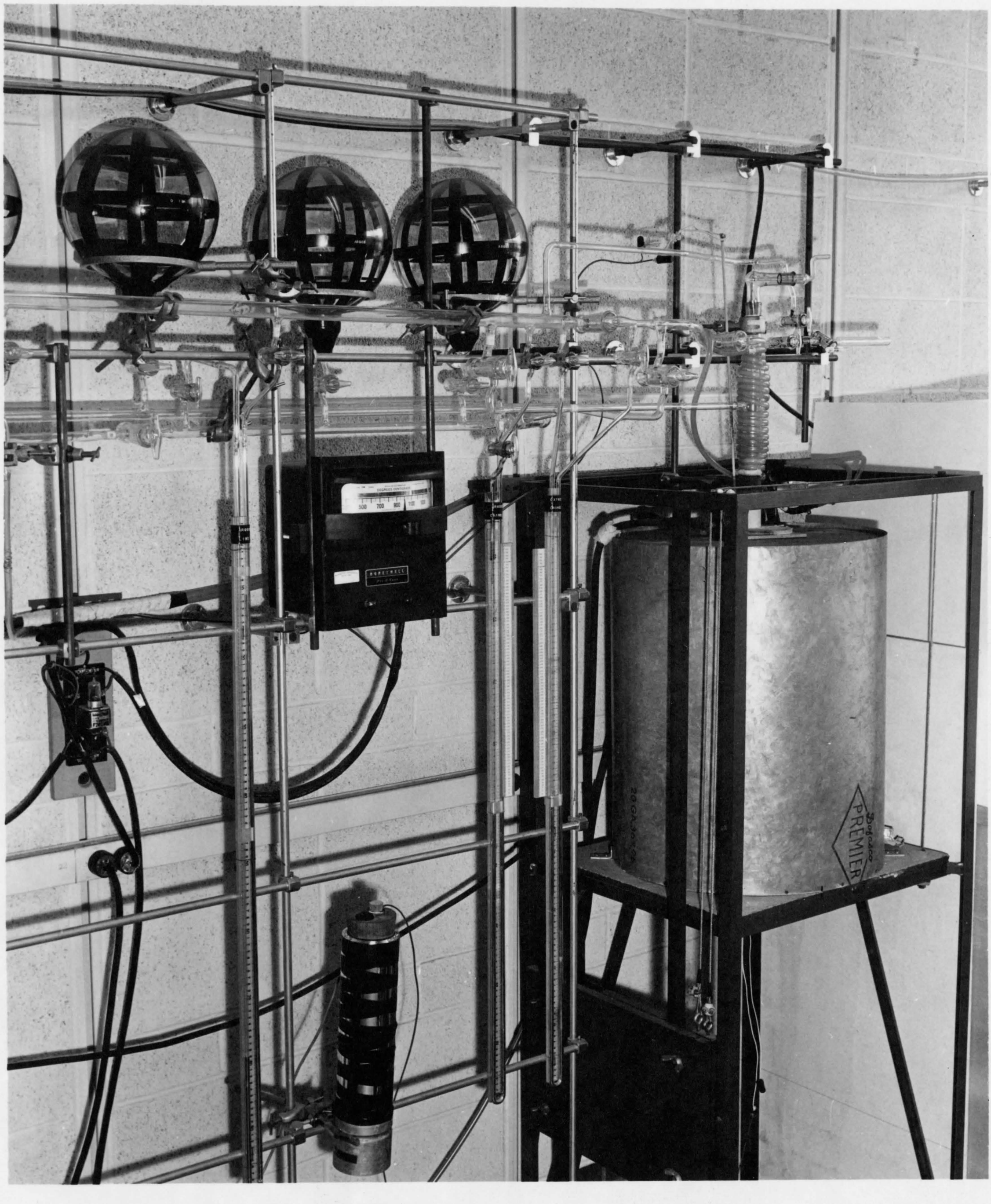

Figure 18

Oxygen diffusion portion of the apparatus.

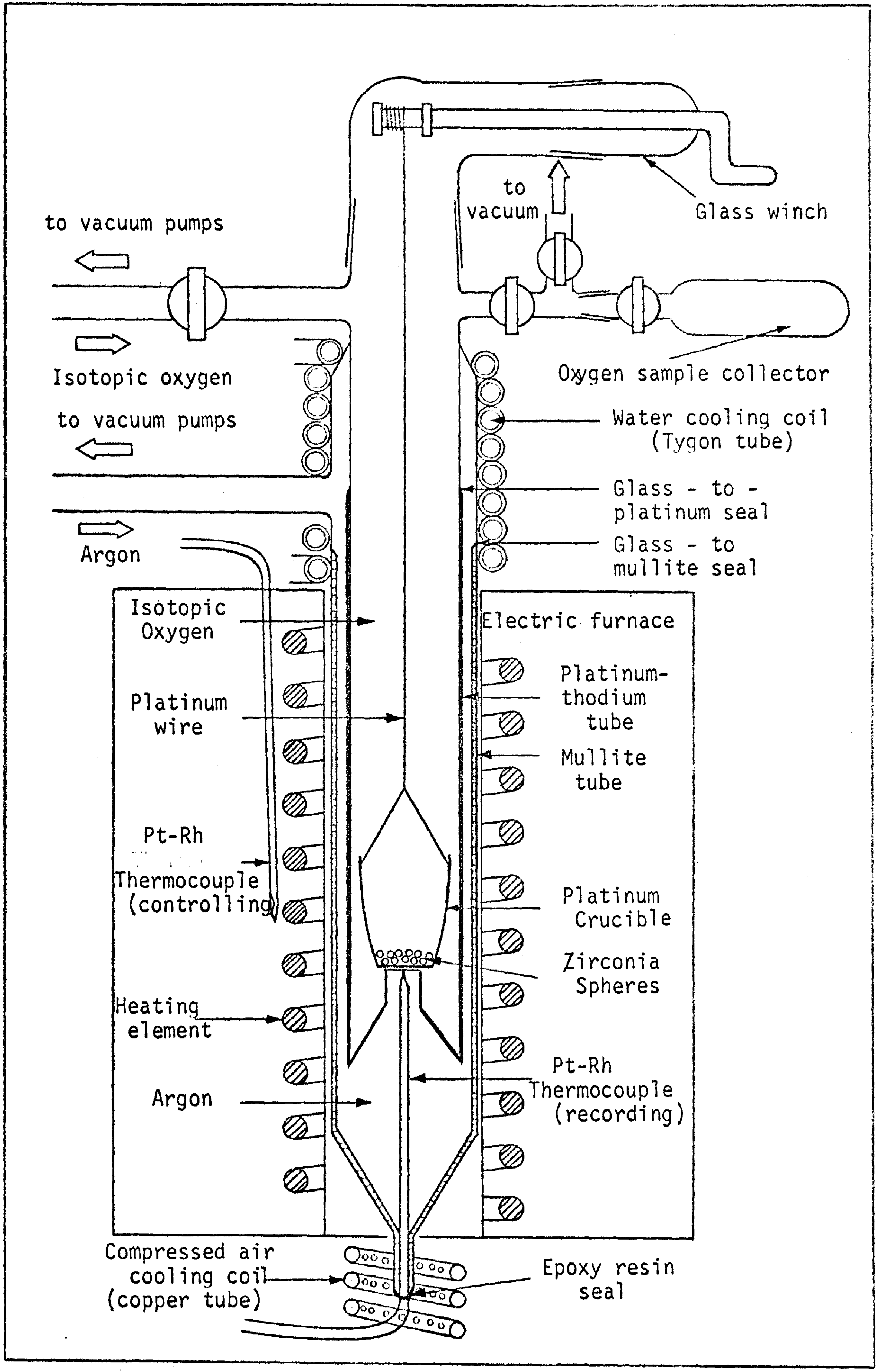

Figure 19

Schematic diagram of the diffusion portion of the apparatus.

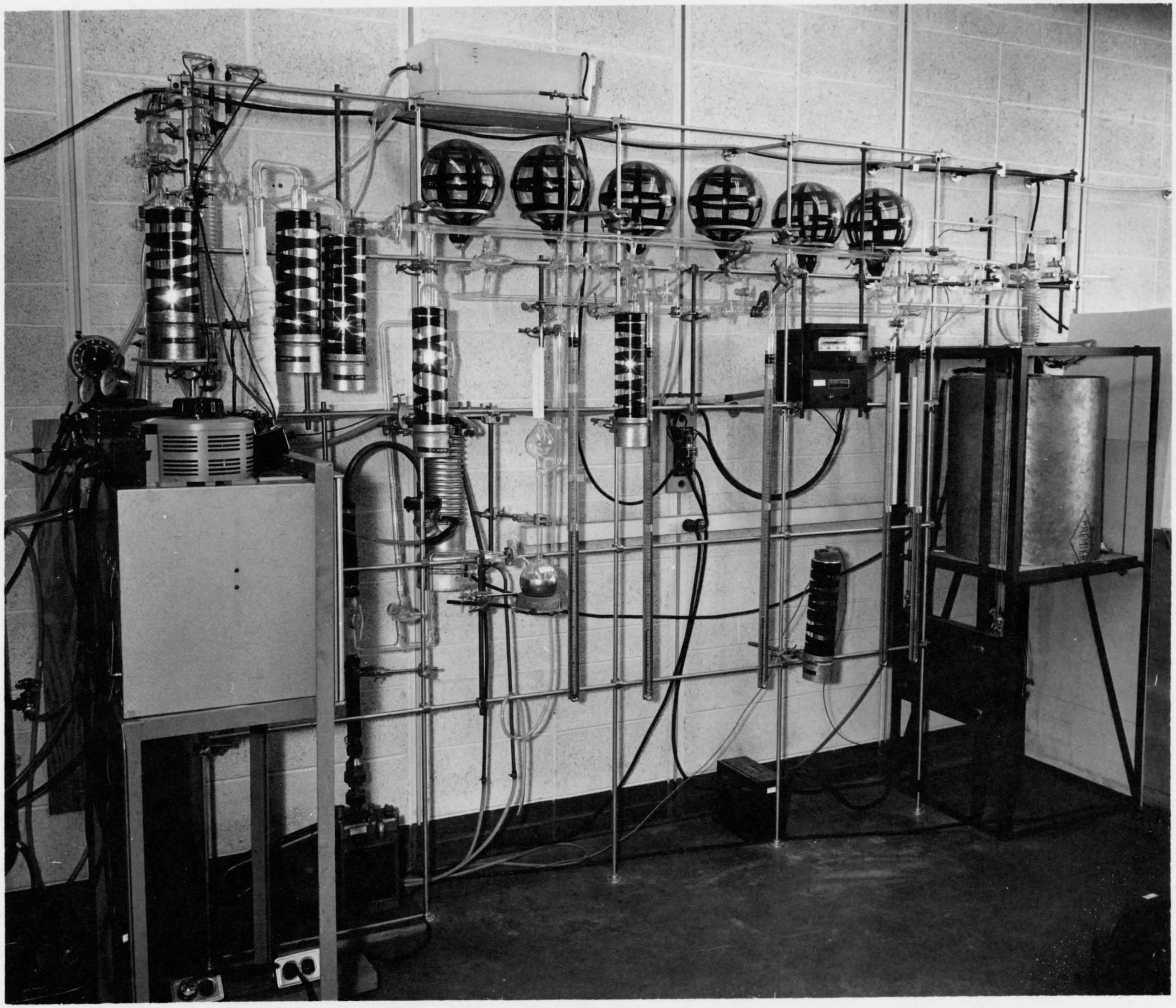

Figure 20

General view of the apparatus.

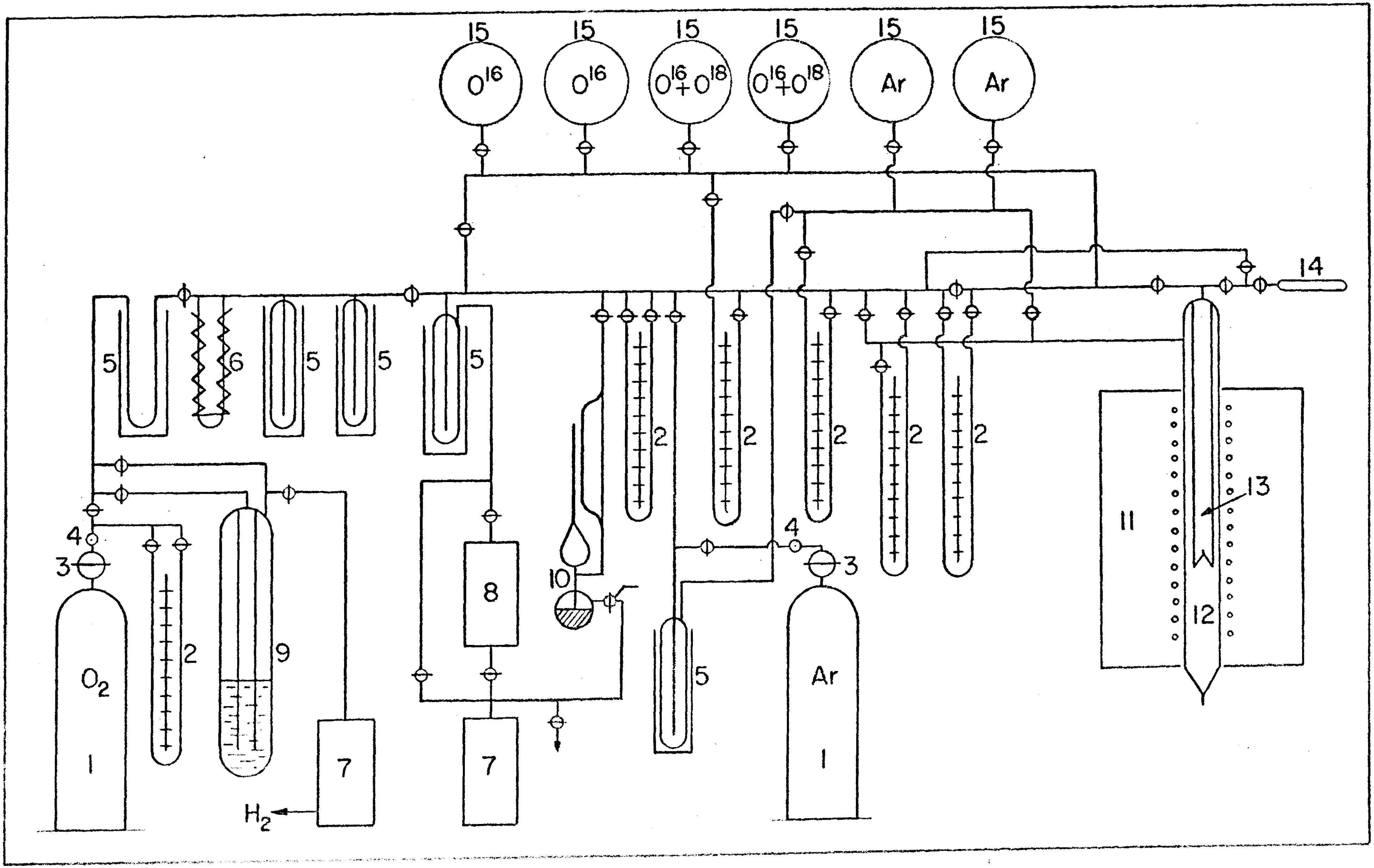

Figure 21

General schematic diagram of the apparatus.

Legend for Figure 21

1. gas cylinder
2. manometer
3. pressure regulator
4. needle valve
5. cold trap
6. heated catalyst
7. mechanical vacuum pump
8. diffusion vacuum pump
9. electrolysis unit
10. McLeod gauge
11. furnace
12. mullite tube
13. platinum diffusion chamber
14. gas sample collector
15. gas reservoir

gas impervious mullite. This outer tube could be connected to the vacuum manifold or argon reservoir as necessary. The ceramic tube was filled with argon at the same pressure as oxygen inside the platinum tube. This served two purposes: a) prevented the collapse of the thin-walled platinum tubing at a high temperature if the oxygen pressure inside it was lower than atmospheric, and b) eliminated the possibility of diffusion of contaminants, such as hydrogen, from the atmosphere into the diffusion-anneal chamber. The gas pressures inside the two tubes were measured with mercury manometers.

Both tubes were inside a 2500 watt electric resistance furnace with a Kanthal element and Vermiculite insulation. The furnace, which was 19 in. diameter x 23 in. high, was supported on a moveable counter-weighted platform for easy lowering and removal for repairs. The temperature inside the furnace was measured and controlled by an "S" type (platinum vs. platinum plus 10% rhodium) thermocouple and a Honeywell Pyr-O-Vane temperature compensated proportional controller with a range of 300°C to 1400°C.

The actual temperature of the zirconia spheres was measured and recorded by another platinum vs. platinum - rhodium thermocouple and a Philips "Automatic Compensator" recorder. The hot junction of this thermocouple was welded to the bottom of the platinum tube diffusion-anneal chamber, in a special well almost touching the crucible in its normal position during the diffusion (see Figure 19).

The graded seals between the platinum tube and glass, and between the mullite tube and glass, as well as the glass tube just above the furnace were cooled by means of a Tygon hose wrapped around them and carrying cold tap water. This was done to prevent the cracking of the seals due to excessive expansion and to prevent possible exchange of the isotopic oxygen with a hot glass. Previously used method of cooling which consisted in using water - carrying copper tubing embedded in Thermon cement was unsuccessful because the hard and rigid cement introduced high thermal stresses in the glass and eventually lead to a failure of both seals.

3.4 Atmosphere Analysis

3.4.1 Method

To record the progress of diffusion in the zirconium dioxide spheres, samples of the atmosphere in the diffusion chamber were periodically taken and analyzed for the concentration of the mass 34 molecules (oxygen $0^{16}\ 0^{18}$). The analyses were performed using a mass spectrometer.

3.4.2 Mass Spectrometer for Atmosphere Analysis

The mass spectrometer chosen for the analysis of the isotopic oxygen was a 180° Nier type instrument designed and made at the McMaster University. The sample line and analyzer of this spectrometer are shown in Figure 22, while the power control unit, recorder, vibrating reed electrometer and the mass spectrum scanning unit (small box between the recorder and the power control unit) will be seen in Figure 23. The preparation of the mass spectrometer for this project consisted in rebuilding the electronic circuitry of the power control unit and overhauling the motor-generator set (not shown in photographs) supplying the

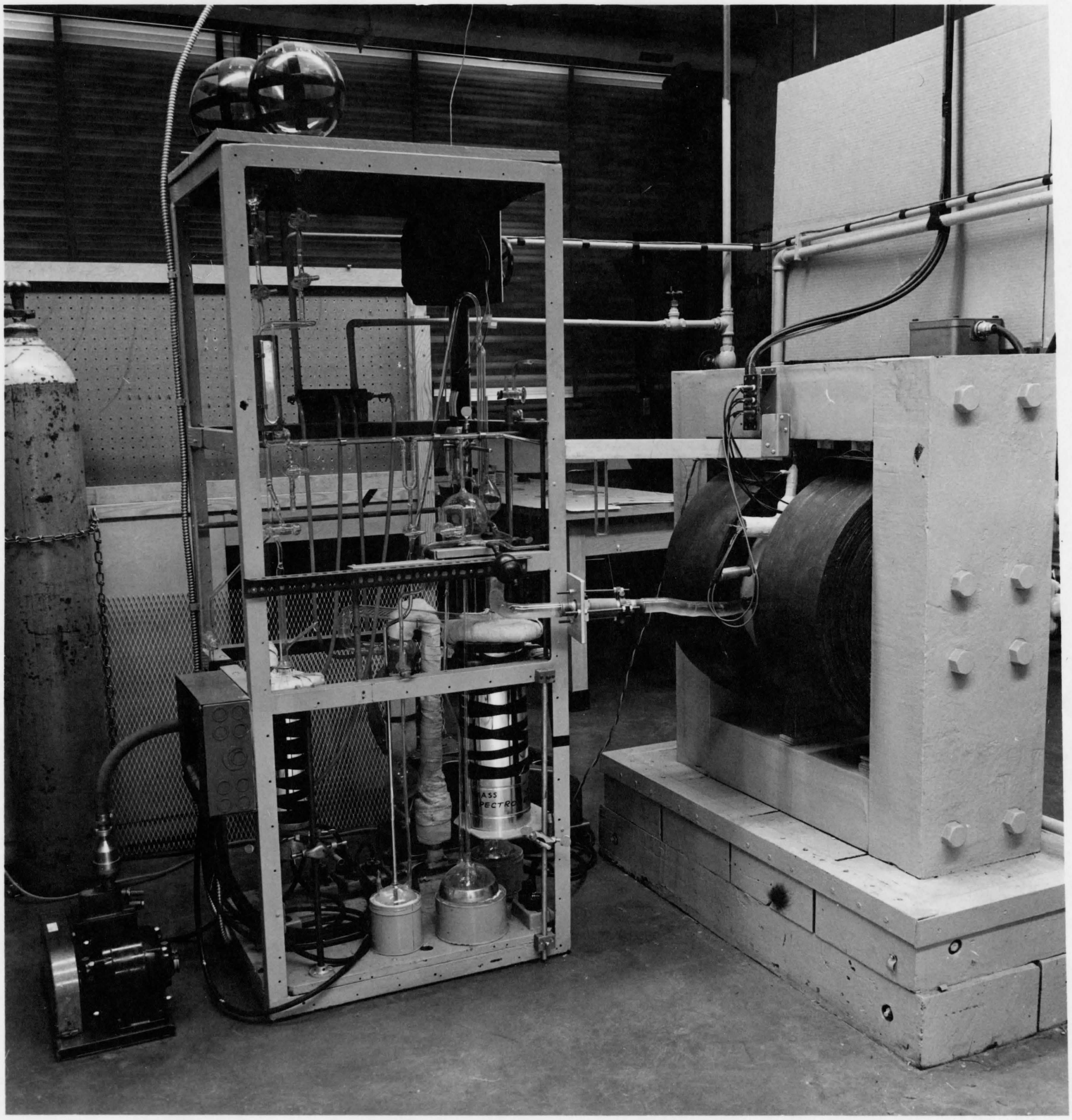

Figure 22
Sample line and analyzer of the mass spectrometer

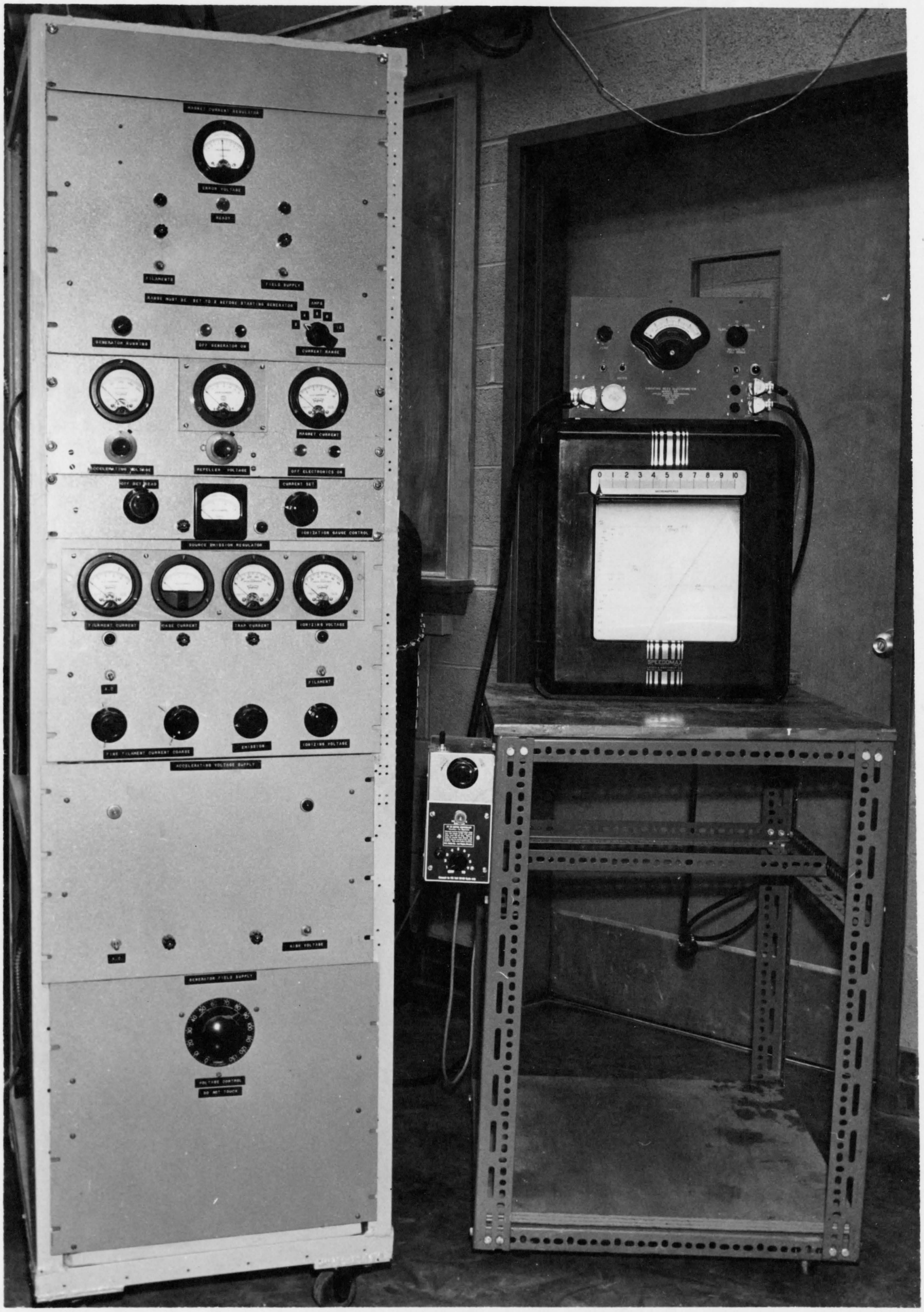

Figure 23

Control unit and recorder of the mass spectrometer. Vibrating reed electrometer is mounted on top of the recorder.

D.C. power to the electromagnet. Improvements and modifications were also made in the sample line and analyzer portion of the apparatus. For instance, a flexible bellows connection with 3 adjustable threaded supports was designed, made and installed between the sample line and the analyzer tube to allow for a precision centering of the analyzer tube in the magnetic field without breaking the vacuum. The bellows may be seen in Figure 22between the sample line frame and the glass tube leading to the magnet portion of the apparatus. Another improvement consisted in replacing the tungsten filament used for gas sample ionization, by a thoria-coated iridium strip filament. The development of the coating method and testing of the filament is described in Appendix 2 of this thesis. The change of the filament was made to extend its life in an oxygen atmosphere. Unfortunately, this mass spectrometer was used only for preliminary gas analyses. During final baking of the analyzer tube, a glass-to-metal seal failed and paraffin wax supporting the electrometer leads outside the tube melted and contaminated the vacuum system. In view of an early deadline for the completion of the project, the mass spectrometer had to be temporarily abandoned and the oxygen analyses were performed using a consolidated Electro-Dynamics Co. model M-21-103 C mass spectrometer, provided through the good offices of the Management of the British American Oil Research Laboratories, Sheridan Park, Ontario.

In this instrument the precision of determining the concentration of mass 34 particles was ± 0.02%.

CHAPTER 4

EXPERIMENTAL RESULTS

4.1 Oxidation of Zirconium

Since the oxidation of zirconium metal was carried out in this study to completion which is seldom done by other research workers, some additional interesting observations were made. Zirconium strip cross-sections, produced by fractures at various stages of oxidation, are shown in Figures 24 through 32. They are discussed more thoroughly in Section 5.1.

The specimen shown in Figure 24 was oxidized in pure oxygen at 900°C for 3 weeks. Thin layers of white and black zirconia oxide formed at the surfaces, while the rest of the strip was converted to a solid solution of oxygen in zirconium metal. Figure 25 shows a more advanced stage of oxidation of zirconium. This strip was exposed to oxygen at 1000°C for 27 days. The solid solution has now been eliminated and replaced by black, substoichiometric, and white, stoichiometric zirconia. Cracking of the white zirconia layer at the corners of some of the specimens is illustrated in Figure 26 .

A more advanced stage of oxidation is shown in Figure 27. Here, the cracking occurred primarily in the center plane of the strip. High internal stresses associated with the expansion of the metal as it oxidizes often resulted in distortion of the specimen. This is best illustrated in Figure 28. The effect of cracking on the direction of oxidation is shown in Figure 29. Figure 30 represents the end area of the center plane (parallel to both surfaces) of a completely oxidized specimen. In many cases, the two halves of the specimens separated along this center plane.

Figure 31 shows the longitudinal cross-section of a white zirconia strip produced by exposure of zirconium to oxygen at 1250°C for 18 days. The uniformity of this columnar structure is truly remarkable, and the individual grains extend through the complete half-thickness of the strip.

To utilize the specimens which were prematurely removed from the furnace before they had time to oxidize completely, the strips were broken up, white zirconia particles were separated, crushed to the desired size and used for spheroidizing in the usual way. Black zirconia particles were placed in a platinum crucible and exposed again to oxygen at 950°C. The result is shown in Figure 32.

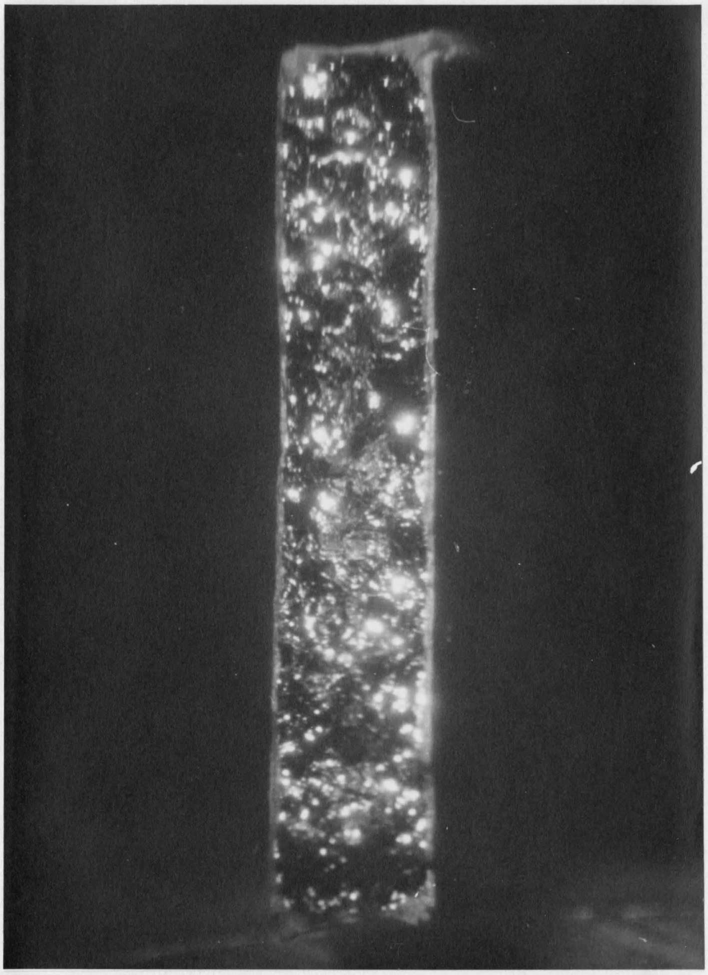

Figure 24

Fracture of zirconium strip converted to a solid solution of oxygen in zirconium with thin layers of white and black zirconium oxide at each surface. Magnification: 100x.

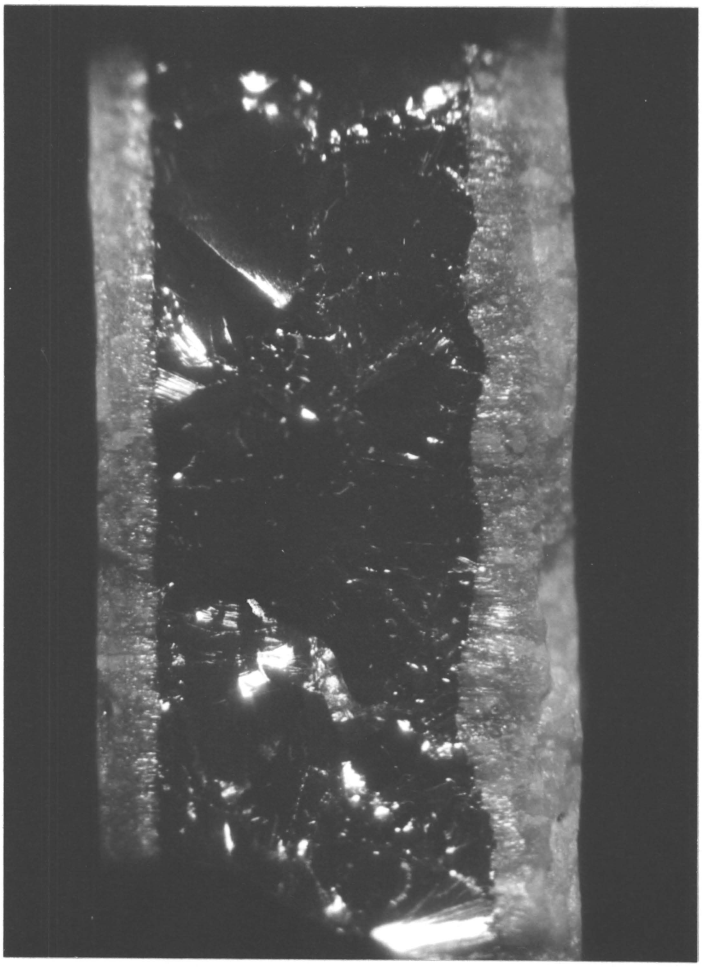

Figure 25

Fracture of a black and white zirconia "sandwich" after the metal was converted to oxide during oxidation of zirconium strip. Not etched. Magnification: 30x.

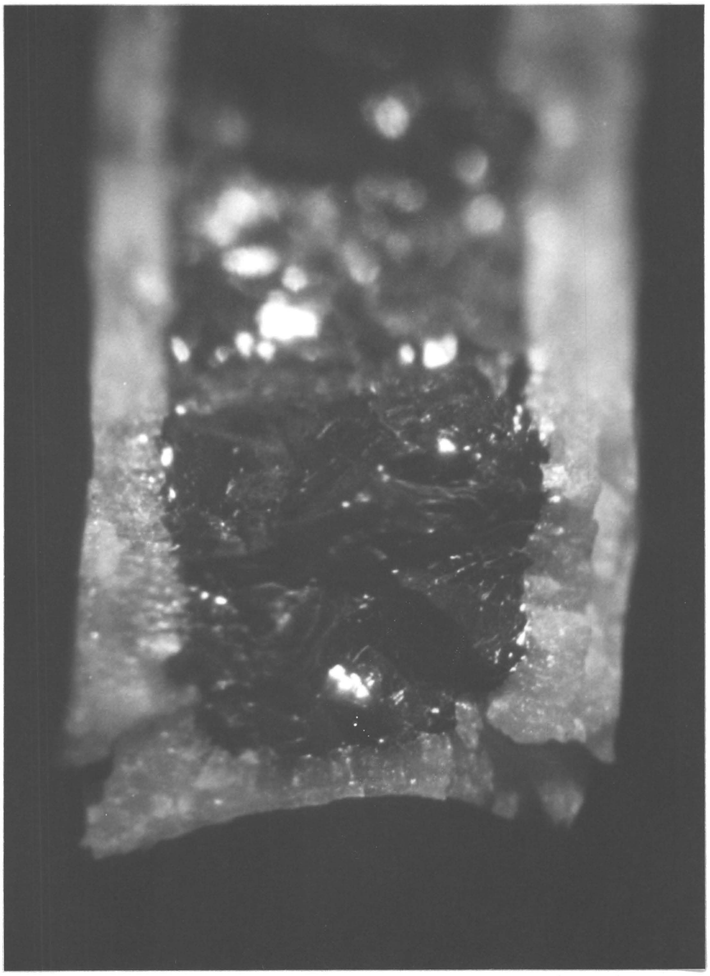

Figure 26

Black and white zirconia. Note the cracks in the white layer at the corners. Magnification: 35x.

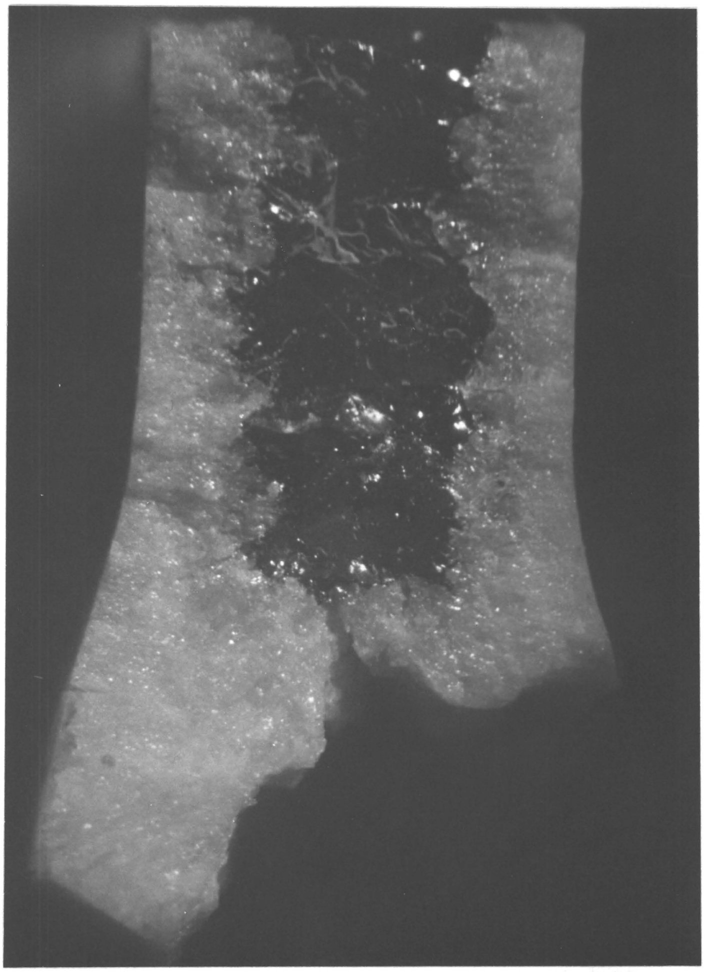

Figure 27

Black and white zirconia at a more advanced stage of oxidation. Note the crack in the white zirconia layer in the lower part of the photograph and the curving of the oxide. The extension of the white zirconia layer to the right of the crack broke off. Magnification: 25x.

Figure 28

The end of a zirconium strip completely oxidized to zirconia. The remaining portion of the strip in the background was still in one piece and contained a black zirconia layer in the middle. Magnification: 10x.

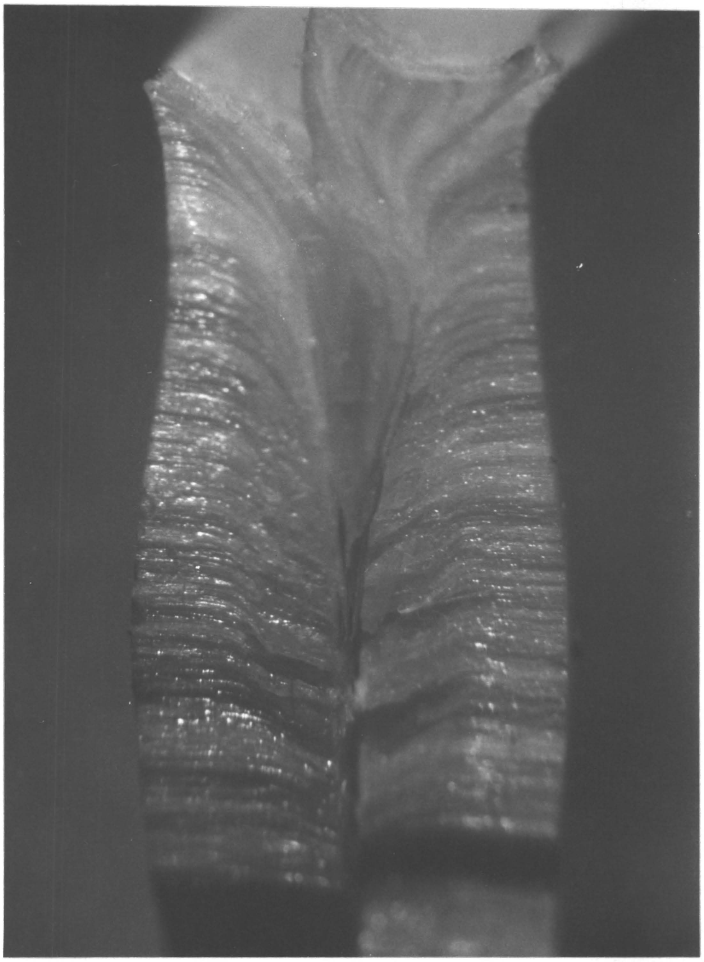

Figure 29

Completely oxidized specimen fractured along its axis. Note the curving of the white zirconia columnar grains near the end of the strip. Magnification: 20x.

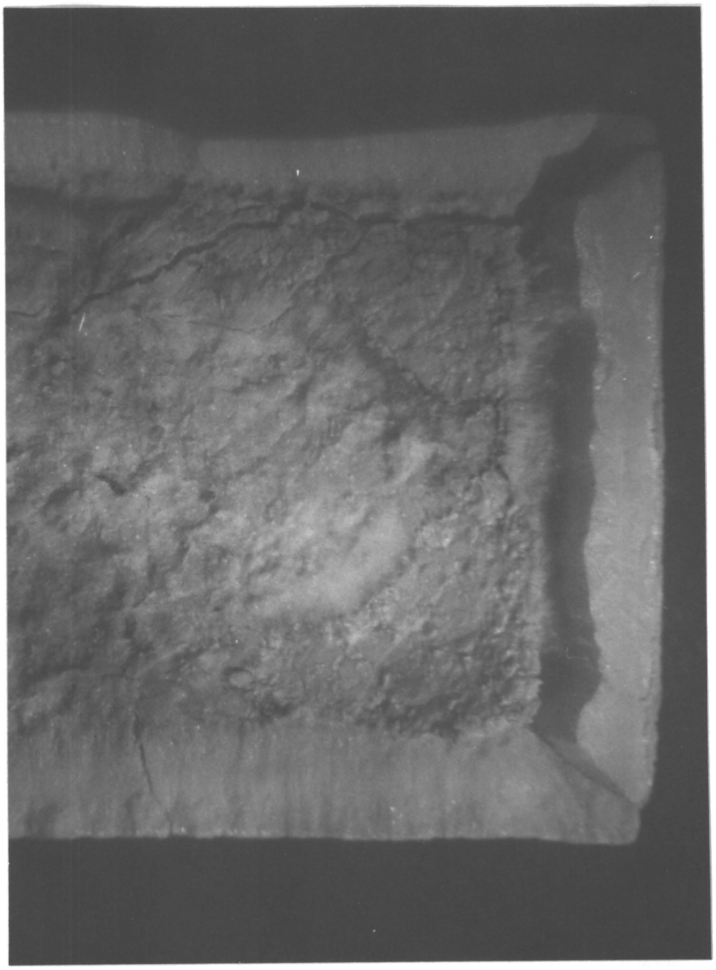

Figure 30

The centre plane (parallel to both surfaces) of a completely oxidized strip. Magnification: 7x.

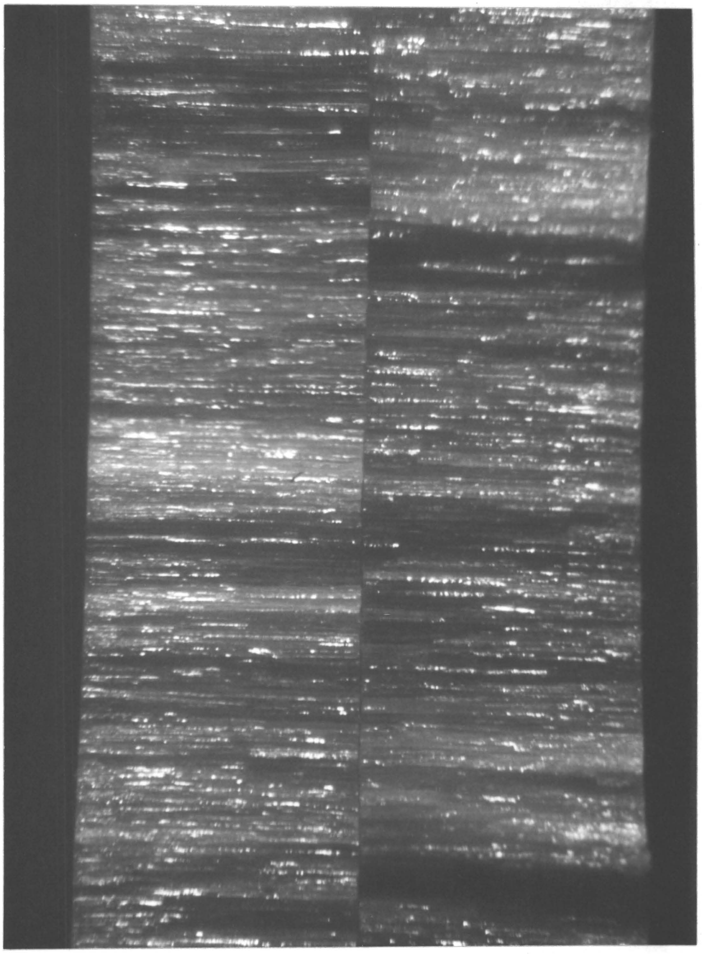

Figure 31

Longitudinal cross-section of a white zirconia strip fractured after completion of oxidation. Not etched. Magnification: 25x.

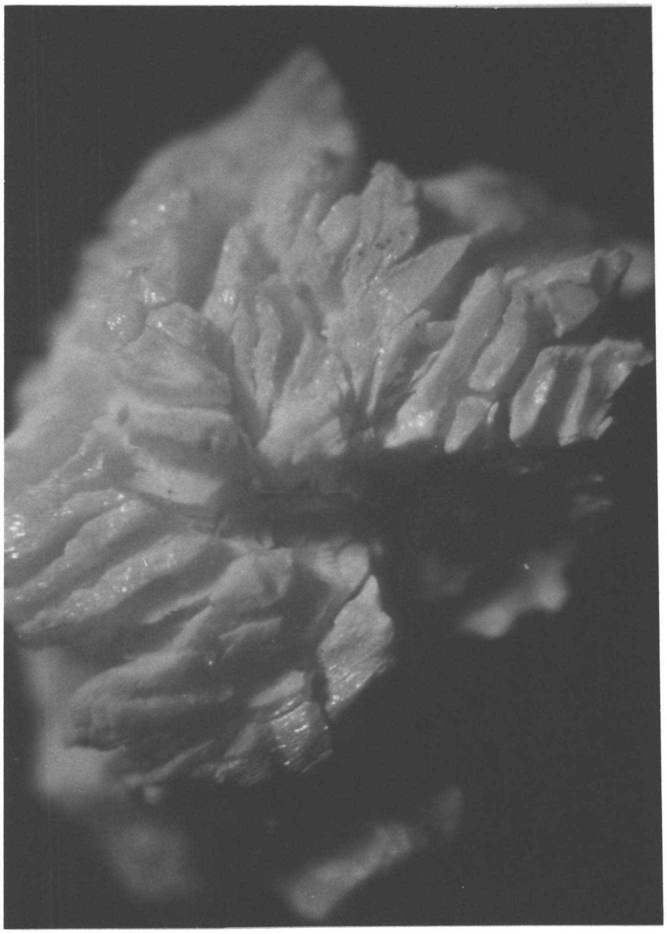

Figure 32

White zirconia obtained from a black zirconia particle stripped off its white layer and exposed directly to oxygen at 950°C. Magnification: 50x.

4.2 Spheroidization of Zirconia

Particles of crushed white zirconia which were used for spheroidizing are shown in Figures 33 and 34 . They passed through a Tyler sieve with openings of 0.075 mm and were collected on a sieve with openings of 0.045 mm. The particles shown in Figure 33 were obtained from zirconia produced at temperatures about 1000°C and below. Their structure was columnar, but showed a fair amount of cohesion in the planes normal to the direction of crystal growth. As a result, the crushed particles were rather equiaxed. Zirconia produced by oxidation of the metal at higher temperatures, in the tetragonal region, such as 1250°C, consisted of thin, needlelike columnar crystals, which readily separated while crushed in a mortar. The resulting material is shown in Figure 34 . Either type of particles spheroidized satisfactorily, and since the high temperature variety took less time to produce in the oxidation furnace, it was used for making most of the spheres for the diffusion experiments.

In the early spheroidizing experiments, the crushed zirconia particles were dropped through an arc operating in an air atmosphere, but the results were not satisfactory. Nitrogen from the air dissolved in molten zirconia, possibly forming zirconium nitride. As the molten spheres left the arc and cooled, nitrogen was released. At first, when zirconia was still molten, the gas could escape into the atmosphere, but as soon as a solid skin formed on the surface of the sphere, the pressure of nitrogen inside blew it up like a balloon to an enormous size, as shown in Figure 35 , making it entirely unsuitable for the intended use. Change

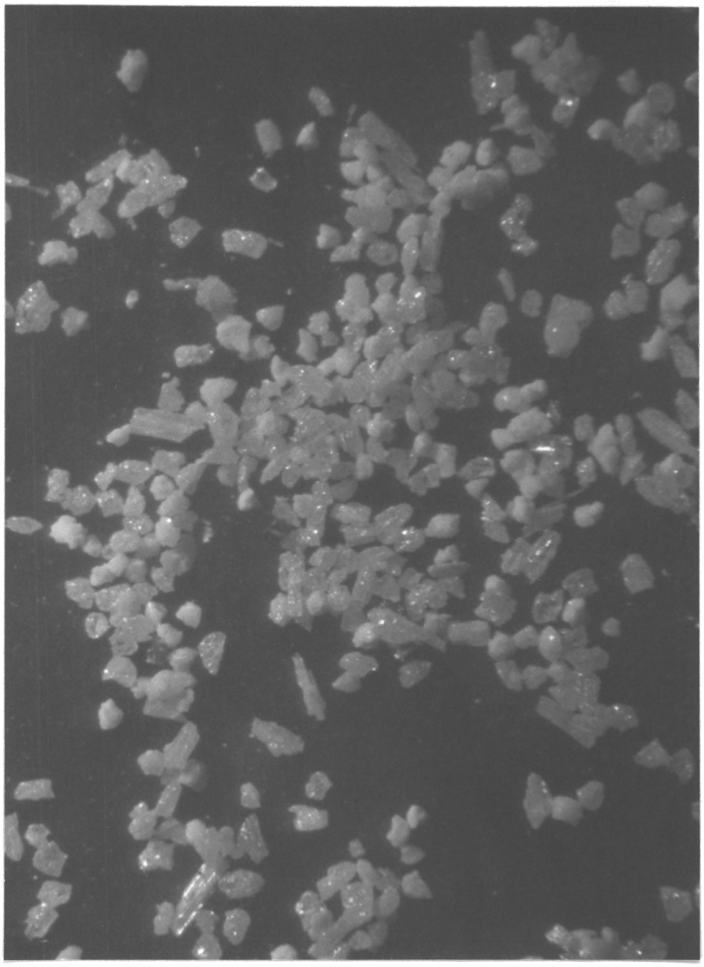

Figure 33

Particles of crushed white zirconia used for spheroidizing. This zirconia was produced from zirconium metal by oxidation at temperatures below 1000°C. Magnification: 75x.

Figure 34

Particles of crushed white zirconia used for spheroidizing. This material was produced from zirconium oxidized at 1250°C. Magnification: 35x.

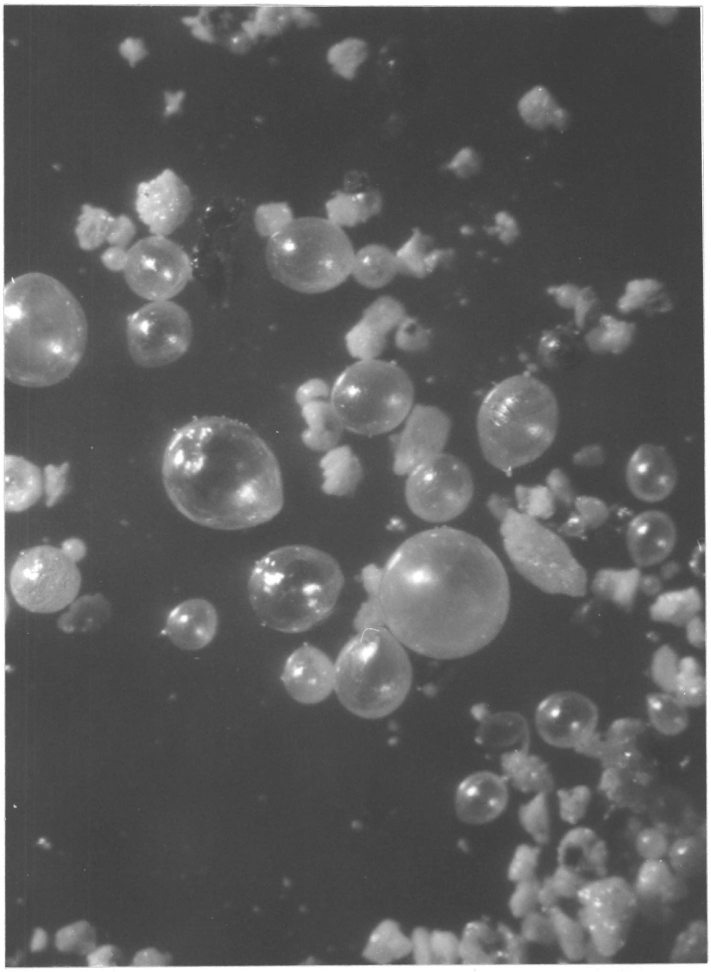

Figure 35

Unsatisfactory spheres produced in the arc operated in air.

Magnification: 100x.

of the arc atmosphere to an inert gas solved this problem by eliminating nitrogen, and also produced uncracked spheres, as discussed in Section 2.4. Argon was first used for this purpose, but it was soon found that helium produced a larger yield of better spheres, apparently because of its higher thermal conductivity.

The reducing atmosphere was supplied by carbon electrodes operating in helium. Carbon vapor produced in the temperature of the arc reacted with oxygen in $Zr\ O_2$ forming CO and sub-stoichiometric, black zirconia. This was probably a surface reaction only because of a short time available for carbon diffusion, but the product extended throughout the sphere as a result of vigorous mixing of the liquid zirconia produced by convection currents in high thermal gradients. In cooler areas outside the arc, carbon monoxide presumably changed to carbon dioxide and carbon which were removed by the flowing helium.

Results for the size distribution of the black zirconia spheres from a typical run involving one pass through the arc are presented in Table 3 , expressed as w/o of the white zirconia feed particles in the size range 45-75μ. The yield of 12.6 w/o includes only sound spheres and not incompletely fused particles or spheres fused together. Since a major percentage of the sample consisted of spheres with diameters larger than the largest dimension of the irregularly shaped feed particles, most spheres were produced by combined fusion of particles. In practice the yield was increased to approximately 50 w/o by recycling the feed through the arc five to six times. A sample of the black spheres obtained upon separation from the irregularly shaped feed is shown in Figure 36 . Only the spheres in the diameter ranges 45-75μ (average d = 60μ) and

Table 3

Size Distribution of Black Zirconia Spheres

Diameter range μ	Weight percent of all the black spheres	Weight percent of the white zirconia input
45-75	8	1.0
75-105	27	3.4
105-147	24	3.0
147-208	31	3.9
208	10	1.3
Total	100	12.6

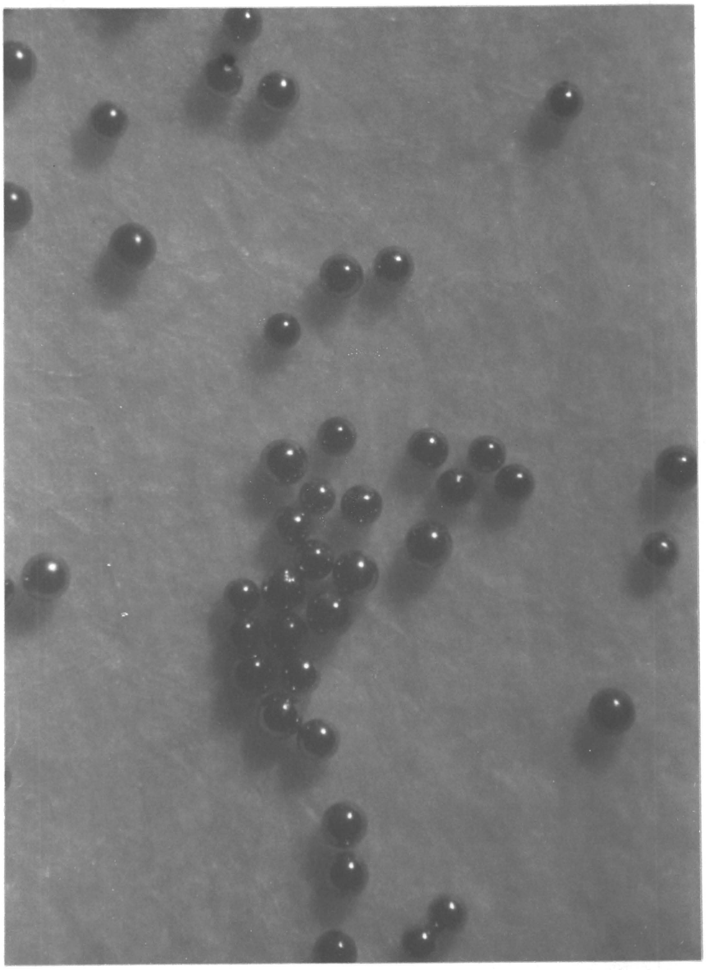

Figure 36

Black, sub-stoichiometric zirconia spheres. Magnification: 100x.

75-105μ (average d = 90μ) were used for oxygen diffusion experiments in this study, for two reasons. First of all, the spheres had to be small enough to allow for a reasonable proportion of oxygen exchange within the time allotted for the experiments. Secondly, large spheres had a much higher incidence rate of porosity and shrinkage cavities.

4.3 Metallographic and X-ray Diffraction Examination of Black Spheres

In order to microscopically examine the internal structure of theoxide, dispersions of spheres were mounted in bakelite and metallographically abraded using silicon carbide paper and diamond dust of progressively finer size, down to 0.3μ γ-alumina. The black spheres were found to possess various degrees of non-stoichiometry, depending apparently on the duration and place of the oxide particle passage through the arc. Representative samples of single-phase and two-phase black spheres are shown in Figures 37 through 40. Their structures will be discussed in Section 5.2 of this thesis.

X-ray diffraction photographs of the black spheres showed that the oxide was essentially monoclinic zirconia with no discernible zirconium carbide or other inclusions. Thirty-five degree oscillation and full rotation X-ray diffraction photographs were taken of one sphere using a Weissenberg camera with Cu K_α radiation. Examination of these patterns demonstrated that the sphere was polycrystalline, containing about five grains. Metallographic examination of some of the other spheres indicated that they were single crystals or contained less than five grains.

4.4 Re-oxidation of black spheres

The re-oxidation of the black spheres done at 850°C normally

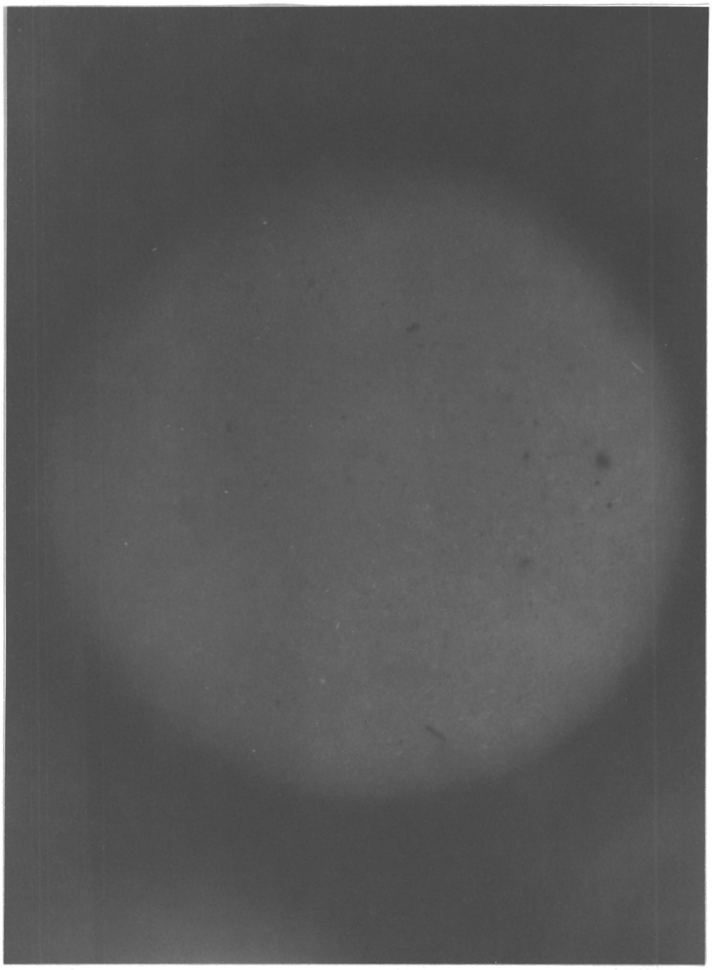

Figure 37

Cross-section of a black zirconia sphere consisting of a homogeneous, single phase. Not etched. Magnification: 500x.

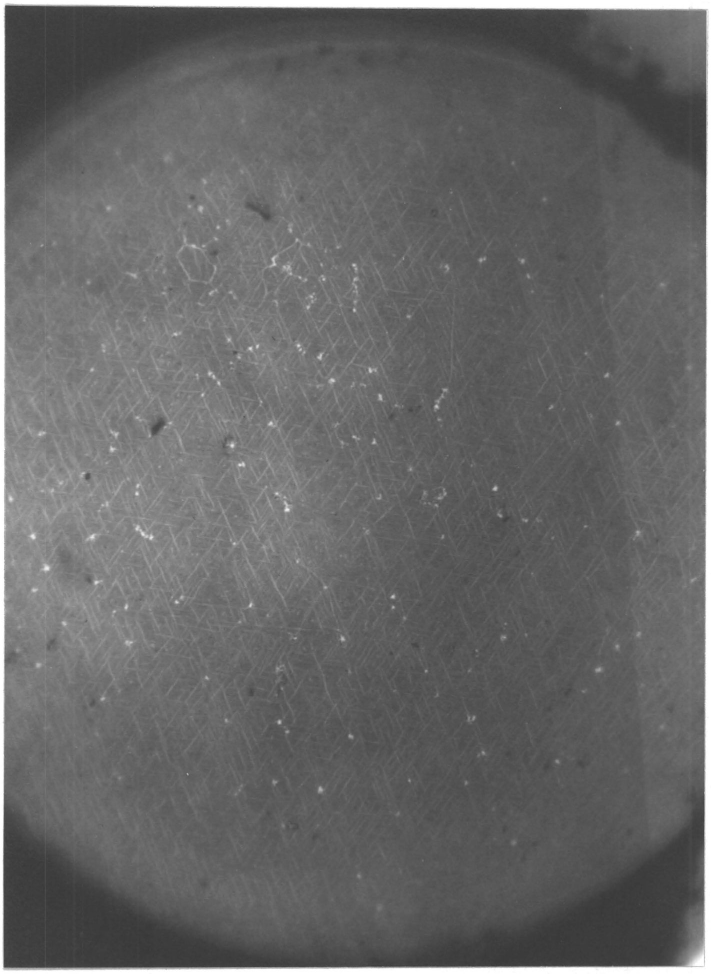

Figure 38

Cross-section of an almost single phase black zirconia sphere. The fine striations consist of the low-oxygen α-Zr solution phase rejected on cooling. Not etched. Magnification: 700x.

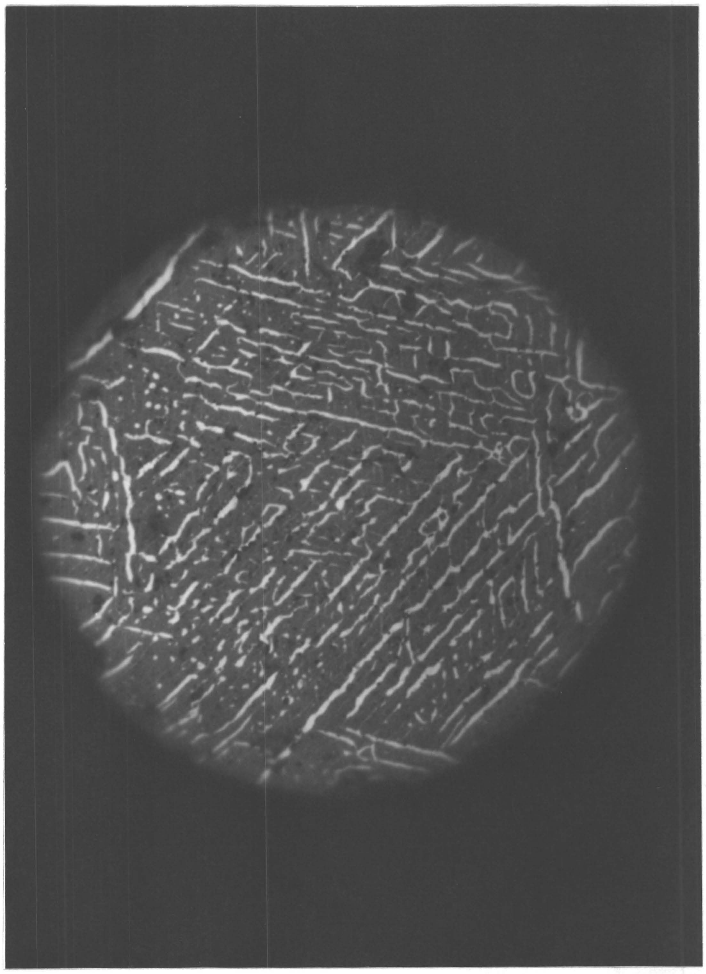

Figure 39

Cross-section of a black zirconia sphere showing large amounts of α-Zr precipitated on cooling. Not etched. Magnification: 700x.

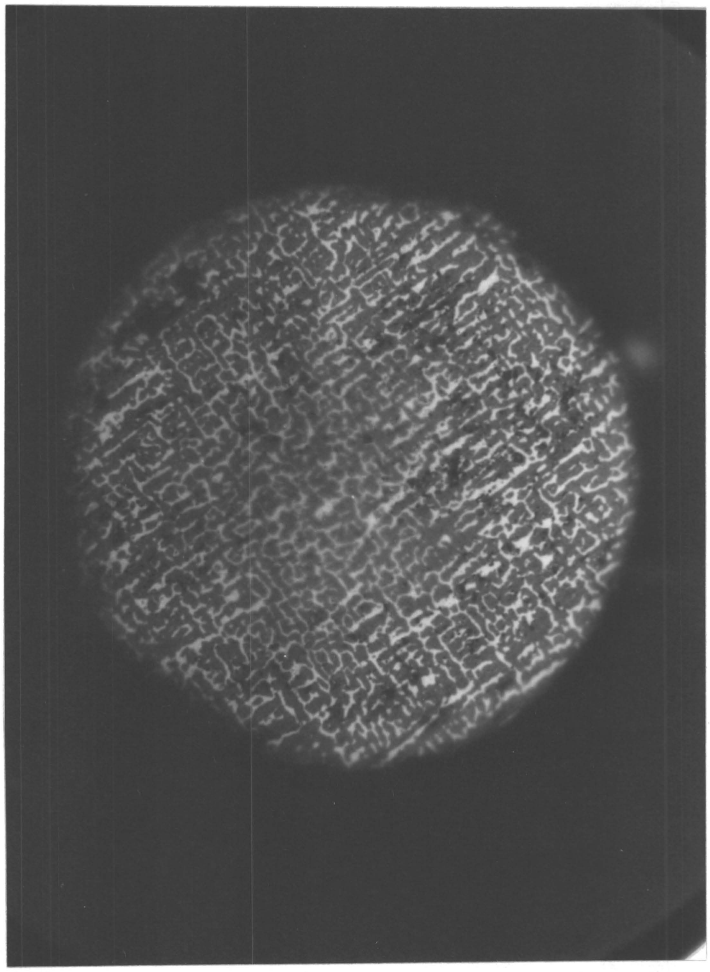

Figure 40

Cross-section of a black zirconia sphere with lower oxygen content showing some α-Zr solution phase rejected on cooling and some isothermal, eutectic α-Zr. Not etched. Magnification: 700x.

produced a yield of approximately 98% of compact, fully stoichiometric spheres. However, in the early stages of this investigation, the importance of the complete removal of nitrogen from the arc furnace was not fully appreciated. One lot of black spheres apparently had some nitrogen dissolved in the oxide, as indicated by traces of golden-yellow zirconium nitride on the surface of the spheres. These spheres were solid when removed from the arc furnace, but disintegrated on re-oxidation, as shown in Figure 41. When the bottom of the furnace was re-designed to made it air-tight, and the furnace was thoroughly purged with helium, good quality white spheres, such as shown in Figure 42 were consistently obtained on re-oxidation.

4.5 Metallographic Examination of White Spheres

A sample of white spheres was mounted in plastic and prepared for metallographic examination in the manner previously used for black spheres. The spheres were found to be sound and suitable for diffusion experiments. A photomicrograph of a typical sphere is shown in Figure 43.

4.6 Diffusion of Oxygen in Zirconia

The self-diffusion of oxygen in zirconia spheres was carried out as described in Section 3.3.1. The atomic concentration O^{18} in the isotopic water was 1.3%, which was also the molecular concentration because in every molecule of H_2O there is only one atom of oxygen. When the water was electrolyzed, the atomic concentration of O^{18} was obviously still 1.3%, but the concentration of the heavy molecules $O^{18}\,O^{16}$ was 2.6%, because the total number of oxygen molecules was then one half of the original number of atoms while the number of $O^{18}\,O^{16}$ was equal to the

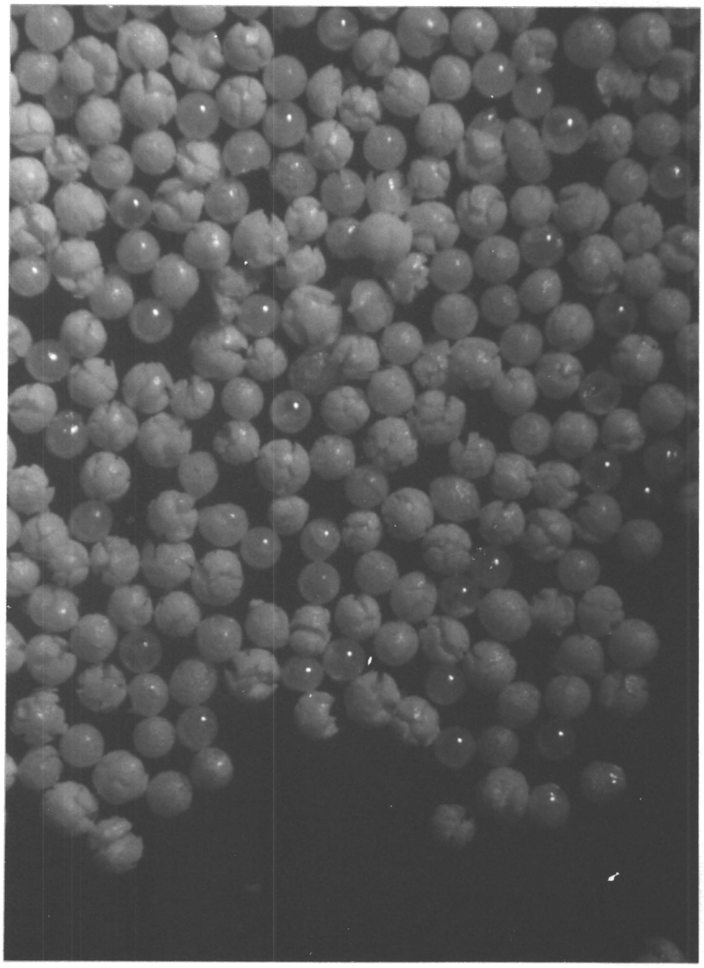

Figure 41

Nitrogen-contaminated spheres which disintegrated on reoxidation.

Magnification: 100x.

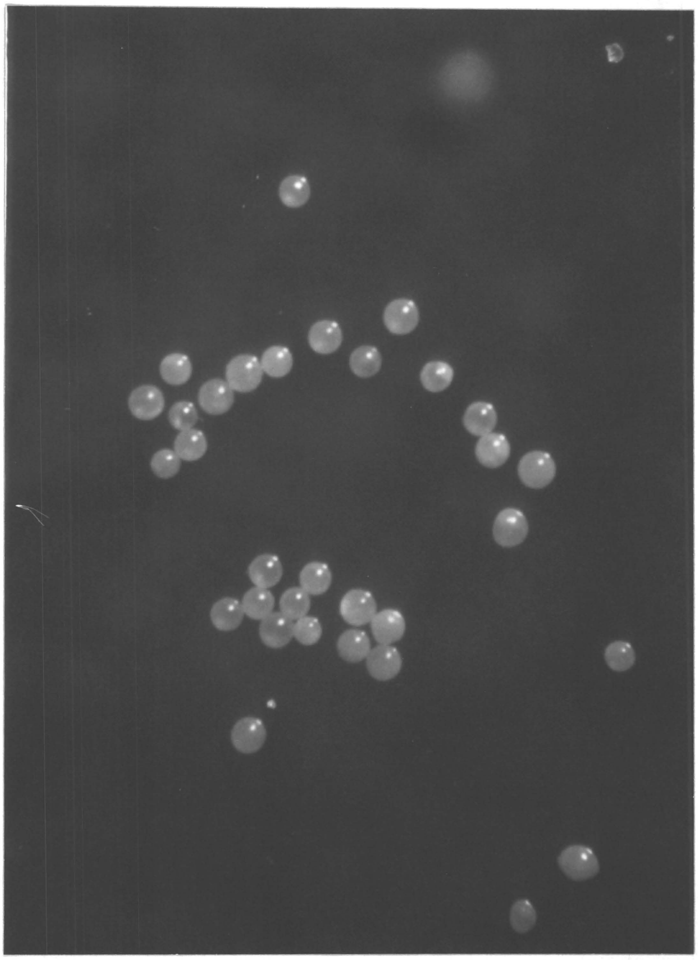

Figure 42

White, fully stoichiometric zirconia spheres. Magnification: 75x.

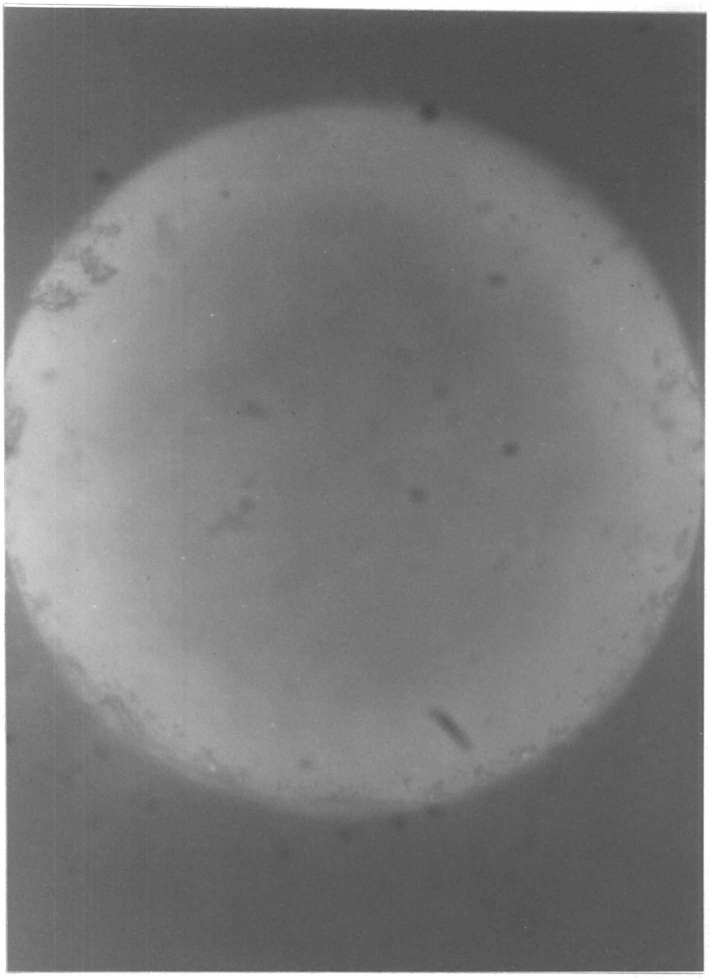

Figure 43

Cross-section of a white zirconia sphere. Not etched.

Magnification: 1500x.

original number of O^{18} atoms. Consequently, for every O^{18} atom entering the oxide, one O^{18} O^{16} molecule was destroyed, so that the change in concentration of the mass 34 molecules could be used as a measure of the progress of self-diffusion. In this analysis the presence of O^{18} O^{18} and O^{18} O^{17} was disregarded because of their negligible concentrations resulting from the very low probabilities of an O^{18} atom meeting another O^{18} atom or an O^{17} atom. This was substantiated by actual measurements of the concentrations of the mass 36 and 35 oxygen molecules, which were found to be below the accuracy range of the mass spectrometer. The O^{17}-O^{17} molecules, whose concentration was undoubtedly even lower, were actually included in the measured percentage of the mass 34 molecules.

Eleven samples of the oxygen atmosphere were taken during each run, - one before the oxide specimen was lowered into the hot furnace, and ten during the diffusive exchange. The time intervals between the sample collections were approximately equal, and therefore depended on the total duration of a run. This in turn was a function of temperature and of the desired final fraction of oxygen exchange. For the shortest run the gas sampling intervals were about 1.25 hr., for the longest run they were 1.25 day on the average.

The average total mass of the oxygen in the diffusion chamber during a run was calculated from the volume of the diffusion chamber and the oxygen pressure at room temperature before and after the run. The same mass of oxygen and the same mass of oxide spheres (0.5 gram) was used for every run so that the oxygen pressures at the diffusion temperatures were slightly different. However, the differences were too small to affect the mechanism or the rate of diffusion. The pressures during diffusion experiments were around one-half of the atmosphere. The exact values are shown in the Tables of results.

Besides the spheres, also some irregular but equiaxed zirconia particles were used for diffusion runs. These are shown in Figure 33, and were the same particles as used for spheroidization in the arc furnace. Finally, two zirconia "slabs", also cut to weigh as close as possible to 0.5 gram each, were employed as diffusion specimens. The "slabs", which are shown in Figures 44 through 47 were obtained by complete oxidation of zirconium strips using the method described in Sections 3.1.1 and 3.1.2. The slabs were simply the original "raw material" from which the irregular particles, and later the spheres were made.

The purpose of using the irregular particles and the "slabs" for the diffusion experiments was to provide material with the same chemical composition as the spheres, but with more defective structures, closer to that existing in the oxide scale on a metal substrate. Such structures were then tested under the same conditions as the compact spheres, yielding results which were directly comparable. One of the slabs was produced by zirconium oxidation at 950°C, in the temperature range for the monoclinic zirconia phase, while the other was obtained by oxidation at 1250°C, where zirconia is tetragonal. Both slabs had a columnar structure, but the lower temperature slab showed a much higher cohesion between the grains, so that it was difficult to trim it to the desired size without obtaining a brittle, irregular break. Conversely, the 1250°C slab was easily trimmed by cutting with a razor blade. Both slabs were microscopically examined before and after the diffusion runs

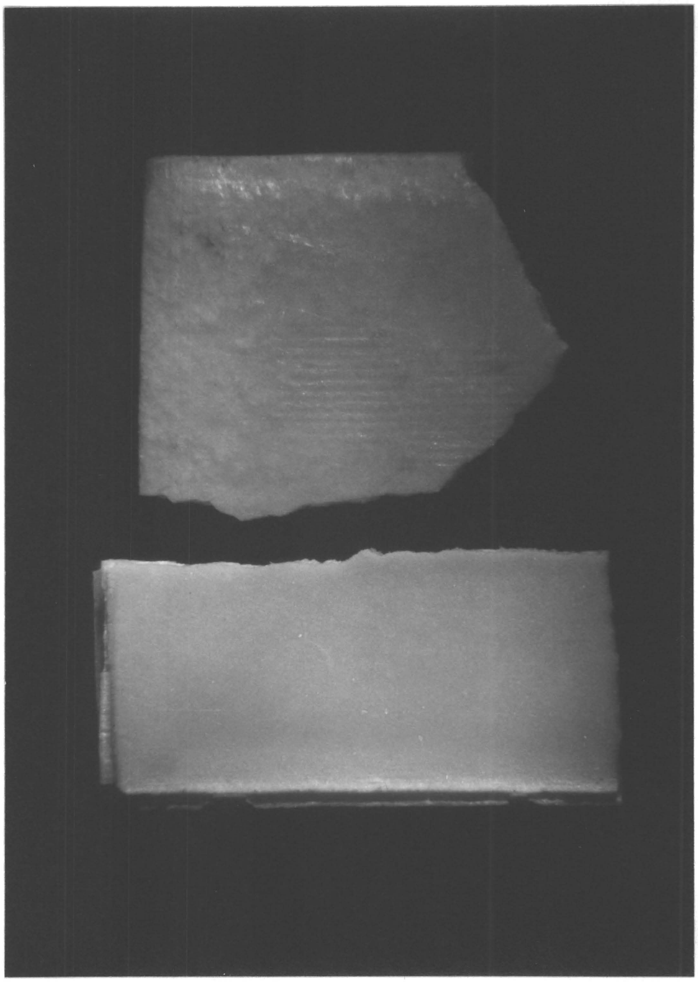

Figure 44

Top sides of zirconia "slabs" used for oxygen diffusion tests. Upper slab was obtained by zirconium oxidation at 950°C, lower slab - at 1250°C. Magnification: 5.5x.

Figure 45

Reverse sides of zirconia "slabs" used for oxygen diffusion tests. The surfaces visible were center planes of the zirconium metal strips befor oxidation. Upper slab was obtained by zirconium oxidation at 950°C, lower slab - at 1250°C. Magnification 5.5x.

Figure 46

Side view of the "950°C" slab from Figure 45. Average thickness: 1.28 mm. Magnification: 9x.

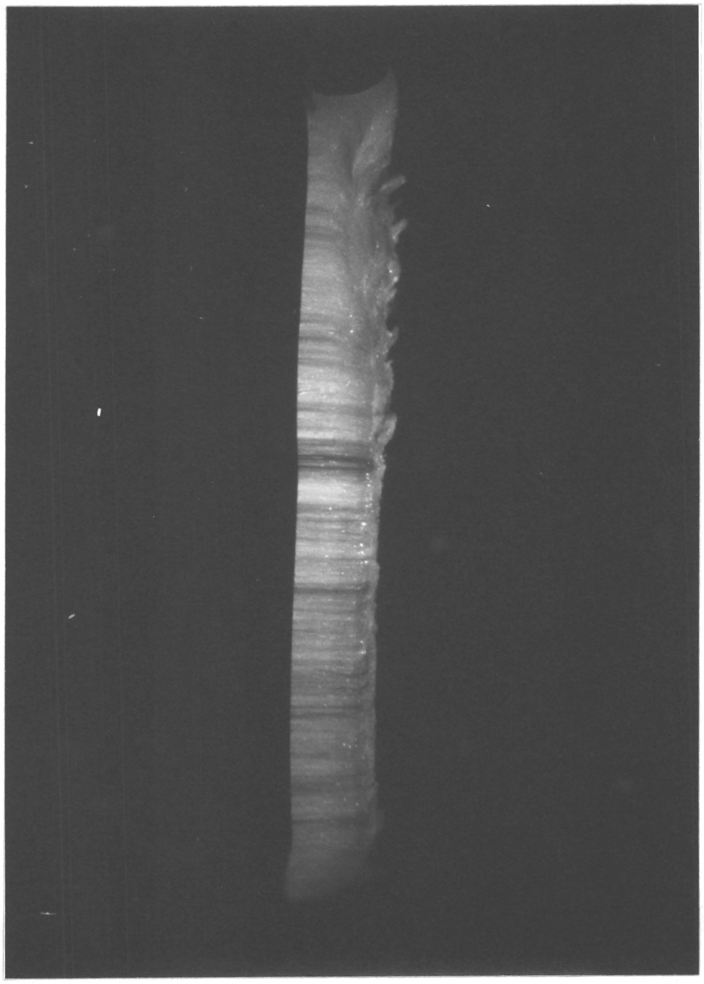

Figure 47

Side view of the "1250°C" slab from Figure 45. Average thickness: 1.44 mm. Magnification: 9x.

and no structural deterioration due to their heating and cooling could be detected, partly because the test temperature was below the allotropic transformation range.

Every specimen, whether made of spheres or a single slab, was gradually lowered into the hot furnace at the beginning of the diffusion run, so that it attained the hot zone temperature within 15 minutes. In view of the fact that the shortest run lasted 12.5 hours, this heat-up period had no significant effect on the oxygen diffusion results. The temperature of the specimen was continuously recorded throughout each run and was found to vary by no more than ±2°C. After the run was completed and the last gas sample taken, the specimen was cooled with the furnace.

The mathematical treatment of the mass spectrometer analyses followed that used by Hagel(93) for a similar investigation. The error function equation, originally developed by Carman and Haul(109), is $(p-p_1)/(p_2-p_1) = \phi\,\mathrm{erfc}\,(\sqrt{Dt}/a\lambda)$ where:

p = mole fraction of O^{18} in the convection stirred gas at time t.

p_1 = mole fraction of O^{18} initially in the oxide, taken as the natural abundance 0.0020.

p_2 = the original mole fraction of O^{18} in the gas at zero time, equal to 0.0130.

a = sphere radius divided by three, or slab thickness divided by two.

λ = ratio of total mass of oxygen in the gas (m_g) to the total mass of oxygen in the solid oxide (m_s).

In the calculation of m_s the oxide was assumed stoichiometric.

The above equation may be also expressed as

$$(p-p_1)/(p_2-p_1) = \exp\ (Dt/a^2\lambda^2)\ [1-\mathrm{erf}\ (\sqrt{Dt}/a\lambda)]$$

Figure 48 shows the graphical presentation of this equation, based on the numerical table given by Crank(110). This graph was used for the determination of $\sqrt{Dt}/a\lambda$ from the measured values of p. The self-diffusion coefficient D was then calculated from the measured t and known a and λ. The results are shown in Tables 4 through 12, and are summarized in Table 13.

The values of log D for the spheres at various absolute temperatures T were then plotted against $10^3/T$, as shown in Figure 49. They were found to fit fairly well a straight line in this Arrhenius plot, indicating that the frequency factor D_o is approximately constant in this temperature range. The "best fit" straight line was determined with the least square method using a computer. The equation obtained was

$$D = 8.58 \times 10^{-3}\ \exp\ (-56224/RT).\ \mathrm{cm^2/sec}$$

Standard error of estimate for log D was 0.067243.

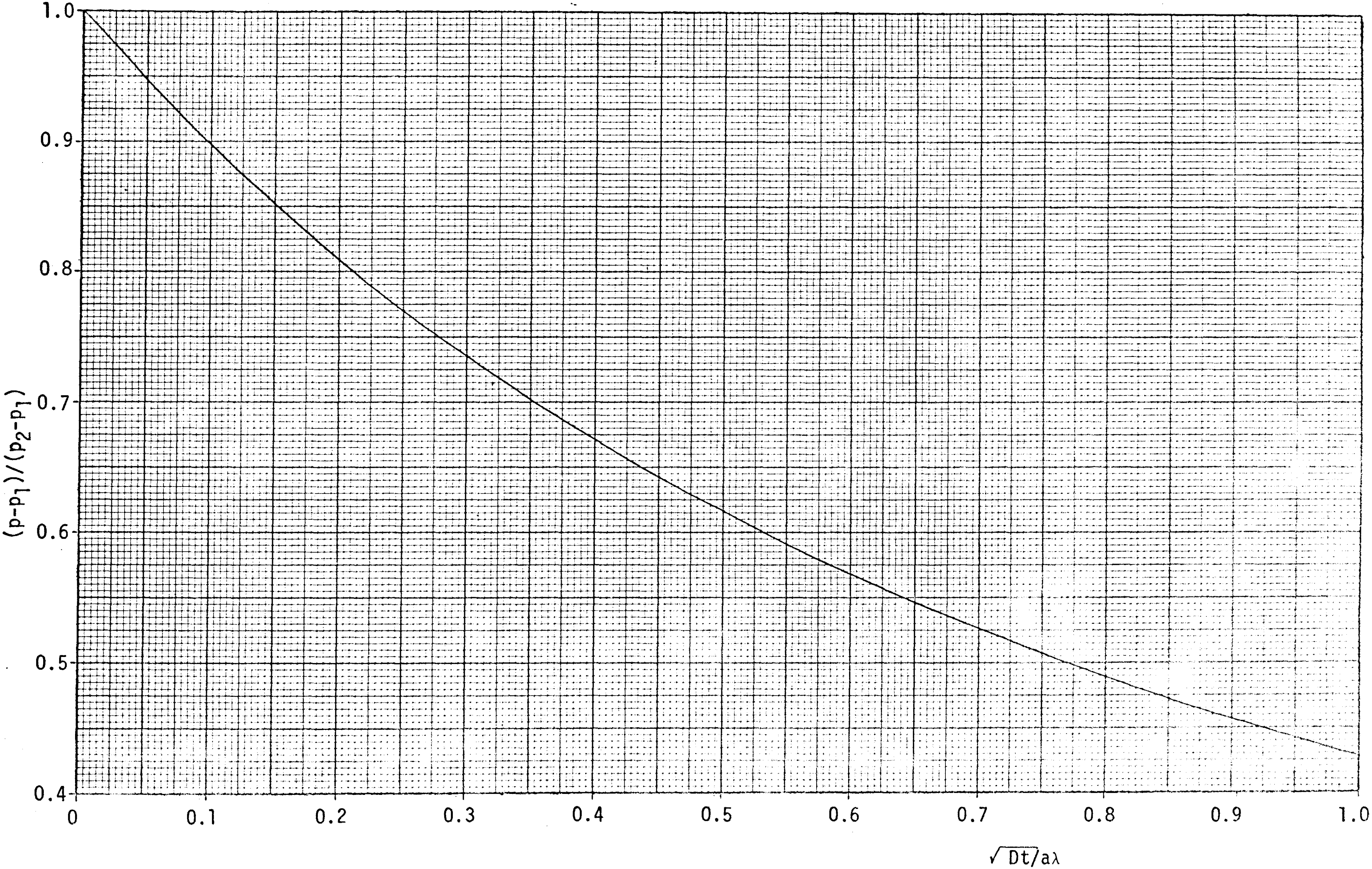

Figure 48

Plot of function $(p-p_1)/p_2-p_1 = \text{eerfc}\ (\sqrt{Dt}/a\lambda)$, used for calculating D.

TABLE 4

Oxygen Diffusion Results

Temperature: 1000°C.
Oxygen pressure: 370 mm Hg
Specimen: spheres, $d = 9.0 \times 10^{-3}$ cm.
Specimen weight: 0.500 g.
Run No. : 15-6

$$a = \frac{d}{6} = 1.5 \times 10^{-3} \text{ cm}$$

$$\lambda = \frac{m_g}{m_s} = \frac{9.3 \times 10^{-2}}{1.3 \times 10^{-1}} = 7.15 \times 10^{-1}$$

$$a^2\lambda^2 = 1.5 \times 10^{-6}$$

Sample No.	0	1	2	3	4
$p \times 10^3$	13.0	12.0	11.5	11.3	11.0
$(p-p_1)\times 10^3$	11.0	10.0	9.5	9.3	9.0
$\frac{p-p_1}{p_2-p_1}$	0.0	9.10×10^{-1}	8.64×10^{-1}	8.46×10^{-1}	8.19×10^{-1}
$\frac{Dt}{a\lambda}$	0.0	8.80×10^{-2}	1.35×10^{-1}	1.55×10^{-1}	1.88×10^{-1}
$\frac{Dt}{a^2\lambda^2}$	0.0	7.75×10^{-3}	1.83×10^{-2}	2.40×10^{-2}	3.54×10^{-2}
Dt	0.0	8.91×10^{-9}	2.10×10^{-8}	2.76×10^{-8}	4.07×10^{-8}
t hours	0.0	1.25	2.50	3.75	5.00
t sec.	0.0	4.50×10^3	9.00×10^3	1.35×10^4	1.80×10^4
D cm^2/sec.	-	1.98×10^{-12}	2.33×10^{-12}	2.04×10^{-12}	2.26×10^{-12}

Table continued . . .

TABLE 4 (continued)

Oxygen Diffusion Results

Temperature: 1000°C.
Oxygen pressure: 370 mm Hg
Specimen: spheres, $d = 9.0 \times 10^{-3}$ cm.
Specimen weight: 0.500 g.
Run No. : 15-6

$$a = \frac{d}{6} = 1.5 \times 10^{-3} \text{ cm}$$

$$\lambda = \frac{m_g}{m_s} = \frac{9.3 \times 10^{-2}}{1.3 \times 10^{-1}} = 7.15 \times 10^{-1}$$

$$a^2\lambda^2 = 1.15 \times 10^{-6}$$

Sample No.	5	6	7	8	9	10
$p \times 10^3$	10.9	10.8	10.6	10.5	10.4	10.3
$(p-p_1) \times 10^3$	8.9	8.8	8.6	8.5	8.4	8.3
$\frac{p - p_1}{p_2 - p_1}$	8.09×10^{-1}	8.00×10^{-1}	7.82×10^{-1}	7.73×10^{-1}	7.64×10^{-1}	7.55×10^{-1}
$\frac{Dt}{a\ \lambda}$	2.00×10^{-1}	2.10×10^{-1}	2.32×10^{-1}	2.47×10^{-1}	2.58×10^{-1}	2.70×10^{-1}
$\frac{Dt}{a^2\ \lambda^2}$	4.00×10^{-2}	4.41×10^{-2}	5.39×10^{-2}	6.10×10^{-2}	6.66×10^{-2}	7.30×10^{-2}
Dt	4.60×10^{-8}	5.07×10^{-8}	6.19×10^{-8}	7.01×10^{-8}	7.58×10^{-8}	8.39×10^{-8}
t hours	6.25	7.50	8.75	10.00	11.25	12.50
t sec.	2.25×10^4	2.70×10^4	3.15×10^4	3.60×10^4	4.05×10^4	4.50×10^4
D cm^2/sec.	2.04×10^{12}	1.88×10^{-12}	1.97×10^{-12}	1.95×10^{-12}	1.87×10^{-2}	1.86×10^{-12}

Average $D = 2 \times 10^{-12}$ cm^2/sec.

TABLE 5

Oxygen Diffusion Results

Temperature: 950°C.
Oxygen pressure: 365 mm Hg
Specimen: spheres, d = 9.0×10^{-3} cm.
Specimen weight: 0.500 g.
Run No. 9-6

$$a = \frac{d}{6} = 1.5 \times 10^{-3} \text{ cm.}$$

$$\lambda = \frac{m_g}{m_s} = \frac{9.3 \times 10^{-2}}{1.3 \times 10^{-1}} = 7.15 \times 10^{-1}$$

$$a^2\lambda^2 = 1.15 \times 10^{-6}$$

Sample No.	0	1	2	3	4
$p \times 10^3$	13	12	11.5	11	10.5
$(p-p_1) \times 10^3$	11	10	9.5	9	8.5
$\frac{p - p_1}{p_2 - p_1}$	1.0	9.09×10^{-1}	8.64×10^{-1}	8.18×10^{-1}	7.73×10^{-1}
$\frac{Dt}{a\lambda}$	0	8.70×10^{-2}	1.36×10^{-1}	1.89×10^{-1}	2.45×10^{-1}
$\frac{Dt}{a^2\lambda^2}$	0	7.57×10^{-3}	1.85×10^{-2}	3.57×10^{-2}	6.00×10^{-2}
Dt	0	8.72×10^{-9}	2.13×10^{-8}	4.11×10^{-8}	6.91×10^{-8}
t hours	0	5.5	11.0	16.5	22.0
t sec.	0	1.98×10^4	3.96×10^4	5.94×10^4	7.92×10^4
D cm^2/sec.	-	4.41×10^{-13}	5.48×10^{-13}	6.92×10^{-13}	8.72×10^{-13}

Table continued . . .

TABLE 5 (continued)

Oxygen Diffusion Results

Temperature: 950°C.
Oxygen pressure: 365 mm Hg
Specimen: spheres, d = 9.0×10^{-3} cm.
Specimen weight: 0.500 g.
Run No. 9-6

$$a = \frac{d}{6} = 1.5 \times 10^{-3} \text{ cm}$$

$$\lambda = \frac{m_g}{m_s} = \frac{9.3 \times 10^{-2}}{1.3 \times 10^{-1}} = 7.5 \times 10^{-1}$$

$$a^2\lambda^2 = 1.15 \times 10^{-6}$$

Sample No.	5	6	7	8	9	10
$p \times 10^3$	10.5	10	10	10	9.5	9.5
$(p-p_1) \times 10^3$	8.5	8	8	8	7.5	7.5
$\frac{p-p_1}{p_2 - p_1}$	7.73×10^{-1}	7.27×10^{-1}	7.27×10^{-1}	7.27×10^{-1}	6.82×10^{-1}	6.82×10^{-1}
$\frac{Dt}{a\lambda}$	2.45×10^{-1}	3.13×10^{-1}	3.13×10^{-1}	3.13×10^{-1}	3.83×10^{-1}	3.83×10^{-1}
$\frac{Dt}{a^2\lambda^2}$	6.00×10^{-2}	9.80×10^{-2}	9.80×10^{-2}	9.80×10^{-2}	1.47×10^{-1}	1.47×10^{-1}
Dt	6.91×10^{-8}	1.13×10^{-7}	1.13×10^{-7}	1.13×10^{-7}	1.69×10^{-7}	1.69×10^{-7}
t hours	27.5	34.25	45.0	54.5	58.5	70.0
t sec.	9.90×10^{4}	1.23×10^{5}	1.62×10^{5}	1.96×10^{5}	2.11×10^{5}	2.52×10^{5}
D cm^2/sec.	6.98×10^{-13}	9.18×10^{-13}	6.97×10^{-13}	5.76×10^{-13}	8.01×10^{-13}	6.72×10^{-13}

Average D = 7×10^{-13} cm^2/sec.

TABLE 6

Oxygen Diffusion Results

Temperature: 900°C.
Oxygen pressure: 361 mm Hg.
Specimen: spheres, $d = 9.0 \times 10^{-3}$ cm
Specimen weight: 0.500 g.
Run No. 27-5

$$a = \frac{d}{6} = 1.5 \times 10^{-3} \text{ cm.}$$

$$\lambda = \frac{m_g}{m_s} = \frac{9.3 \times 10^{-2}}{1.3 \times 10^{-1}} = 7.15 \times 10^{-1}$$

$$a^2\lambda^2 = 1.15 \times 10^{-6}$$

Sample No.	0	1	2	3	4
$p \times 10^3$	13	12.5	12	11.5	11
$(p-p_1) \times 10^3$	11	10.5	10	9.5	9
$\frac{p - p_1}{p_2 - p_1}$	1.0	9.55×10^{-1}	9.09×10^{-1}	8.64×10^{-1}	8.18×10^{-1}
$\frac{Dt}{a \lambda}$	0	4.25×10^{-2}	8.70×10^{-2}	1.36×10^{-1}	1.89×10^{-1}
$\frac{Dt}{a^2\lambda^2}$	0	1.81×10^{-3}	7.57×10^{-3}	1.85×10^{-2}	3.57×10^{-2}
Dt	0	2.08×10^{-9}	8.72×10^{-9}	2.13×10^{-8}	4.11×10^{-8}
t hours	0	3.5	18.0	27.25	39.5
t sec.	0	1.26×10^{4}	6.48×10^{4}	9.80×10^{4}	1.42×10^{5}
C cm^2/sec	-	1.65×10^{-13}	2.17×10^{-13}	2.17×10^{-13}	2.89×10^{-13}

Table continued . . .

TABLE 6 continued

Oxygen Diffusion Results

Temperature: 900°C.
Oxygen pressure: 361 mm Hg
Specimen: spheres, $d = 9.0 \times 10^{-3}$ cm.
Specimen weight: 0.500 g.
Run No. 27-5

$a = \frac{d}{6} = 1.5 \times 10^{-3}$ cm

$\lambda = \frac{m_g}{m_s} = \frac{9.3 \times 10^{-2}}{1.3 \times 10^{-1}} = 7.15 \times 10^{-1}$

$a^2\lambda^2 = 1.15 \times 10^{-6}$

Sample No.	5	6	7	8	9	10
$p \times 10^3$	11	10.5	10.5	10	10	10
$(p-p_1) \times 10^3$	9	8.5	8.5	8	8	8
$\frac{p-p_1}{p_2 - p_1}$	8.18×10^{-1}	7.73×10^{-1}	7.73×10^{-1}	7.27×10^{-1}	7.27×10^{-1}	7.27×10^{-1}
$\frac{Dt}{a\ \lambda}$	1.89×10^{-1}	2.45×10^{-1}	2.45×10^{-1}	3.13×10^{-1}	3.13×10^{-1}	3.13×10^{-1}
$\frac{Dt}{a^2\ \lambda^2}$	3.57×10^{-2}	6.00×10^{-2}	6.00×10^{-2}	9.80×10^{-2}	9.80×10^{-2}	9.80×10^{-2}
Dt	4.11×10^{-8}	6.91×10^{-8}	6.91×10^{-8}	1.13×10^{-7}	1.13×10^{-7}	1.13×10^{-7}
t hours	52.25	63.5	75.0	87.5	99.75	111.5
t sec.	1.88×10^5	2.29×10^5	2.70×10^5	3.15×10^5	3.59×10^5	4.02×10^5
D cm^2/sec.	2.19×10^{-13}	3.02×10^{-13}	2.56×10^{-13}	3.59×10^{-13}	3.15×10^{13}	2.81×10^{-13}

TABLE 7

Oxygen Diffusion Results

Temperature: 850°C.
Oxygen pressure: 356 mm Hg.
Specimen: spheres, $d = 9.0 \times 10^{-3}$ cm.
Specimen weight: 0.500 g.
Run No.: 15-5

$$a = \frac{d}{6} = 1.5 \times 10^{-3} \text{ cm.}$$

$$\lambda = \frac{m_g}{m_s} = \frac{9.3 \times 10^{-2}}{1.3 \times 10^{-1}} = 7.15 \times 10^{-1}$$

$$a^2\lambda^2 = 1.15 \times 10^{-6}$$

Sample No.	0	1	2	3	4
$p \times 10^3$	13	12.5	12.5	12.5	12
$(p-p_1) \times 10^3$	11	10.5	10.5	10.5	10
$\frac{p - p_1}{p_2 - p_1}$	0	9.55×10^{-1}	9.55×10^{-1}	9.55×10^{-1}	9.09×10^{-1}
$\frac{Dt}{a\lambda}$	0	4.25×10^{-2}	4.25×10^{-2}	4.25×10^{-2}	8.70×10^{-2}
$\frac{Dt}{a^2\lambda^2}$	0	1.81×10^{-3}	1.81×10^{-3}	1.81×10^{-3}	7.57×10^{-3}
Dt	0	2.08×10^{-9}	2.08×10^{-9}	2.08×10^{-9}	8.70×10^{-9}
t hours	0	3.5	5.5	9.5	21.0
t sec.	0	1.26×10^4	1.98×10^4	3.42×10^4	7.56×10^4
D cm^2/sec.	-	1.65×10^{-13}	1.05×10^{-13}	6.08×10^{-14}	1.15×10^{-13}

Table continued . . .

TABLE 7 continued

Oxygen Diffusion Results

Temperature: 850°C.
Oxygen pressure: 356 mm Hg.
Specimen: spheres, $d = 9.0 \times 10^{-3}$ cm
Specimen weight: 0.500 g.
Run No.: 15-5

$$a = \frac{d}{6} = 1.5 \times 10^{-3} \text{ cm}$$

$$\lambda = \frac{m_g}{m_s} = \frac{9.3 \times 10^{-2}}{1.3 \times 10^{-1}} = 7.15 \times 10^{-1}$$

$$a^2\lambda^2 = 1.15 \times 10^{-6}$$

Sample No.	5	6	7	8	9	10
$p \times 10^3$	12	12	11.5	11.5	11.5	11.5
$(p-p_1) \times 10^3$	10	10	9.5	9.5	9.5	9.5
$\frac{p - p_1}{p_2 - p_1}$	9.09×10^{-1}	9.09×10^{-1}	8.64×10^{-1}	8.64×10^{-1}	8.64×10^{-1}	8.64×10^{-1}
$\frac{Dt}{a\lambda}$	8.70×10^{-2}	8.70×10^{-2}	1.36×10^{-1}	1.36×10^{-1}	1.36×10^{-1}	1.36×10^{-1}
$\frac{Dt}{a^2\lambda^2}$	7.57×10^{-3}	7.57×10^{-3}	1.85×10^{-2}	1.85×10^{-2}	1.85×10^{-2}	1.85×10^{-2}
Dt	8.70×10^{-9}	8.70×10^{-9}	2.13×10^{-8}	2.13×10^{-8}	2.13×10^{-8}	2.13×10^{-8}
t hours	24.0	29.0	40.0	43.5	46.0	50.0
t sec.	8.64×10^{4}	1.05×10^{5}	1.44×10^{5}	1.57×10^{5}	1.66×10^{5}	1.80×10^{5}
D cm^2/sec.	1.01×10^{-13}	8.29×10^{-14}	1.48×10^{-13}	1.36×10^{-13}	1.28×10^{-13}	1.18×10^{-13}

Average $D = 1 \times 10^{-13}$ cm^2/sec.

TABLE 8

Oxygen Diffusion Results

Temperature: 850°C.
Oxygen pressure: 335 mm Hg.
Specimen: spheres, $d = 9.0 \times 10^{-3}$ cm.
Specimen weight: 0.500 g.
Run No.: 21-5

$$a = \frac{d}{6} = 1.5 \times 10^{-3} \text{ cm}$$

$$\lambda = \frac{m_g}{m_s} = \frac{8.2 \times 10^{-2}}{1.3 \times 10^{-1}} = 6.31 \times 10^{-1}$$

$$a^2\lambda^2 = 8.96 \times 10^{-7}$$

Sample No.	0	1	2	3	4
$p \times 10^3$	13	12.5	12	11.5	11.5
$(p-p_1) \times 10^3$	11	10.5	10	9.5	9.5
$\frac{p-p_1}{p_2-p_1}$	1.0	9.55×10^{-1}	9.09×10^{-1}	8.64×10^{-1}	8.64×10^{-1}
$\frac{Dt}{a\lambda}$	0	4.25×10^{-2}	8.70×10^{-2}	1.36×10^{-1}	1.36×10^{-1}
$\frac{Dt}{a^2\lambda^2}$	0	1.81×10^{-3}	7.57×10^{-3}	1.85×10^{-2}	1.85×10^{-2}
Dt	0	1.62×10^{-9}	6.78×10^{-9}	1.66×10^{-8}	1.66×10^{-8}
t hours	0	14.0	18.0	36.0	47.0
t sec.	0	5.04×10^4	6.48×10^4	1.30×10^5	1.69×10^5
D cm^2/sec	-	3.21×10^{-14}	1.05×10^{-13}	1.28×10^{-13}	9.82×10^{-14}

continued . . . .

TABLE 8 continued

Oxygen Diffusion Results

Temperature: 850°C.

Oxygen pressure: 335 mm Hg.

Specimen: spheres, $d = 9.0 \times 10^{-3}$ cm.

Specimen weight: 0.500 g.

Run No.: 21-5

$$a = \frac{d}{6} = 1.5 \times 10^{-3} \text{ cm}$$

$$\lambda = \frac{m_g}{m_s} = \frac{8.2 \times 10^{-2}}{1.3 \times 10^{-1}} = 6.31 \times 10^{-1}$$

$$a^2\lambda^2 = 8.96 \times 10^{-7}$$

Sample No.	5	6	7	8	9	10
$p \times 10^3$	11	11	11	10.5	10.5	10.5
$(p-p_1) \times 10^3$	9	9	9	8.5	8.5	8.5
$\frac{p-p_1}{p_2-p_1}$	8.18×10^{-1}	8.18×10^{-1}	8.18×10^{-1}	7.73×10^{-1}	7.73×10^{-1}	7.73×10^{-1}
$\frac{Dt}{a\lambda}$	1.89×10^{-1}	1.89×10^{-1}	1.89×10^{-1}	2.45×10^{-1}	2.45×10^{-1}	2.45×10^{-1}
$\frac{Dt}{a^2\lambda^2}$	3.57×10^{-2}	3.57×10^{-2}	3.57×10^{-2}	6.00×10^{-2}	6.00×10^{-2}	6.00×10^{-2}
Dt	3.20×10^{-8}	3.20×10^{-8}	3.20×10^{-8}	5.38×10^{-8}	5.38×10^{-8}	5.38×10^{-8}
t hours	61.0	70.5	82.5	89.0	93.5	108.0
t sec.	2.20×10^5	2.54×10^5	2.97×10^5	3.20×10^5	3.27×10^5	3.89×10^5
D cm^2/sec.	1.45×10^{-13}	1.26×10^{-13}	1.08×10^{-13}	1.68×10^{-13}	1.60×10^{-13}	1.38×10^{-13}

Average $D = 1 \times 10^{-13}$ cm^2/sec.

TABLE 9

Oxygen Diffusion Results

Temperature: 800°C.

Oxygen pressure: 352 mm Hg.

Specimen: spheres, $d = 6.0 \times 10^{-3}$ cm.

Specimen weight: 0.500 g.

Run No. 2-6

$$a = \frac{d}{6} = 1.0 \times 10^{-3} \text{ cm}$$

$$\lambda = \frac{m_g}{m_s} = \frac{9.3 \times 10^{-2}}{1.3 \times 10^{-1}} = 7.15 \times 10^{-1}$$

$$a^2\lambda^2 = 5.11 \times 10^{-7}$$

Sample No.	0	1	2	3	4
$p \times 10^3$	13	12.5	12	12	11.5
$(p - p_1) \times 10^3$	11	10.5	10	10	9.5
$\frac{p - p_1}{p_2 - p_1}$	1.0	9.55×10^{-1}	9.09×10^{-1}	9.09×10^{-1}	8.64×10^{-1}
$\frac{Dt}{a\lambda}$	0	4.25×10^{-2}	8.70×10^{-2}	8.70×10^{-2}	1.36×10^{-1}
$\frac{Dt}{a^2\lambda^2}$	0	1.81×10^{-3}	7.57×10^{-3}	7.57×10^{-3}	1.85×10^{-2}
Dt	0	9.25×10^{-10}	3.87×10^{-9}	3.87×10^{-9}	9.45×10^{-9}
t hours	0	22.75	45.0	56.5	73.75
t sec.	0	8.20×10^4	1.62×10^5	2.04×10^5	2.66×10^5
D cm^2/sec	-	1.13×10^{-14}	2.39×10^{-14}	1.90×10^{-14}	3.55×10^{-14}

Table continued . . .

TABLE 9 continued

Oxygen Diffusion Results

Temperature: 800°C.
Oxygen pressure: 352 mm Hg.
Specimen: spheres, $d = 6.0 \times 10^{-3}$ cm.
Specimen weight: 0.500 g.
Run No. 2-6

$$a = \frac{d}{6} = 1.0 \times 10^{-3} \text{ cm}$$

$$\lambda = \frac{m_g}{m_s} = \frac{9.3 \times 10^{-2}}{1.3 \times 10^{-1}} = 7.15 \times 10^{-1}$$

$$a^2\lambda^2 = 5.11 \times 10^{-7}$$

Sample No.	5	6	7	8	9	10
$p \times 10^3$	11.5	11.5	11.5	11.5	11	11
$(p-p_1) \times 10^3$	9.5	9.5	9.5	9.5	9	9
$\frac{p-p_1}{p_2-p_1}$	8.64×10^{-1}	8.64×10^{-1}	8.64×10^{-1}	8.64×10^{-1}	8.18×10^{-1}	8.18×10^{-1}
$\frac{Dt}{a\lambda}$	1.36×10^{-1}	1.36×10^{-1}	1.36×10^{-1}	1.36×10^{-1}	1.89×10^{-1}	1.89×10^{-1}
$\frac{Dt}{a^2\lambda^2}$	1.85×10^{-2}	1.85×10^{-2}	1.85×10^{-2}	1.85×10^{-2}	3.57×10^{-2}	3.57×10^{-2}
Dt	9.45×10^{-9}	9.45×10^{-9}	9.45×10^{-9}	9.45×10^{-9}	1.83×10^{-8}	1.83×10^{-8}
t hours	78.25	90.75	100.0	116.5	124.5	141.0
t sec.	2.82×10^5	3.27×10^5	3.60×10^5	4.20×10^5	4.48×10^5	5.08×10^5
D cm²/sec.	3.35×10^{-14}	2.89×10^{-14}	2.63×10^{-14}	2.25×10^{-14}	4.08×10^{-14}	3.60×10^{-14}

Average $D = 3 \times 10^{-14}$ cm²/sec.

TABLE 10

Oxygen Diffusion Results

Temperature: 850°C.

Oxygen pressure: 375 mm Hg.

Specimen: irregular particles, equiaxed, $d \simeq 6.0 \times 10^{-3}$ cm.

Specimen weight: 0.500 g.

Run No. : 9-5

$$a = \frac{d}{6} = 1.0 \times 10^{-3} \text{ cm}$$

$$\lambda = \frac{m_g}{m_s} = \frac{9.6 \times 10^{-2}}{1.3 \times 10^{-1}} = 7.38 \times 10^{-1}$$

$$a^2\lambda^2 = 5.45 \times 10^{-7}$$

Sample No.	0	1	2	3	4
$p \times 10^3$	13	11.5	10.5	10	9
$(p - p_1) \times 10^3$	11	9.5	8.5	8	7
$\frac{p - p_1}{p_2 - p_1}$	1.0	8.64×10^{-1}	7.73×10^{-1}	7.27×10^{-1}	6.36×10^{-1}
$\frac{Dt}{a \lambda}$	0	1.36×10^{-1}	2.45×10^{-1}	3.13×10^{-1}	4.60×10^{-1}
$\frac{Dt}{a^2\lambda^2}$	0	1.85×10^{-2}	6.00×10^{-2}	9.80×10^{-2}	2.12×10^{-1}
Dt	0	1.01×10^{-8}	3.27×10^{-8}	5.34×10^{-8}	1.16×10^{-7}
t hours	0	0.67	1.67	2.67	15.84
t sec.	0	2.4×10^3	6.0×10^3	9.6×10^3	5.7×10^4
D cm^2/sec.	-	4.20×10^{-12}	5.45×10^{-12}	5.56×10^{-12}	2.04×10^{-12}

Average $D = 4 \times 10^{-12}$ cm^2/sec.

TABLE 11

Oxygen Diffusion Results

Temperature: 950°C.

Oxygen pressure: 365 mm Hg

Specimen: "Slab:, 1.28 mm thick
produced at 950°C.

Specimen weight: 0.534 g.

Run No.: 17-6

$$a = \frac{L}{2} = 6.4 \times 10^{-2} \text{ cm}$$

$$\lambda = \frac{m_g}{m_s} = \frac{9.3 \times 10^{-2}}{1.4 \times 10^{-1}}$$

$$a^2\lambda^2 = 1.81 \times 10^{-3}$$

Sample No.	0	1	2	3	4
$p \times 10^3$	13.0	10.0	9.5	9.0	8.9
$(p - p_1) \times 10^3$	11.0	8.0	7.5	7.0	6.9
$\frac{p - p_1}{p_2 - p_1}$	1.0	7.27×10^{-1}	6.82×10^{-1}	6.36×10^{-1}	6.27×10^{-1}
$\frac{\sqrt{Dt}}{a\lambda}$	0.0	3.13×10^{-1}	3.83×10^{-1}	4.62×10^{-1}	4.81×10^{-1}
$\frac{Dt}{a^2\lambda^2}$	0.0	9.80×10^{-2}	1.47×10^{-1}	2.14×10^{-1}	2.32×10^{-1}
Dt	0.0	1.77×10^{-4}	2.66×10^{-4}	3.87×10^{-4}	4.20×10^{-4}
t hours	0.0	28.0	53.0	76.0	98.0
t sec	0.0	1.01×10^5	1.91×10^5	2.74×10^5	3.53×10^5
D cm^2/sec.	-	1.76×10^{-9}	1.39×10^{-9}	1.41×10^{-9}	1.19×10^{-9}

Table continued . . .

TABLE 11 continued

Oxygen Diffusion Results

Temperature: 950°C.

Oxygen pressure: 365 mm Hg

Specimen: "Slab:, 1.28 mm thick
produced at 950°C.

Specimen weight: 0.534 g.

Run No.: 17-6

$a = \frac{L}{2} = 6.4 \times 10^{-2}$ cm.

$\lambda = \frac{m_g}{m_s} = \frac{9.3 \times 10^{-2}}{1.4 \times 10^{-1}} = 6.64 \times 10^{-1}$

$a^2\lambda^2 = 1.81 \times 10^{-3}$

Sample No.	5	6	7	8	9	10
$p \times 10^3$	8.7	8.6	8.2	8.1	7.7	7.5
$(p - p_1) \times 10^3$	6.7	6.6	6.2	6.1	5.7	5.5
$\frac{p - p_1}{p_2 - p_1}$	6.09×10^{-1}	6.00×10^{-1}	5.64×10^{-1}	5.55×10^{-1}	5.18×10^{-1}	5.00×10^{-1}
$\frac{\sqrt{Dt}}{a\lambda}$	5.15×10^{-1}	5.32×10^{-1}	6.10×10^{-1}	6.30×10^{-1}	7.22×10^{-1}	7.70×10^{-1}
$\frac{Dt}{a^2\lambda^2}$	2.65×10^{-1}	2.83×10^{-1}	3.72×10^{-1}	3.97×10^{-1}	5.21×10^{-1}	5.94×10^{-1}
Dt	4.80×10^{-4}	5.12×10^{-4}	6.73×10^{-4}	7.18×10^{-4}	9.43×10^{-4}	1.08×10^{-3}
t hours	123.0	151.0	172.0	221.0	267.0	312.0
t sec	4.93×10^{5}	5.44×10^{5}	6.19×10^{5}	7.96×10^{5}	9.61×10^{5}	1.12×10^{6}
D cm^2/sec	9.73×10^{-10}	9.41×10^{-10}	1.03×10^{-9}	9.02×10^{-10}	9.82×10^{-10}	9.64×10^{-10}

Average D = 1×10^{-9} cm^2/sec.

TABLE 12

Oxygen Diffusion Results

Temperature: 950°C.

Oxygen pressure: 365 mm Hg

Specimen: "Slab", 1.44 mm thick
produced at 1250°C.

Specimen weight: 0.545 g.

Run No.: 2-7

$$a = \frac{L}{2} = 7.2 \times 10^{-2} \text{ cm}$$

$$\lambda = \frac{m_g}{m_s} = \frac{9.3 \times 10^{-2}}{1.4 \times 10^{-1}} = 6.64 \times 10^{-1}$$

$$a^2\lambda^2 = 2.29 \times 10^{-3}$$

Sample No.	0	1	2	3	4
$p \times 10^3$	13.0	9.7	9.0	8.4	8.1
$(p - p_1) \times 10^3$	11.0	7.7	7.0	6.4	6.1
$\frac{p - p_1}{p_2 - p_1}$	1.0	7.00×10^{-1}	6.38×10^{-1}	5.82×10^{-1}	5.54×10^{-1}
$\frac{\sqrt{Dt}}{a\lambda}$	0.0	3.53×10^{-1}	4.58×10^{-1}	5.70×10^{-1}	6.32×10^{-1}
$\frac{Dt}{a^2\lambda^2}$	0.0	1.25×10^{-1}	2.10×10^{-1}	3.25×10^{-1}	4.00×10^{-1}
Dt	0.0	2.86×10^{-4}	4.81×10^{-4}	7.44×10^{-4}	9.16×10^{-4}
t hours	0.0	23.0	47.0	71.0	95.0
t sec	0.0	8.28×10^4	1.69×10^5	2.56×10^5	3.42×10^5
D cm^2/sec.	-	3.46×10^{-9}	2.85×10^{-9}	2.91×10^{-9}	2.68×10^{-9}

Table continued . . .

TABLE 12 continued

Oxygen Diffusion Results

Temperature: 950°C
Oxygen pressure: 365 mm Hg
Specimen: "Slab", 1.44 mm thick produced at 1250°C
Specimen weight: 0.545 g.
Run No.: 2-7

$a = \frac{L}{2} = 7.2 \times 10^{-2}$ cm

$\lambda = \frac{m_g}{m_s} = \frac{9.3 \times 10^{-2}}{1.4 \times 10^{-1}} = 6.64 \times 10^{-1}$

$a^2\lambda^2 = 2.29 \times 10^{-3}$

Sample No.	5	6	7	8	9	10
$p \times 10^3$	7.8	7.6	7.5	7.4	7.3	7.2
$(p - p_1) \times 10^3$	5.8	5.6	5.5	5.4	5.3	5.2
$\frac{p - p_1}{p_2 - p_1}$	5.27×10^{-1}	5.09×10^{-1}	5.00×10^{-1}	4.91×10^{-1}	4.82×10^{-1}	4.75×10^{-1}
$\frac{\sqrt{Dt}}{a\lambda}$	7.00×10^{-1}	7.45×10^{-1}	7.67×10^{-1}	7.95×10^{-1}	8.20×10^{-1}	8.40×10^{-1}
$\frac{Dt}{a^2\lambda^2}$	4.90×10^{-1}	5.55×10^{-1}	5.89×10^{-1}	6.32×10^{-1}	6.72×10^{-1}	7.06×10^{-1}
Dt	1.12×10^{-3}	1.27×10^{-3}	1.35×10^{-3}	1.45×10^{-3}	1.54×10^{-3}	1.62×10^{-3}
t hours	119.0	3.0	4.0	194.0	215.0	239.0
t sec.	4.78×10^5	5.14×10^5	5.90×10^5	6.98×10^5	7.74×10^5	8.60×10^5
D cm^2/sec.	2.34×10^{-9}	2.47×10^{-9}	2.29×10^{-9}	2.08×10^{-9}	1.99×10^{-9}	1.89×10^{-9}

Average $D = 2 \times 10^{-9}$

Table 13

Summary of experimental results for oxygen self-diffusion in stoichiometric zirconia

Temperature °C	Coefficient of self-diffusion D cm^2/sec.	Specimen
1000°	2 x 10^{-12}	Spheres, d = 9.0 x 10^{-3} cm
950°	7 x 10^{-13}	Spheres, d = 9.0 x 10^{-3} cm
	1 x 10^{-9}	"Slab", 1.28 x 10^{-1} cm. thick, originally produced by zirconium oxidation at 950°C.
	2 x 10^{-9}	"Slab, 1.44 x 10^{-1} cm thick originally produced by zirconium oxidation at 1250°C.
900°	3 x 10^{-13}	Spheres, d = 9.0 x 10^{-3} cm.
850°	1 x 10^{-13}	Spheres, d = 9.0 x 10^{-3} cm.
	4 x 10^{-12}	Irregular but equiaxed particles, d ≈ 6.0 x 10^{-3} cm., originally produced by zirconium oxidation at 950°C.
800°	3 x 10^{-14}	Spheres, d = 6.0 x 10^{-3}cm.

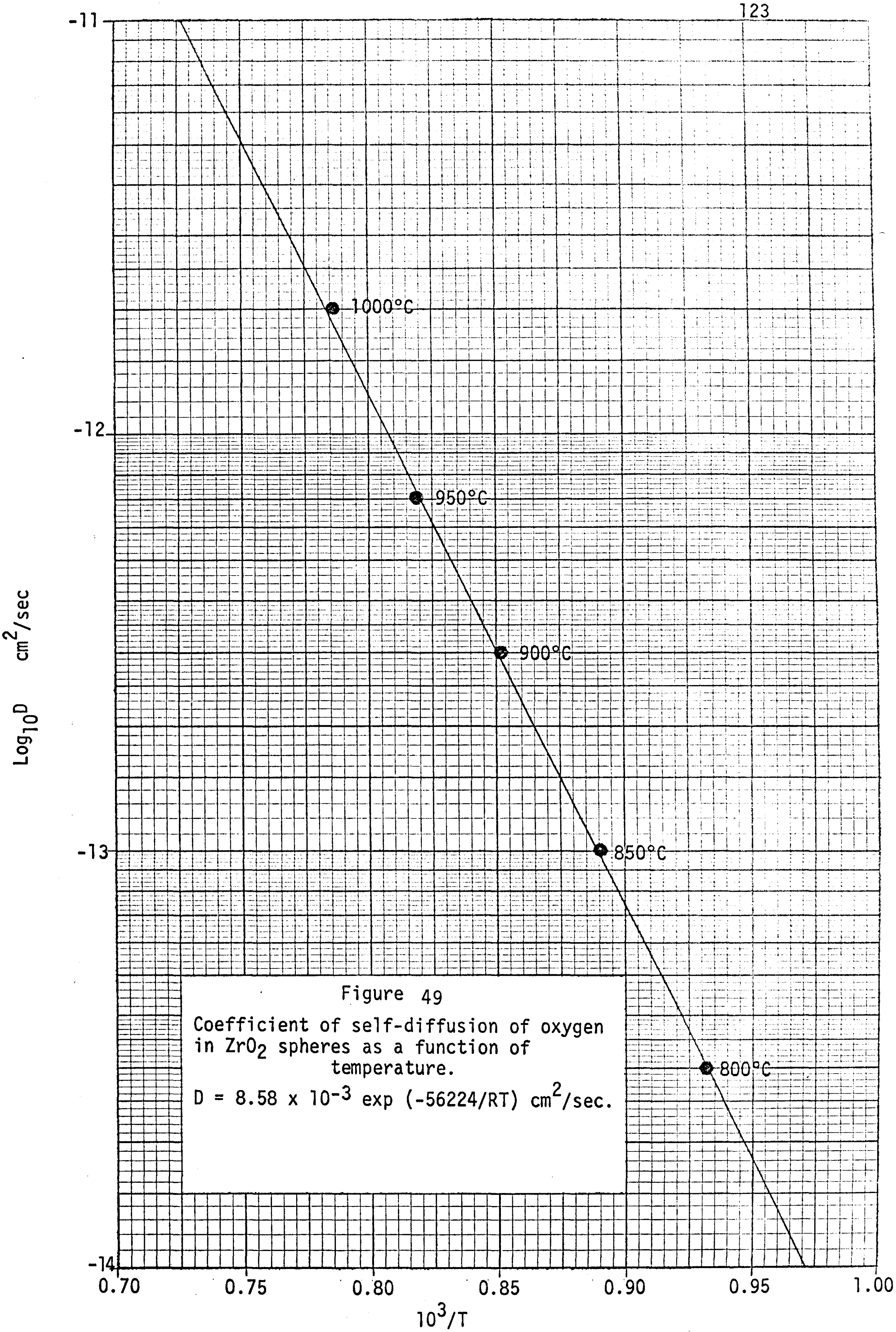

Figure 49

Coefficient of self-diffusion of oxygen in ZrO_2 spheres as a function of temperature.

$D = 8.58 \times 10^{-3} \exp(-56224/RT)\ cm^2/sec.$

CHAPTER 5

DISCUSSION OF RESULTS

5.1 Oxidation of Zirconium

Zirconium metal has a high solubility for oxygen at elevated temperatures as shown by the zirconium-oxygen constitution diagram in Figure 1. Consequently, at the first stages of oxidation, oxygen would be largely absorbed by the metal. Nucleation of oxide would also occur and lead first to growth of a thin layer of black zirconia followed by an external thin white layer as shown in Figure 24. A still later stage of the oxidation is illustrated by the photograph in Figure 25. An interesting feature of this specimen is that it consists only of white columnar zirconia and black zirconia with large, equiaxed grains, presumably corresponding to the original metal grains grown to a very large size during the oxidation anneal.

Columnar black zirconia, observed by other investigators, e.g. Wallwork et al(111) during formation of an oxide scale on zirconium was not present in this oxide. The reasons for this behaviour are not entirely clear. This specimen represents a later stage of oxidation than those photographed by previous investigators. The original external black columnar zirconia has been probably converted to a white columnar layer of ZrO_2, while the concentration of oxygen in the centre of the specimen has increased markedly, gradually filling up the original "oxygen trough" in the finite plate and substantially decreasing the concentration gradient of oxygen near the oxide-metal solid solution interface. Under these conditions, it is conceivable that a small supersaturated volume of the solution was produced ahead of the advancing columnar oxide interface, as a result of some thermal fluctuations. This could have caused a localized nucleation of black zirconia with the orientation related to the metal grain in which it was located. When such nucleation and growth became widespread, further growth of the columnar layer had to occur through recrystallization of the equiaxed grains of the oxygen deficient zirconia.

Another interesting feature of the specimen shown in Figure 25 is the very sharp transition of color from white zirconia across the interface to the black layer, with no intermediate shades of gray. This was observed also by other investigators(99). No information could be found in literature on the relation between the color perception of the human eye and the actual concentration of oxygen vacancies in zirconia, so it is possible that our visual observation on the degree of its blackness is not necessarily linearly related to the vacancy concentration. The majority of the hundreds of thousands of zirconia spheres seen by the author were either white or black, but there were perhaps three or four incompletely re-oxidized spheres which were gray. Consequently, is it possible that the sharp change in color does, in fact, correspond to an abrupt change in the vacancy concentration at the black-white zirconia interface, as advocated by Douglass and Wagner(99).

The direction of growth of the columnar oxide was related to the oxygen gradient in the sense that when this gradient changed direction, so did the long axis of the needle-like grains. Figures 50 and 51 show schematically the texture of an actual specimen at two stages of oxidation. The columnar layer split near the end of the strip as a result of high

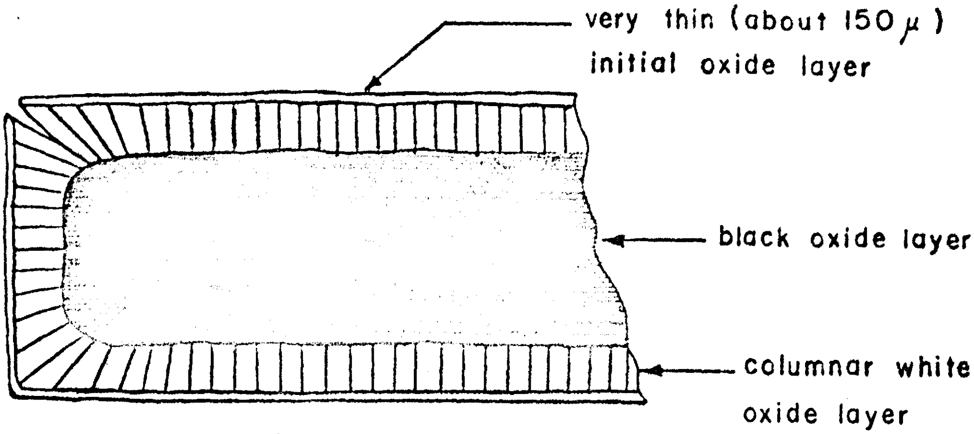

Figure 50

Initial direction of the columnar grains of the white oxide.

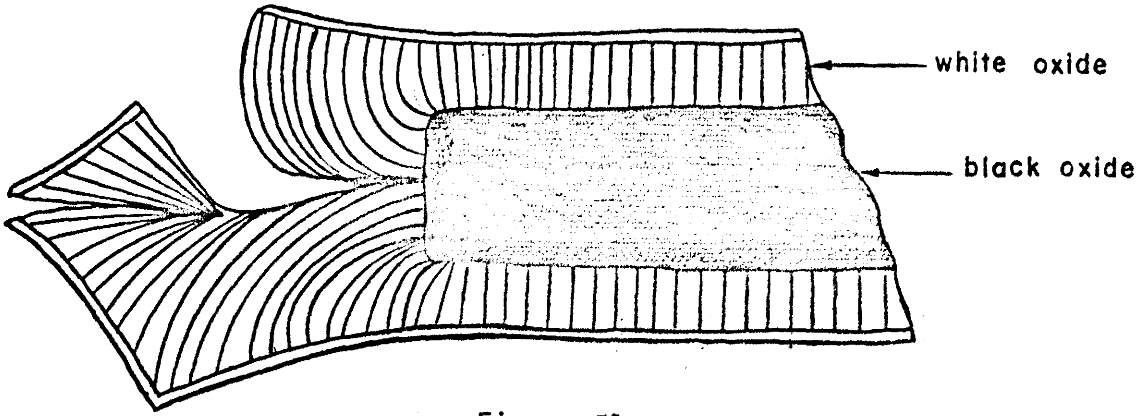

Figure 51

Direction of the columnar grains of the white oxide in some specimens at a more advanced stage of oxidation.

stress and the oxygen diffusion pattern changed, apparently causing the curving of the columnar grains. A somewhat similar phenomenon must have taken place during the oxidation of the specimen shown in Figure 29.

It was mentioned in Section 4.1 that zirconium specimens which were prematurely removed from the furnace before they had time to oxidize completely, were crushed, and separated into white and black particles. The black particles were returned to the furnace for complete oxidation. However, a compact, white zirconia layer did not form on them. The black oxide was instead oxidized fairly rapidly along parallel crystal planes and produced white, stoichiometric zirconia particles as shwon in Figure 32. The particles, when handled, easily disintegrated into a mass of white flakes with irregular edges. These were not suitable for subsequent spheroidizing because they interlocked while being dropped into the arc and either extinguished the arc or produced large, porous and deformed spheres. Possibly this type of oxidation was associated with formation of a number of microcracks in the black zirconia particles during the mechanical removal of the original white layer. These microcracks would serve as easy paths for access of oxygen. Expansion of black zirconia on oxidation to white at the walls of the cracks would account for the observed ultimate splitting. Similar thin, white platelets were formed in some black zirconia strips, as indicated by the white, irregular lines in Figure 27. These could have resulted from thermal cracking, or propagated from the white, columnar oxide. The white patches in Figure 25 are not white oxide colonies, but light reflections from the black zirconia surface.

5.2 Spheroidization of Zirconia

The metallographic examination of the black spheres described in Section 4.3 revealed that about 50% of the spheres were single phase or almost single phase zirconia, such as those illustrated in Figures 37 and 38. The remaining spheres, as shown in Figures 39 and 40, exhibited two-phase structures.

These structures were evaluated by comparing the above photomicrographs with those published by Domagala and McPherson(1) who examined the morphologies of various specimens with known ratios of zirconium to oxygen after annealing and quenching treatments. Fully stoichiometric zirconia contains 26 w/o O, and the black single phase spheres would be expected to contain approximately 24 w/o O, the fine striations of α-Zr saturated with oxygen (6.75 w/o O) being precipitated upon certain crystallographic planes by oxygen segregation across the oxide-metal solvus line upon cooling (Figures 38 and 39). The spheres of lowest oxygen content which exhibited structures characteristic of α-Zr rejected both at the eutectic temperature of 1900°C and upon cooling, would be close to 23 w/o O (Figure 40). It should be borne in mind that these percentage figures represent only an estimate because the amount and type of α-Zr present depend also on the rate of cooling of the spheres, which is neither known exactly nor controlled in the arc furnace.

5.3 Diffusion of Oxygen in Zirconia

5.3.1 Calculation of Enthalpy and Entropy Changes

In view of the fact that the diffusion measurements were conducted at oxygen partial pressures not far from atmospheric, the composition of the zirconia samples was virtually stoichiometric. Following the reasoning presented by Douglass and Wagner(99) it will also be assumed that the ionic defects present in the specimens were interstitial oxygen and oxygen vacancies (anti-Frenkel defects), in equal concentrations to satisfy the condition of the stoichiometry.

It has been shown by Shewmon(112) from electric conductivity experiments on silver bromide that to a good approximation interstitial and vacancy point defects move independently. The same should be true for zirconia, so that the total ionic electric conductivity can be taken as the sum of the conductivities for each type of defect. This was also implicitly assumed by Douglass and Wagner(99) when they wrote the expression for the ionic conductivity quoted in Section 2.5 as Eq. (11):

$$\kappa_{ion} = 2\ F\ (u_o\ x_o + u_v\ x_v)/V_m \tag{1}$$

Similarly, κ_{ion} for doubly charged defects may be expressed in terms of the total ionic concentration x_{ion} and the total ionic mobility u_{ion}:

$$\kappa_{ion} = 2\ F\ u_{ion}\ x_{ion}/V_m \tag{2}$$

Comparing equations (1) and (2), and remembering that $x_{ion} = 1$,

$$u_{ion} = u_o\ x_o + u_v\ x_v \tag{3}$$

This equation may be used for relating the corresponding diffusion coefficients D_{ion}, D_o and D_v introduced through the Nernst-Einstein equation

$$D_{ion} = u_{ion}\ RT/2\ F \tag{4a}$$

$$D_o = u_o\ RT/2\ F \tag{4b}$$

and

$$D_v = u_v\ RT/2\ F \tag{4c}$$

where R = gas constant

T = absolute temperature.

Thus

$$u_{ion} = \frac{2\ F\ D_{ion}}{RT} \quad \text{, etc.,}$$

so that

$$D_{ion} = D_o\ x_o + D_v\ x_v \tag{5}$$

This equation has been developed for ionic electrochemical diffusion. It may be considered valid for self-diffusion (tracer diffusion) if we substitute the corresponding self-diffusion coefficients

$$D^* = D_o^* + D_v^* \tag{6}$$

This is justified on the following grounds. The coefficient of self-diffusion D* is related to the coefficient of chemical diffusion Dx by the equation

$$Dx = D^*\ (1 + \frac{d\ \ln\ \gamma}{d\ \ln\ N}) \tag{7}$$

where

γ = activity coefficient of the diffusing species

N = mole fraction of the diffusing species.

For Dx to be exactly equal to D*, there must be then

$$\frac{d\ \ln\ \gamma}{d\ \ln\ N} = 0,$$

that is γ = constant.

This is true for ideal solutions, and approximately correct for dilute solutions where γ is practically constant for the solute as shown by Henry's law, and for the solvent, as described by Raoult's law.

Let us consider now the oxygen tracer diffusion by a vacancy mechanism using the "Random Walk" model. The tracer flux along the diffusion axis is equal to the difference between the "forward" flux J_{12} from plane 1 to plane 2, and the "reverse" flux J_{21} from plane 2 to plane 1. The forward flux is

$$J_{12} = \beta_2 \, n_1 \, p_{v_2} \, w_{12} \tag{8}$$

where β_2 = number of nearest neighbors on the "forward" plane 2.

n_1 = number of tracer atoms per unit area of plane 1.

p_{v_2} = probability that any site on plane 2 is vacant.

w_{12} = frequency for atom jump from plane 1 to 2.

Similarly, the reverse flux is

$$J_{21} = \beta_1 \, n_2 \, p_{v_1} \, w_{21}. \tag{9}$$

Since all isotopes of oxygen are assumed to diffuse in the same way, $w_{21} = w_{12}$ and $p_{v_1} = p_{v_2}$. Furthermore, the numbers of tracer atoms available for the jump are equal to $n_1 = \alpha C_1$ for plane 1, and $n_2 = \alpha C_2$, where C_1 and C_2 are the corresponding concentrations, and α is the plane separation. Finally, since 1 and 2 can represent any parallel neighboring crystal planes in a zirconia sphere, depending on the grain orientation, there must be $\beta_1 = \beta_2 =$ (average) β.

The net flux is then equal to

$$J = J_{12} - J_{21} = \beta \, \alpha \, p_v \, w \, (C_1 - C_2) \tag{10}$$

Since $C_1 - C_2 = -\alpha \frac{\partial C}{\partial y}$, (11)

where y is the diffusion axis,

$$J = -\beta \, \alpha^2 \, p_v \, w \frac{\partial C}{\partial y} \tag{12}$$

From the assumed equivalence of all oxygen isotopes, it follows that p_v must be equal to the fraction of sites vacant, or $p_v = x_v$.

Comparing Eq. (12) with the first Fick's law, we get

$$D_v^* = \beta\, \alpha^2\, x_v\, w \tag{13}$$

For the interstitial oxygen tracer diffusion a similar equation may be derived,

$$D_O^* = \eta\, \alpha^2\, w \tag{14}$$

Since we are dealing in this case with a very dilute solution, w is independent of composition, and the mole fraction of vacant interstitial sites is essentially unity, so that it does not appear in the above equation. The coefficient η is a geometric constant.

The quantities in equations (13) and (14) may be evaluated in terms of thermodynamic considerations. At equilibrium,

$$x_v \equiv \exp\left(\frac{-\Delta F_v}{RT}\right) \tag{15}$$

where $\Delta F_v \equiv \Delta H_v - T \Delta S_v$ is the free energy change of an infinite crystal, per mole of vacancies added, over and above the entropy of mixing; ΔH_v and ΔS_v are the corresponding enthalpy and entropy changes.

The second unknown quantity which appears in the expressions for D^* is w. The most common method of calculating w is by the use of the concept of "activated complexes", i.e. regions containing an atom midway between two equilibrium sites. Using this method of derivation, w may be expressed as

$$w = \nu \exp\left(- \frac{\Delta F_m}{RT}\right) \tag{16}$$

where ΔF_m is the change in the Gibbs free energy involved in a reversible, isothermal formation of an activated complex. This free energy change is identical with

$$\Delta F_m \equiv \Delta H_m - T \Delta S_m, \tag{17}$$

The pre-exponential factor ν is the frequency with which the atoms at the saddle point jump to the new site. It may be shown that ν is of the order of the mean vibrational frequency of an atom about its equilibrium site.

Substituting Equations (15) and (16) into (13) and (14), we obtain

$$D_v^* = f_v \, \beta \, \alpha_v^2 \, \nu_v \exp\left(\frac{-\Delta F_v}{RT}\right) \exp\left(\frac{-\Delta F_{mv}}{RT}\right) \tag{18}$$

and

$$D_o^* = f_o \, \eta \, \alpha_o^2 \, \nu_o \exp\left(\frac{-\Delta F_{mo}}{RT}\right) \tag{19}$$

where f_v and f_o are ion jump correlation factors.

Introducing these expressions into Equation (6), an exponential form is obtained for D^*:

$$D^* = f_o \, \eta \, \alpha_o^2 \, \nu_o \exp\left(\frac{-\ F_{mo}}{RT}\right) + f_v \, \beta \, \alpha_v^2 \, \nu_v \exp\left(\frac{-\Delta F_v}{RT}\right) \exp\left(\frac{-\Delta F_{mv}}{RT}\right) \tag{20}$$

Expressing the free energy changes as sums of enthalpy and entropy terms, and re-arranging the exponents,

$$D^* = f_o \, \eta \, \alpha_o^2 \, \nu_o \exp\left(\frac{\Delta S_{mo}}{R}\right) \exp\left(\frac{-\Delta H_{mo}}{RT}\right) + f_v \, \beta \, \alpha_v^2 \, \nu_v \exp\left(\frac{\Delta S_v + \Delta S_{mv}}{R}\right) \exp\left(\frac{-\Delta H_v - \Delta H_{mv}}{RT}\right) \tag{21}$$

This diffusion coefficient represents the coefficient of self-diffusion of oxygen measured in the O^{18} exchange tests.

In view of the fact that the results shown in Figure 49 could be represented by a linear Arrhenius plot, $D^* = D_o \exp\left(\frac{-Q}{RT}\right)$, it appears that only one exponential term including T was involved, and not a sum of two, as indicated by Equation (21). This suggests that one of the diffusion mechanisms, either vacancy or interstitial, was predominant, with the other one adding perhaps only a minor, or even negligible contribution. The results obtained by Ure(100) on CaF_2, which has a structure similar to ZrO_2, have proven that the mobility of anion vacancies in fluorite type structure is much greater than that of interstitial ions. Since the concentrations of the two types of point defects are equal (anti-Frenkel defects), the diffusion rate of interstitial oxygen ions should be much lower.

We have assumed that these two types of defects move independently, so that the total rate of diffusion is determined by the faster mechanism. In the first approximation we may write then

$$D^* = f_v \, \beta \, \alpha_v^2 \, \nu_v \exp \left(\frac{\Delta S_v + \Delta S_{mv}}{R}\right) \exp \left(\frac{-\Delta H_v - \Delta H_{mv}}{RT}\right) \qquad (22)$$

Comparing this equation with that obtained experimentally and listed in Section 4.6,

$$D^* = 8.58 \times 10^{-3} \exp(-56224/RT) \ \text{cm}^2/\text{sec} \qquad (23)$$

we get

$$\Delta H_v + \Delta H_{mv} = 56224 \text{ cal/mole.}$$

which is the enthalpy of formation (ΔH_v) and migration (ΔH_{mv}) of oxygen vacancies in the stoichiometric zirconia. It is of interest that this activation energy is practically equal to that obtained by Aronson(102) for non-stoichiometric zirconia (58000 cal/mole.). The numerical interpretation of the individual factors in the pre-exponential coefficient is difficult and uncertain. Apparently,

$$f_v \, \beta \, \alpha_v^2 \, \nu_v \exp \left(\frac{\Delta S_v + \Delta S_{mv}}{R}\right) = 8.58 \times 10^{-3} \qquad (24)$$

The ion jump correlation coefficients for vacancy diffusion in various crystal structures usually vary between 0.5 and 0.8[(112)], so that assuming $f_v = 0.65$ should not be far from the actual figure. The factor β, which is the number of nearest neighbors in the "forward" jump plane, can be taken in the first approximation as 1/3 of the average coordination number for oxygen ions in zirconia. This involves a simplifying assumption that 1/3 of all the nearest neighbors are in the same plane (perpendicular to the diffusion axis) as the ion ready to jump, 1/3 of the neighboring sites are in the "reverse" jump plane, and 1/3 are located in the "forward" jump plane. This makes $\beta = 3$ approximately (see Section 2.1). The value of α_v, the "forward" component of an average jump, i.e. the distance between the plane containing the ion ready to jump and the "forward" plane into which it is jumping, is of the order of 2.5×10^{-8} cm. The frequency with which the ions at the saddle point go to the new site, ν, is usually taken equal to the Debye frequency, 7×10^{12} approximately. Introducing these values into Equation (24), we get

$$0.65 \times 3 \times 6.25 \times 10^{-16} \times 7 \times 10^{12} \exp\left(\frac{\Delta S_v + \Delta S_{mv}}{R}\right) = 8.58 \times 10^{-3} \quad (25)$$

$$8.52 \times 10^{-3} \exp\left(\frac{\Delta S_v + \Delta S_{mv}}{R}\right) = 8.58 \times 10^{-3} \quad (26)$$

This relation demonstrates that $(\Delta S_v + \Delta S_{mv})$ has a very small positive value.

5.3.2 Comparison with Results of Other Investigators

Figure 52 shows the comparison between the results of this study and the diffusivity values obtained by previous investigators for the diffusion of oxygen in zirconia. It will be seen that the D values obtained

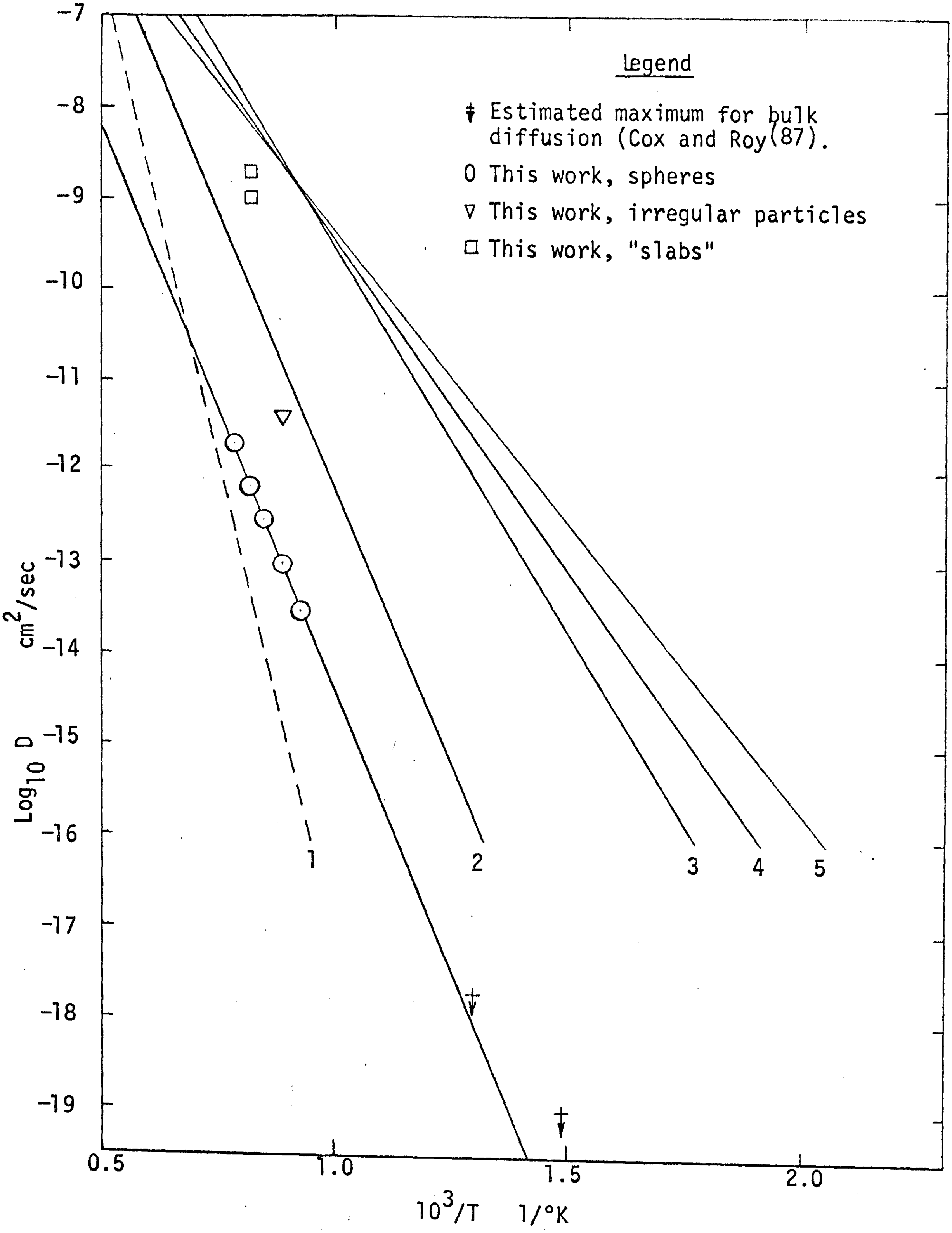

Figure 52

Diffusion of oxygen in zirconia

1 - McClaine(103) - estimated intrinsic diffusion
2 - Aronson (102) - substoichiometric powder
3 - Cox and Roy(87) - ion bombardment of scale on Zr
4 - Douglass(86) - sintered substoichiometric zirconia
5 - Debuigne and Lehr(79) - calculated from Zr oxidation.

in the spheres are about 4 orders of magnitude lower than those measured by Debuigne and Lehr(79), Douglass(86), and Cox and Roy(87), and 2 orders of magnitude lower than Aronson's(102) values. It is of considerable interest to analyze this disparity.

There are several possible factors accounting for the difference:

1) Electrochemical diffusion vs. self-diffusion.
2) Higher vacancy concentration in substoichiometric zirconia.
3) Different experimental techniques.
4) Larger number of structural defects in zirconia scale on metal, forming short-circuit diffusion paths for oxygen ions.

We shall discuss these factors in turn.

The electrochemical potential gradient during the oxidation of zirconium accelerates the migration of oxygen ions through the oxide scale. Consequently, the coefficient of electrochemical diffusion is expected to be higher than that of self-diffusion. However, theoretical considerations made by Douglass and Wagner(99) indicate that this acceleration of diffusion is not extremely high. For instance, at low oxygen partial pressures, such as possibly exist in the zirconium oxide near the metal interface, the ambipolar diffusion coefficient was calculated to be 3 times the diffusion coefficient of oxygen vacancies, because the movement of the anions is supported by a diffusion potential due to the tendency of the faster electrons to move ahead. The diffusion coefficients calculated by Debuigne and Lehr(79) from the oxidation studies were not 3, but 10,000 times higher than measured in the present study.

Allowing even for the accelerating effect of the vacancy concentration on vacancy diffusion, this still does not explain the above disparity. A proof that this, in fact, is not a decisive factor, is supplied by the measurements of the coefficient of diffusion of oxygen in the zirconia "slabs". These slabs had no oxygen gradient and were stoichiometric, so that they had the same vacancy concentrations as the spheres, yet the coefficients of oxygen diffusion in them were less than one order of magnitude lower than that determined in the oxide scale. In fact, the slabs were the oxide scale with the electrochemical gradients eliminated, but the columnar crystal structure and the line defects retained. These slabs were tested under identical experimental conditions and in the same apparatus as the spheres, so that the method of measuring could not have been responsible for the high ratio of the diffusivities.

The main factor responsible for the large difference of the coefficients of diffusion appears to be then the presence of easy paths for oxygen diffusion in the oxide scale on metal. In other words, the values measured by the three groups of investigators mentioned above were actually effective diffusion coefficients embracing both short-circuit and lattice diffusion. Thus, thanks to the development of a new method for preparation of zirconia spheres it has been possible to approach lattice diffusion of oxygen much closer than it was feasible in the past.

The fact that oxidation of zirconium is determined largely by short-circuit diffusion of oxygen through zirconia was actually anticipated by some investigators. For instance, Smeltzer et al(113) developed an equation for the oxidation of metals by short-circuit and lattice diffusion of oxygen using the relation given by Hart(117) for the effective diffusion coefficient,

$$D_{eff} = D_L (1 - f) + D_B f \tag{1}$$

where:

D_{eff} = effective diffusion coefficient
D_L = lattice diffusion coefficient
D_B = short circuit diffusion coefficient
f = fraction of the total available oxygen sites lying within low resistance paths in the oxide film.

Accordingly,

$$\frac{D_{eff}}{D_L} = 1 - f + \frac{D_B}{D_L} f \cong \frac{D_B}{D_L} f \tag{2}$$

or

$$\frac{D_B}{D_L} = \frac{D_{eff}}{D_L f} \tag{3}$$

According to Chute(114) the crystallite size in zirconia is about 100Å = 10^{-6} cm. Assuming that the short circuit paths for the diffusion are mainly the grain boundaries, and using the model shown in Figure 53, the grain boundary area per 1 cm^2 in a plane normal to the diffusion axis is

$$f \cong 2 \times \left(\frac{1}{10^{-6}}\right) \times (5 \times 10^{-8} \times 1) = \frac{10^7}{10^8} = 10^{-1} \text{ cm}^2$$

Taking (for 950°C) D_{eff} = D for slabs $\cong 2 \times 10^{-9}$ cm^2/sec., and D_L = D for spheres $\cong 7 \times 10^{-13}$ cm^2/sec. we obtain

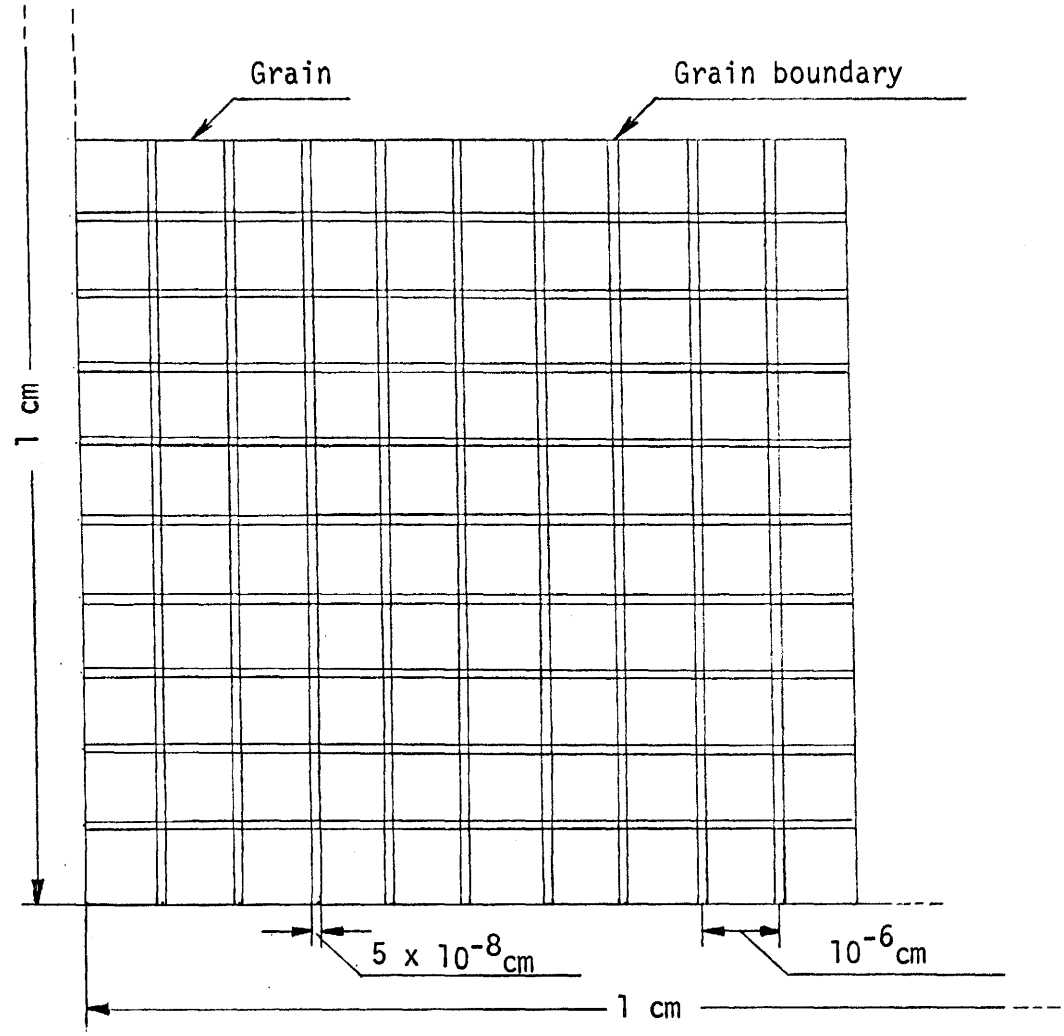

Figure 53

Model for calculating grain boundary area per 1 cm^2 of a plane perpendicular to the diffusion path.

$$\frac{D_B}{D_L} = \frac{2 \times 10^{-9}}{7 \times 10^{-13} \times 10^{-1}} \cong 3 \times 10^4$$

This ratio is that to be expected when diffusion in a solid is essentially determined by grain boundary diffusion.

Cox(87) also predicted that the oxygen diffusion in the oxide scale layer occurs through the short-circuit paths, and his estimated maximum values for the lattice diffusion are quite close to the values extrapolated from this study. (See Figure 52).

5.3.3 Calculation of Concentration Drop of Oxygen Across Zirconia Scale on Metal

In this and the following section , the experimental results and results by other investigators will be used to calculate some quantities pertaining to the parabolic oxidation behaviour of zirconium. Wallwork, Smeltzer and Rosa(111) determined the oxidation kinetics of alpha-zirconium at 850°C. For the theoretical analysis of their results, they used a model advanced by Wagner(115) for diffusion in a two-phase system, the metal phase being an infinite plate.

According to this analysis, the oxygen uptake per unit area would be

$$\frac{\Delta M}{A} = Kp \sqrt{t} = [Kp(\text{oxide}) + Kp(\text{metal})] \sqrt{t} \qquad (1)$$

where Kp(oxide) and Kp(metal) represent constants in the parabolic relationships for oxide growth and oxygen solution in the metal, respectively, and t is time. The parabolic constants may be expressed also as

$$Kp(\text{oxide}) = 2\gamma \, (C_{II}^{I} - C_{I}^{II}) \sqrt{D_{II}} \qquad (2)$$

and

$$Kp(\text{metal}) = 2B_1 \sqrt{D_I/\Pi} \; \exp\left(- \frac{\gamma^2 D_{II}}{D_I}\right) \qquad (3)$$

where D_{II} and D_I are the oxygen diffusion constants in zirconia and zirconium respectively, C_{II}^{I} and C_{I}^{II} are the oxygen concentrations in the oxide and metal respectively, at the metal/oxide interface, B_1 and γ are constants. The oxide thickness ε at a time t is equal to

$$\varepsilon = 2\gamma \sqrt{D_{II}} \quad \sqrt{t} = \frac{K_p \text{ (oxide)}}{C_{II}^{I} - C_{I}^{II}} \quad \sqrt{t} \tag{4}$$

Using this equation, Wallwork et al(111) calculated Kp(oxide) for 850°C after $\varepsilon/\sqrt{t}$ was determined experimentally, and the oxygen concentrations were taken as $C_{II}^{I} = 1.514 \text{ g/cm}^3$ and $C_{I}^{II} = 0.439 \text{ g/cm}^3$ from Domagala and McPherson's(1) zirconium-oxygen constitution diagram. The total parabolic oxidation constant Kp was calculated from the experimental results using the equation

$$\frac{\Delta M}{A} = Kp \sqrt{t} \tag{5}$$

Finally, Kp(metal) was determined for 850°C as

$$Kp(\text{metal}) = Kp - Kp \text{ (oxide)} \tag{6}$$

Employing the same method, Hussey and Smeltzer(116) calculated the values of these quantities from their results for zirconium oxidation at 600°C. The two sets of values for the Kp's are shown in Table 14

The values from Table 14 may be used for the determination of the oxygen concentration drop across the oxide (see Figure 54)

$$\Delta C = C_{II}^{0} - C_{II}^{I} \tag{7}$$

According to Fick's First Law,

$$J = \frac{d}{dt}\left(\frac{\Delta M}{A}\right) = - D_{II} \frac{\partial C}{\partial x} \simeq -D_{II} \frac{\Delta C}{\Delta x} = - D_{II} \frac{\Delta C}{\varepsilon} \tag{8}$$

TABLE 14

Parabolic Rate Constants for Oxidation of Zirconium at 850°C and 600°C.

Temperature	Kp $g/cm^2\ sec.^{1/2}$	Kp(oxide) $g/cm^2\ sec.^{1/2}$	Kp(metal $g/cm^2\ sec.^{1/2}$
850°C	2.1 x 10^{-5}	(0.75 ± 0.08) x 10^{-5}	(1.35 ± 0.30) x 10^{-5}
600°C	2.00 x 10^{-6}	1.27 x 10^{-6}	0.73 x 10^{-6}

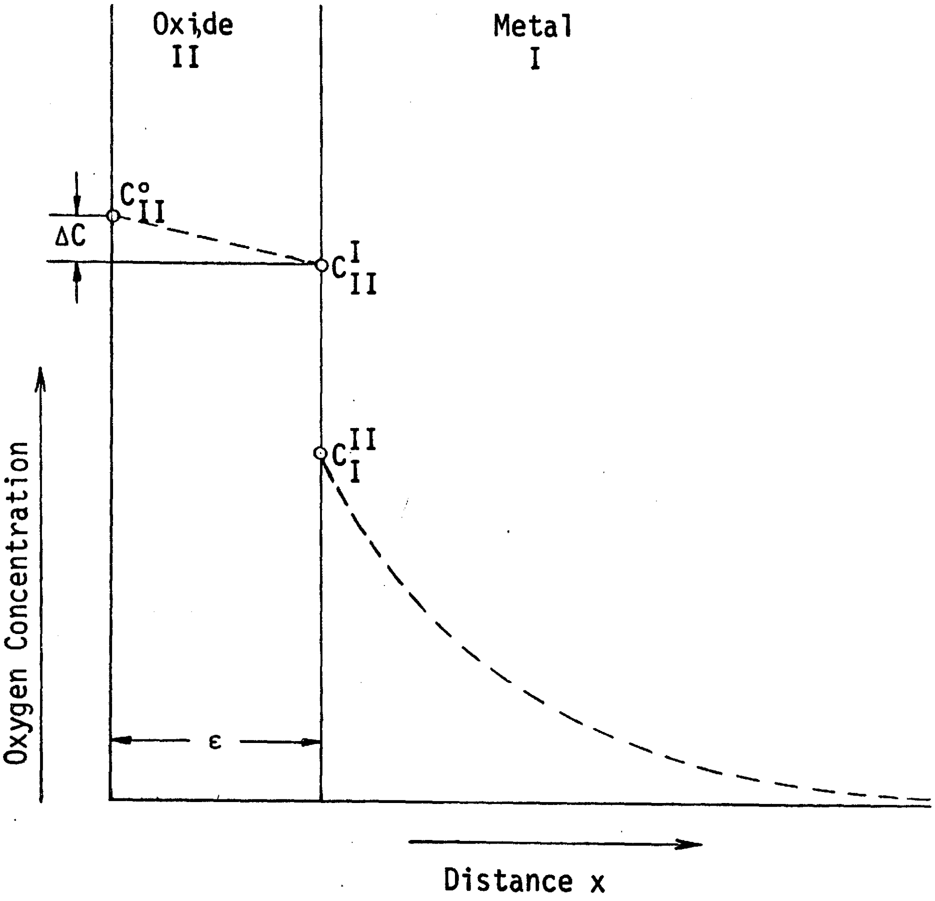

Figure 54

Oxide-Metal diffusion model for parabolic oxidation

Substituting Equation (5) into the left side of Equation (8)

$$J = \frac{d}{dt}(Kp\sqrt{t}) = \frac{Kp}{2\sqrt{t}} \qquad (9)$$

Comparing Equations (8) and (9),

$$\Delta C = \frac{Kp\ \varepsilon}{2D_{II}\sqrt{t}} \qquad (10)$$

Substituting Equation (4) for ε

$$\Delta C = \frac{Kp\ Kp(\text{oxide})}{2D_{II}\ (C_{II}^{I} - C_{I}^{II})} \qquad (11)$$

In this equation, only the magnitude of D_{II} needs now to be known to calculate the corresponding value of ΔC. The diffusion coefficients D_{II} extrapolated from the data published by Debuigne and Lehr(79), Douglass(86), and Cox and Roy(87), discussed in Section 2.6 of this thesis, are listed in Table 15.

The average values are then,

for 850°C :

$$D_{II} = 2 \times 10^{-9}\ \text{cm}^2/\text{sec}.$$

for 600°C :

$$D_{II} = 3 \times 10^{-11}\ \text{cm}^2/\text{sec}.$$

Substituting these values into Equation (11) yields

$$\Delta C_{850^\circ} \simeq 0.04\ \text{g/cm}^3$$

$$\Delta C_{600^\circ} \simeq 0.04\ \text{g/cm}^3$$

The oxygen concentration drop across the oxide layer is then fairly small compared to the drop across the oxide-metal interface which is

TABLE 15

Coefficients of Diffusion of Oxygen Through Zirconia Scale During Oxidation of Zirconium Metal (Extrapolated Values)

	D_{II}, cm^2/sec.		
Temperature	Debuigne & Lehr(79)	Douglass(86)	Cox & Roy(87)
850°C	2×10^{-9}	2×10^{-9}	2×10^{-9}
600°C	5×10^{-11}	3×10^{-11}	2×10^{-11}

more than 1 g/cm^3. It appears also that ΔC does not change rapidly with temperature, the difference between 850°C and 600°C being less than 0.005 g/cm^3.

CHAPTER 6

CONCLUSIONS

1. Black, substoichiometric zirconia has a higher ductility than the white oxide. Consequently, black zirconia successfully withstands the polymorphic transformation while the white, stoichiometric oxide cracks.

2. Using a method developed in this study, it is possible to produce white zirconia spheres, 45μ - 105μ diameter, of a quality suitable for oxygen diffusion experiments. The method consists in spheroidizing zirconia in an electric arc with a reducing atmosphere which produces sub-stoichiometric spheres. The spheres are subsequently re-oxidized at a temperature below the polymorphic transformation range.

3. The coefficient of oxygen self-diffusion in stoichiometric zirconia, determined by O^{18} exchange using the spheres, obeys the Arrhenius law expressed by the equation,

   $$D = 8.58 \times 10^{-3} \exp(-56224/RT) \text{ cm}^2/\text{sec}$$

   within the temperature range 800° - 1000°C.

4. Theoretical considerations indicate that this diffusion occurs by a vacancy mechanism.

5. The activation energy for this diffusion, 56224 cal/mole, is very close to that measured by Aronson(102) in substoichiometric zirconia, 58,000 cal/mole. The entropy change associated with this diffusion

was a very small positive value.

6. The coefficients of oxygen self-diffusion in two stoichiometric zirconia "slabs" produced by oxidation of metal strips, were determined as 1×10^{-9} and 2×10^{-9} cm^2/sec respectively, at 950°C. The first slab was originally produced in the monoclinic region, while the second was formed in the tetragonal region. These values are almost 10^4 times higher than the coefficient of self-diffusion for stoichiometric zirconia spheres at the same temperature. Theoretical considerations indicate that this was caused by short-circuit diffusion in the slabs.

7. The coefficient of oxygen diffusion in the slabs was less than one order of magnitude lower than that calculated for zirconia scale from oxidation experiments. This points out to short-circuit diffusion as the major mechanism during oxidation of zirconium.

8. The oxygen concentration drop across zirconia scale on metal, during its formation by parabolic kinetics was calculated for 600°C and 850°C and was found to be 0.04 g/cm^3 approximately, while the concentration drop across the interface between the oxide and the oxygen-saturated metal was about 1.07 g/cm^3.

9. At a certain stage of zirconium oxidation, black equiaxed zirconia forms ahead of the moving boundary of the columnar oxide. Oxide nucleation from islands of supersaturated solution of oxygen in the metal, produced by thermal fluctuations, may be responsible for this phenomenon.

CHAPTER 7

RECOMMENDATIONS FOR FUTURE WORK

Zirconia spheres produced by the method developed in this investigation consitute a powerful tool for the investigation of oxygen diffusion in zirconia. As a next step, measurements in the tetragonal region of temperatures may be carried out with the following procedure. Black spheres can be heated in vacuum or in a reducing atmosphere through the polymorphic transformation range without cracking. While in the tetragonal region, the spheres may be slowly re-oxidized with O^{16}, after which O^{16} is pumped out and O^{16} O^{18} quickly admitted for the oxygen exchange experiment.

Another series of experiments may involve oxygen diffusion in spheres at various low partial pressures of oxygen in H_2 - H_2O or CO-CO_2 atmospheres using O^{18}. These spheres could be pure zirconia and this oxide doped with metallic additives of different valences. The results from these investigations could be used to test the validity of the model proposed by Douglass and Wagner(99) for the anion and electron defect structure of zirconia.

Another interesting field of study would be the investigation of the possible nucleation of equiaxed black zirconia ahead of the columnar oxide boundary, and its effect on the oxidation kinetics.

APPENDIX I

Conductivity measurements of aqueous KF solutions

The purpose of these measurements was to determine the optimum concentration of KF in the O^{18}-containing water to produce improved electrical conductivity necessary for the electrolysis. Non-isotopic distilled water was used for the measurements. Anhydrous potassium fluoride, reagent grade, with a guaranteed minimum KF content of 99.0 w/o, was supplied by the General Chemical Division of the Allied Chemical Corporation, N. Y. The same potassium fluoride was used later for the electrolysis of the isotopic water. The instrument used for the determination of conductivity was Model RC 16 B2 Conductivity Bridge made by Industrial Instruments, Inc. The measurements were made using a standard cell with platinized electrodes. The results obtained at room temperature for six concentrations of potassium fluoride are shown in Table 16 .

TABLE 16

Results of KF Solution Conductivity Measurements

Temperature: 25°C. Current frequency: 1000 c/sec.
Cell constant: $k = 0.02\ cm^{-1}$.

KF Concentration w/o	Measured resistance of electrolyte in cell, R ohm	Specific conductance of electrolyte, $\frac{k}{R}$ mho/cm.
2	1.25	0.0160
5	0.95	0.0210
10	0.68	0.0294
15	0.43	0.0465
20	0.38	0.0526
25	0.37	0.0540

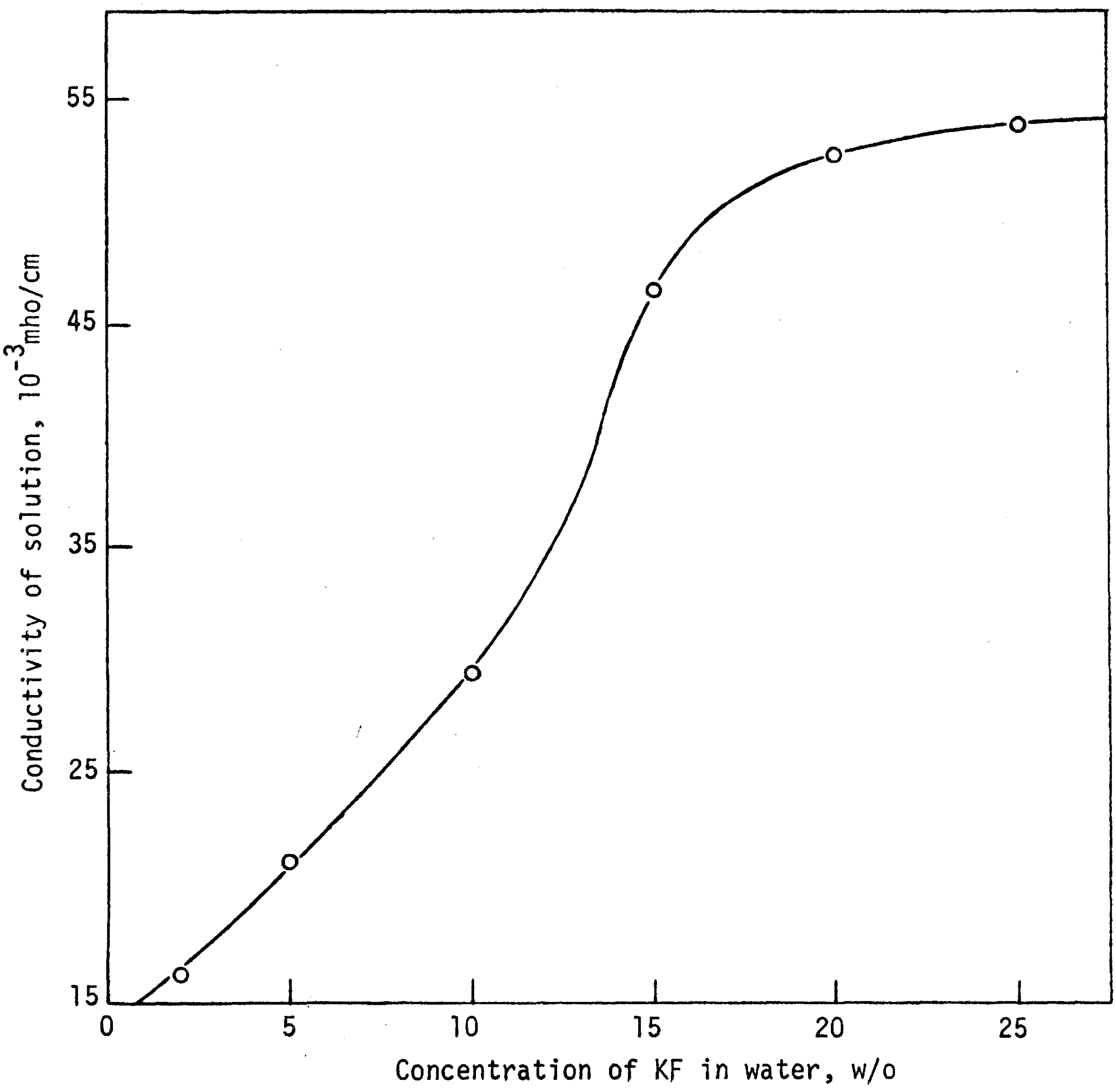

Figure 55

Electric conductivity of aqueous solution of KF as a function of concentration.

APPENDIX II

Preparation and testing of filament for mass spectrometer

In view of the gradual oxidation of a tungsten filament when exposed to oxygen at the normal operating temperature, it appeared desirable to substitute a more durable material for this part of the mass spectrometer. Review of literature suggested that iridium ribbon coated with thoria may provide an answer to the problem.

Hanley(104) who investigated materials for high frequency vacuum tube cathodes, found that the mildly radioactive ThO_2 is most promising. He described also a method of depositing thoria on a metal substrate using electrophoresis. In this process finely divided particles of an insulator suspended in a liquid are deposited onto a metallic cathode in a manner resembling ordinary plating. Hanley determined also high temperature conductivity and thermionic emissivity of thoria cathodes.

Weinreich(105) found that thoria-coated iridium cathodes in ionization gauges were not damaged when exposed hot to open air, and continuous pressure readings in O_2 could be made up to 10^{-2} mm. Hg. Weinreich and Bleecher(106) used a thoriated iridium cathode and found that at a current of 200 m a/cm^2 the filament life, limited by disappearance of the coating, is nearly 10,000 hours.

Goldwater and Danforth(107) determined thermionic emission constants for iridium, and Melton(108) described the use of a thoria-coated iridium filament as a source of ionizing electrons in mass spectrometry. The dimensions of the filament used in his research were 1 x 0.031 x 0.003 in.

A current of 6 amperes produced a temperature of 1400°C and a trap current of 8 μ a. The same trap current could be produced by a current of 3.5 amperes through a tungsten filament having dimensions of 1 x 0.030 x 0.001 in., however, the temperature of the tungsten filament was considerably higher than 2500°C.

Melton has listed the following advantages of the thoria-coated iridium filaments for mass spectrometry:

1) Lower operating temperature, hence, lower source temperature.
2) No "conditioning" required.
3) Chemically resistant to corrosive gases such as Cl_2 and O_2.
4) Constant emission characteristics after repeated exposure to corrosive gases.
5) No increase in the number of background ion beams produced by reaction products from the filament.

In view of the above findings, hard rolled iridium ribbon, 0.030 in. wide and 0.0015 in. thick was purchased for this study. The ribbon was flame annealed, cut into 1/4 pieces and spot-welded to the nickel posts of the filament holders. Each filament was then immersed in turn in a 250 ml. glass beaker containing a bath of 200 ml. of 95% ethyl alcohol in distilled water, 0.150 grams of thorium nitrate and 10 grams of ThO_2 powder obtained from the Fisher Scientific Company. The powder was kept in suspension by constant agitation with a motor-driven glass stirrer. A D.C. voltage of 8 volts was applied between the filament, which was a negative electrode, and a positive electrode made of a piece of nickel sheet, 1 in. x 2 in. in size. The distance between the electrodes was 1/2 in. approximately. The current was 1 m amp, and the time of deposition 10 min. These conditions were selected after a large number of experiments, because the thickness and the quality of the coating is strongly affected by the shape and size of the filament, the geometry of the system, degree and direction of stirring etc., as well as the time and current of the electrophoretic deposition.

To test the filaments a vacuum bell jar was temporarily attached to the sample line of the mass spectrometer. Each filament in turn was mounted in a spare ionization source unit under the bell jar, which was then evacuated. The electric input and output of the unit was measured with the mass spectrometer power control ammeters and voltmeters. The corresponding temperatures of the filament were monitored using a Latronics photoelectric pyrometer.

During the initial baking period after the electrophoresis the filament current and temperature values were as follows:

Time after starting	Filament current amp	Filament temperature, degrees C.
1 min.	6.85(a)	1100°
2 min.	6.90(a)	1200°
3 min.	7.00(a)	1300°
4 min.	7.10(a)	1400°
5 min.	7.20(a)	1500°
24 hrs.	6.80(b)	1600°
24 hrs.	6.65(c)	1450°
48 hrs.	6.65	1450°

<u>Note</u>

(a) Voltage manually increased.

(b) Current dropped at a constant voltage.

(c) Voltage was manually reduced to lower the filament temperature.

The desired case current of 2 m amp corresponded approximately to the filament current of 6.7 amp.

One filament was then mounted in the ion source of the analyzer tube in the mass spectrometer, and the remaining filament units were stored as spares.

REFERENCES

1. R. F. Domagala and D. J. McPherson, Trans. A.I.M.E. 200, 238-246 (1954).
2. J. H. deBoer and J. D. Fast, Rec. trav. chim., 55. 459-467 (1936).
3. J. D. Fast, Metallwirtschaft, 17, 641-644 (1938).
4. J. H. deBoer and J. D. Fast, Rec. trav. chim. 59, 161-167 (1940).
5. W. G. Guldner and L. A. Wooten, J. Electrochem. Soc. 93, 223-235 (1948).
6. R. M. Treco, Trans. ASM 45, 872-890 (1953).
7. R. M. Treco, Trans. AIME 197, 344-348 (1953).
8. D. Cubicciotti, J. Am. Chem. Soc. 73, 2032-2035 (1951).
9. Strukturbericht, 1, 196 (1913-1928), 777-778; 2, 265, 267-269 (1928-1932); 3, 301 (1933-1935); 4, 119 (1936); 7, 87-88 (1939).
10. W. M. Cohn, J. Electrochem. Soc. 68, 65-71 (1935).
11. R. F. Geller and P. J. Yavorsky, J. Research Natl. Bur. Standards, 35, 87-110 (1945).
12. J. W. Hickman and E. A. Gulbransen, Anal. Chem. 20, 158-165 (1948) (Examination of oxide layers by electron diffraction.)
13. P. Duwez and F. Odell, J. Am. Ceram. Soc. 33, 274-283 (1950).
14. A. Dietzel and H. Tober, Ber. deut. keram. Ges. 30, 47-61, 71-82 (1953).
15. P. Murray and E. B. Allison, Trans. Brit. Ceram. Soc. 53, 335-361(1954) (Study of the monoclinic ⇄ tetragonal phase transformation in ZrO_2). Chem. Abstr. 48, 11891 (1954).
16. St. v. Naray-Szabo, Z. Krist., A94, 414-416 (1936).
17. O. Ruff and F. Ebert, Z. anorg. Chem. 180, 19-41 (1929).
18. W. M. Cohn and S. Tolsdorf, Z. Physik. Chem. B8, 331-356 (1929).

19. F. Henning, Naturwissenschaften, 13, 661 (1925).

20. P. Clausing, Z. anorg. Chem., 204, 33-39 (1932).

21. N. Zirnowa, Z. anorg. Chem. 218, 193(1934).

22. W. A. Lambertson and F. H. Gunzel, U. S. Atomic Energy Comm., Publ. AECD-3465 (1952).

23. E. Wedekind, Z. anorg. Chem., 45, 391 (1905).

24. L. Weiss and E. Neumann, Z. anorg. Chem. 65, 248-278 (1910).

25. A. E. van Arkel and J. H. de Boer, Z. anorg. Chem. 148, 346 (1925).

26. J. Jacob, Schweiz. mineralog. petrog. Mitt., 17, 154-163 (1937).

27. E. Zintl, W. Morawietz, and E. Gastinger, Z. anorg. Chem., 245, 8-11 (1940).

28. H. Jakobs, J. Appl. Phys. 17, 596-603 (1946).

29. M. Hoch, W. O. Grooves, and H. L. Johnston, Am. Chem. Soc., Abstr. of Papers 126, 42R-43R (1954).

30. M. Hoch and H. L. Johnston, Acta Cryst., 7, 660 (1954) (abstract of Papers 126, 42R-43R (1954).

31. N. Schonberg, Acta Chem. Scand., 8, 627 (1954) footnote.

32. D. J. McAdam and G. G. Geil, J. Research Natl. Bur. Standards 28, 593-635(1942)

33. E. A. Gulbransen and K. F. Andrew, J. Electrochem. Soc., 96, 364-376 (1949).

34. E. A. Gulbransen and K. F. Andrew, Trans. AIME 185, 515-525 (1949).

35. D. Cubicciotti, J. Am. Chem. Soc. 72, 4138-4141 (1950).

36. C. F. P. Bevington, S. L. Martin, and D. H. Mathews, Proc. Intern. Congr. Pure and Appl. Chem. 11th Cong., London 11, 3-16 (1947).

37. J. Belle and M. W. Mallett, J. Electrochem. Soc. 101, 339 (1954).

38. E. A. Gulbransen and K. F. Andrew, Trans. AIME 209, 394-400, (1957).

39. E. Gebhardt, H. D. Seghezzi, and W. Duerrschnabel, J. Nucl. Mater 4, 255 (1961)

40. P. E. Evans and G. Wildsmith, Nature 189, 569-570 (1961).

41. B. Holmberg and A. Magneli, Acta Chem. Scand., 12, 1341 (1958);
B. Holmberg and T. Dagerhamn, ibid. 15, 919-925 (1961).

42. G. V. Samsonov, Ukr. Khim. Zh., 23, 287-296 (1957).

43. B. C. Weber, H. J. Garrett, F. A. Mauer, and M. A. Schwartz, J. Am. Ceram. Soc. 39, 197-207 (1956).

44. B. C. Weber and M. A. Schwartz, Ber. Deut. Keram. Ges. 34, 391-396 (1957).

45. I. I. Korobkov, D. V. Ignatov, A. I. Evstyukhin, and V. S. Emelyanov, Proc. U. N. Intern. Conf. Peaceful Uses At. Energy 2d, Geneva, 5, 60-68 (1958)

46. I. I. Korobkov and D. V. Ignatov, Dokl. Akad. Nauk SSSR, 120, 527-530 (1958); Proc. Acad. Sci. USSR Chem. Sect., 120, 369-373 (1958).

47. E. S. Sarkisov, N. T. Chebotarev, A. A. Nevzorova, and A. I. Zverkov, At. Energ. (USSR) 5, 550-553 (1958); Soviet J. At. Energy 5, 1027-1031 (1958).

48. L. N. Komissarova, Yu. P. Simanov, and Z. A. Vladimirova, Zh. Neorgan. Khim., 5, 1413-1417 (1960); Russ. J. Inorg. Chem. 5, 687-689 (1960).

49. C. E. Curtis, L. M. Doney, and J. R. Johnson, J. Am. Ceram. Soc., 37, 458-465 (1954).

50. J. Adam and M. D. Rogers, Acta Cryst. 12, 951 (1959).

51. J. D. McCullough and K. N. Trueblood, Acta Cryst. 12, 507 (1959).

52. W. B. Pearson, "A Handbook of Lattice Spacing and Structures of Metals and Alloys", Pergamon Press (1964), 246.

53. K. Yardley, Min. Mag. 21, 169 (1926).

54. O. Ruff and F. Ebert, Z. f. Anorg. Allg. Chem. 180, 19 (1929).

55. R. P. Elliot, "Constitution of Binary Alloys", McGraw-Hill (1965) 709.

56. D. K. Smith and H. W. Newkirk, Acta Cryst. 18, 983 (1956).

57. D. K. Smith and C. F. Cline, J. Amer. Ceram. Soc. 45, 249 (1962).

58. C. E. Melton, Rev. Sci. Instr. 29, 250 (1958).

59. D. L. Goldwater and E. Danforth, Phys. Rev. 103, 871 (1956).

60. O. A. Weinreich, Phys. Rev. 82, 573 (1951).

61. O. A. Weinreich and H. Bleecher, Rev. Sci. Instr. 23, 56 (1952).

62. E. T. Hanley, J. Appl. Phys. 19, 583 (1948).

63. M. J. Buerger, Amer. Min. 33, 101 (1948).

64. A. Ubbelohde, Quart. Rev. Chem. Soc. 11, 246 (1956).

65. A. Ubbelohde and I. Woodward, Proc. Royal Soc. (London) 188, 353 (1947).

66. P. Murray and E. Allison, Trans. Brit. Ceram. Soc., 53, 335 (1954).

67. J. Bailey, Proc. Roy. Soc. (London), Series A, 270, 395 (1964).

68. G. Wolton, J. Amer. Ceram. Soc., 46, (9), 419 (1963).

69. G. Wolton, Acta Cryst. 17, (6), 763 (1964).

70. C. F. Grain and R. C. Garvie, "Mechanism of the Monoclinic to Tetragonal Transformation of Zirconium Dioxide", U. S. Bureau of Mines Report 6619 (1965).

71. B. Ya. Sukharevskii, B. G. Alapin and A. M. Gavrish, Ukr. Sci. Res. Inst. Refract., Kharkov, Uk.S.S.R. Izv. Akad. Nauk S.S.S.R., Neorgan. Mater. 1 (9), 1537 (1965).

72. E. Kauer, O. Klinger, A. Rabenau, Z. Electrochem., 63, 927 (1959).

73. R. C. Garvie, J. Phys. Chem. 69, 1238 (1965).

74. K. S. Mazdiyasni C. T. Lynch and J. S. Smith, J. Amer. Ceram. Soc., 48, 372 (1965).

75. J. P. Pemsler, Electrochem. Technology 4 (3-4), 128 (1966).

76. J. B. Livingstone, Private communication quoted by Pemsler(75).

77. J. Livage and C. Mazières, Compt. Rend. Acad. Sc. Paris, 261, Group 8, 4433 (1965).

78. F. Vahldiek, L. B. Robinson and C. T. Lynch, Science, 142 (3595), 1059 (1963

79. J. Debuigne and P. Lehr, Proc. Conference on Corrosion of Reactor Materials, International Atomic Energy Agency at Europahaus, Salzburg, Austria, 4-8 June 1962. (in French).

80. P. J. Yavorsky, Ceramic Age (June 1962).

81. D. L. Douglass, Corrosion Science, 5, 255 (1965).

82. G. Saur, H. J. Laue and H. Borchers, Metall, 18 (7), 704 (1964). (in German).

83. J. C. Greenbank and S. Harper, Electrochem. Technology, 4 (3-4), 88 (1966).

84. C. F. Smith and W. B. Crandall, J. Amer. Ceram. Soc. 47, 12 (1964).

85. J. N. Wanklyn, "Corrosion of Zirconium Alloys", ASTM Special Technical Publication 368, p. 58 (1964).

86. D. L. Douglass, Proc. Conference on Corrosion of Reactor Materials, International Atomic Energy Agency at Europahaus, Salzburg, Austria, 4-8 June 1962.

87. B. Cox and C. Roy, Electrochem. Technology, 4, (3-4), 121 (1966).

88. J. N. Wanklyn, Electrochem. Technology, 4, (3-4), 81 (1966).

89. R. Haul and D. Just, Z. Elektrochem., 62 (10) 1124 (1958).

90. R. Haul and Just, J. Appl. Phys., Suppl. to Vol. 33, (1), 487 (1962).

91. R. Haul and G. Duembgen, Z. Elektrochem., 66 (819), 636 (1962).

92. W. C. Hagel and J. D. Mackenzie, Phys. and Chem. of Glasses, 5 (4), 113 (1964).

93. W. C. Hagel, J. Am. Ceram. Soc., 48, (2), 70 (1965).

94. W. D. Kingery and M. Berg, J. Appl. Phys. 26, 1205 (1955).

95. W. D. Kingery, J. Pappis, M. E. Doty and D. C. Hill, J. Am. Ceram. Soc., 42 (8), 393 (1959).

96. Y. Oishi and W. D. Kingery, J. Chem. Phys., 33 (2), 480 (1960).

97. W. D. Kingery, D. C. Hill and R. P. Nelson, J. Am. Ceram. Soc., 43 (9), 473 (1960).

98. A. Madeyski and W. W. Smeltzer, Materials Res. Bull., 2, 427 (1967).

99. D. L. Douglass and Carl Wagner, J. Electrochem. Soc., 113 (7), 671 (1966).

100. R. W. Ure, J. Chem. Phys., 26, 1363 (1957).

101. R. W. Vest, N. M. Tallan and W. C. Tripp, J. Am. Ceram. Soc., 47, (12), 635 (1964).

102. S. Aronson, J. Electrochem. Soc., 108, 312 (1961).

103. L. A. McClaine, Technical Documentary Report No. ASD-TDR-62-204, Part II, Air Force Materials Laboratory, Aeronautical Systems Division, Wright Patterson Air Force Base, Ohio, p. 54, May 1963.

104. T. E. Hanley, J. Appl. Phys. 19, 583 (1948).

105. O. A. Weinreich, Phys. Rev., 82, 573 (1951).

106. O. A. Weinreich and H. Bleecher, Rev. Scient. Instr., 23, 56 (1952).

107. D. L. Goldwater and W. E. Danforth, Phys. Rev. 103 (4), 871 (1956).

108. C. E. Melton, Rev. Scient. Instr., 29, 250 (1958).

109, P. C. Carman and A. W. Haul, Proc. Royal Soc. (London), Series A, 222, 109 (1954).

110. J. Crank, "Mathematics of Diffusion", p. 326, Clarendon Press, Oxford (1956).

111. G. R. Wallwork. W. W. Smeltzer and C. J. Rosa, Acta.Met., 12, 409 (1964).

112. P. G. Shewmon, Diffusion in Solids, McGraw Hill, (1963), p. 149.

113. W. W. Smeltzer, R. R. Haering and J. S. Kirkaldy, Acta. Met., 9, (9), 880 (1961).

114. J. Chute, A.E.C.L. - 1999, (Aug. 1964).

115. C. Wagner, Diffusion in Solids, Liquids, Gases, edited by W. Jost, p. 71, Academic Press, New York (1952).

116. R. J. Hussey and W. W. Smeltzer, J. Electrochem. Soc. <u>111</u>, (5), 564 (1964).

117. E. W. Hart, Acta. Met. <u>5</u>, 597 (1957).